Technische Universität München
Fakultät für Chemie

Creating molecular memory through a carbodiimide-driven reaction cycle

Fabian Simon Schnitter

Vollständiger Abdruck der von der Fakultät für Chemie der Technischen Universität München zur Erlangung des akademischen Grades eines

Doktors der Naturwissenschaften (Dr. rer. Nat.)

genehmigten Dissertation.

Vorsitz:		Prof. Dr. Cathleen Zeymer
Prüfer der Dissertation:	1.	Prof. Dr. Job Boekhoven
	2.	Priv.-Doz. Dr. Alexander Pöthig
	3.	Prof. Dr. Thomas Hermans

Die Dissertation wurde am 02.05.2022 bei der Technischen Universität München eingereicht und durch die Fakultät für Chemie am 08.07.2022 angenommen.

Abstract

Remembering and processing past events has been observed as a recurring motif in many cellular processes. Such cellular memory is regulated by the interplay of biological reaction networks and reaction cycles. These so-called transcriptional states are dynamic, and its components are continuously turned over. Given the degradation of the molecules which make memory, the question emerges how the memory can surpass the lifetime of its source? To understand biological mechanisms like these, the field of systems chemistry tries to recreate biologic processes with synthetic approaches. A system chemist's reaction cycle is composed of simpler molecular building blocks than the biopolymers observed in nature. Yet, it exerts similar behaviour. Functional structures emerge in a reaction cycle when so called fuel molecules are consumed and thereby temporarily alter the physical properties of the assembly's building block. As a result, the material properties are dynamic and are controlled by the various reactions taking place. Understanding these dynamics requires the examination of the reaction cycle's kinetics.

Recently, the so called carbodiimide-driven reaction cycle has been introduced. The repeatedly activation and deactivation of building blocks by carbodiimides was coupled to the self-assembly of supramolecular structures. By synthesizing different derivatives of the activated building block, which is a water labile anhydride, the deactivation could be tuned towards fast hydrolysis rates. Now, it was necessary to quench all the reactions taking place in the reaction cycle to get high quality analytic data. Otherwise, most anhydride would degrade within the time course of analysis. In addition to this quenching method a standard routine is proposed in this work how to characterize the dynamic material properties. Amongst the different morphologies which have been created, the work shows that active building blocks forming crystals could create memory by occupying bistable states. As required for a bistable system, the crystals exert proper feedback, and the unstable anhydride already provides a necessary degradation pathway. Memory like cellular memory could be created in form of two stable states, an on-state with the presence of crystals and an off-state without. The bistable states could be switched between each other by applying different triggers. Moreover, patterns could be drawn similar to pixel displays and information has been processed by creating a Boolean Or-port.

Zusammenfassung

Das Speichern und Verarbeiten vergangener Ereignisse wurde als wiederkehrendes Motiv in vielen zellulären Prozessen beobachtet. Ein solches zelluläres Gedächtnis wird durch das Zusammenspiel von biologischen Reaktionsnetzwerken und Reaktionszyklen gesteuert. Diese so genannten Transkriptionszustände sind dynamisch, und ihre Komponenten werden ständig verstoffwechselt. Angesichts des Abbaus der Moleküle, die das Gedächtnis bilden, stellt sich die Frage, wie das Gedächtnis die Lebensdauer seiner Quelle überdauern kann. Um biologische Mechanismen wie diese zu verstehen, versucht die Systemchemie, biologische Prozesse mit synthetischen Ansätzen nachzubilden. Der Reaktionszyklus eines Systemchemikers besteht aus einfacheren molekularen Bausteinen als die in der Natur beobachteten Biopolymere. Dennoch weist er ein ähnliches Verhalten auf. Funktionelle Strukturen entstehen in einem Reaktionszyklus, wenn so genannte Treibstoffmoleküle verbraucht werden und dadurch die physikalischen Eigenschaften des Bausteins der Struktur vorübergehend verändern. Infolgedessen sind die Materialeigenschaften dynamisch und werden durch die verschiedenen ablaufenden Reaktionen gesteuert. Um diese Dynamik zu verstehen, muss die Kinetik des Reaktionszyklus untersucht werden.

Vor kurzem wurde über den so genannten Carbodiimid-getriebenen Reaktionszyklus berichtet. Mit Hilfe dieses Zyklus wurde die wiederholte Aktivierung und Deaktivierung von Bausteinen an den Selbstaufbau verschiedener Strukturen gekoppelt. Durch die Synthese verschiedener Derivate des aktivierten Bausteins, eines wasserlabilen Anhydrids, konnte die Deaktivierung hin zu schnellen Hydrolyseraten entwickelt werden. Um qualitativ hochwertige Daten zu erhalten, mussten nun alle im Reaktionszyklus stattfindenden Reaktionen gequencht werden. Andernfalls würde sich das meiste Anhydrid im Laufe der Analyse zersetzen. Zusätzlich zu dieser Quench-Methode wird in dieser Arbeit eine Standardroutine vorgeschlagen, um die dynamischen Materialeigenschaften zu charakterisieren. Die Arbeit zeigt, dass diejenigen Bausteine ein Gedächtnis ausbilden können, die Kristalle formen. Das Gedächtnis wird ausgebildet, indem bistabile Zustände eingenommen werden. Wie für ein bistabiles System erforderlich, üben die Kristalle eine angemessene Rückkopplung aus. Zudem bietet das instabile Anhydrid einen nötigen Abbauweg. Es wird gezeigt, dass ein Gedächtnis analog zu einem zellulären Gedächtnis in Form von zwei stabilen Zuständen ausgebildet werden kann. Dies sind ein Ein-Zustand in Anwesenheit von Kristallen und ein Aus-Zustand ohne Kristalle. Mittels verschiedener Auslöser, kann zwischen den beiden Zuständen geschalten werden. Außerdem können Muster ähnlich wie bei einem Pixel-Display gezeichnet werden, und es können Informationen ähnlich eines booleschen Oder-Ports verarbeitet werden.

Contents

1 General introduction - Cellular memory

Cellular memory has been described as the conversion of a transient signal into a sustained response.[1] Usually, its biological asset is a more efficient response when the same signal is faced again later. As such the immune system builds up a secondary immune response,[2,3] skin cells produce the tanning pigment melanin when exposed to ultraviolet radiation[4,5] or muscle fibers grow upon mechanical stress.[6] These capabilities stay encoded within the cell even if its original response has faded. It has been shown that the memory of a strength training sustains even after a prolonged time of inactivity and muscle loss, which facilitates retraining.[7] When looking at how long such memory is stored compared to the permanent turnover of cellular material or the lifespan of individual cells, the question about its molecular mechanisms arises.[8] Whereas genetic information is stored and adapted through generations in the total genome, most cellular memory is effected by feedback loops[9] and epigenetic processes.[10,11] The interplay of both result in distinct transcriptional states which are the core of cellular memory. Under certain condition, such memory can be inherited through deoxyribonucleic acid (DNA) replication and cell division. Even though a lasting memory of a biologic response is created, the storage of cell memory is a dynamic process. Memory can be deleted or fades over time although the exact same set of DNA-based genetic instructions have been passed to daughter cells.[12]

Synthetic biologists started to explore the mechanisms behind cellular memory and adapted those to perform distinct tasks. A powerful tool for biotechnological applications was found in the transcriptional states of the lactose operon. Originally, it is required for bacteria to transport and metabolize lactose. Its state can be switched between on and off, regulated by both positive and negative feedback loops.[13] By cloning the lactose operon into an expression vector, protein expression can be turned on in an inducible manner. The phage lambda system is another example of individual cells possessing the capacity to remember. A mutual repression loop navigates the virus through two infectious states.[14] When infecting bacteria, its genetic information gets incorporated into the host's genome. Residing in that lysogenic state, the viral material is replicated together with the host genome as long as the host stays healthy. The host's response to stress produces signals which shifts the lysogenic stage to the following stage of viral infection, which is lytic growth. Apart from these examples, transcriptional states play a pivotal role in cell processes like cell differentiation[15] and cell division.[16–19] The primary gene transcription regulation taking place in such processes are epigenetic ones.[20] By activating and silencing certain DNA regions, the total gene pool can be used for different tasks. The transcriptional state is regulated by methylation-demethylation, acetylation-deacetylation, and other modifications of histones as well as specific nucleotide regions within the DNA sequence.[21,22] It is thought that such epigenetic patterns are inherited to daughter cells by feedback loops, involving methyltransferases. Concentrations of such DNA methyltransferases were also increased in experiments, studying the processes taking place in neurons whilst learning.[23] When introducing chemicals that block the action of DNA methyltransferases, the formation of memory could be stopped. The role of epigenetics in memory formation and storage is also linked to the loss of memory with age which is accompanied with a loss of epigenetic control.

Cellular memory is performing a wide variety of tasks as pointed out above. Therefore, its emergence can be considered as pivotal for the existence of animate matter as we currently observe it. As evolution proceeded from prokaryotes to eukaryotes, also the mechanisms for creating, storing, and retrieving memory developed. In terms of epigenetics, regulation in prokaryotes is strikingly

different from that in eukaryotes, mainly higher eukaryotes.[11] However, both make use of highly evolved cellular machinery like enzymes, DNA and ribonucleic acid (RNA). The question remains what mechanisms of cellular like memory could have existed in a prebiotic world without complex biopolymers. In other words, how can information be stored and inherited in simple molecules although the lifetime of those molecules is limited due to constant turnover rates? This question should be answered in the context of this thesis.

2 Aim of the thesis

The aim of this thesis is to explore mechanisms to store memory in minimal, synthetic reaction networks.[24] I aim to do so by using reaction networks that convert chemical energy and engineer within these networks feedback loops that allow for bistable behavior. In chapter 3, I will discuss a selection of chemical reactions that have been developed and can be used for the creation of bistable behavior. From that chapter it also becomes clear that it remains challenging to obtain a quantitive analysis of the reactions involved in the reaction cycle. In chapter 4 I will discuss standard quantitative methods and explain why such standard methods could be obstructive when exploring dynamic reaction cycles. Therefore, in chapter 5, I developed quenching methods to stop all the reactions taking place within the reaction cycle. The chapter showcases a way how to effectively determine the kinetic parameters of carbodiimide-driven reaction cycles. In chapter 6, I highlight how such a reaction cycle can be used to regulate the behavior of supramolecular materials. In an intermission, I guide the reader through the progress that has been made by the field in the development of non-linear behavior in chemical reaction cycles. Chapter 7 will explain the kinetic mechanisms behind bistable states. I will briefly detail how bistable states become stable and thereby display hysteresis. The chapter ends with a summary of oscillating systems observed in biology. The subsequent chapter 8 reviews artificial bistable systems which have been engineered without using evolved biomolecules. After describing the current limitations of such systems in chapter 9, I will finally discuss my efforts towards the creation of bistability in chemical reaction cycles. We found an exciting mechanism that has to do with the non-linearity of crystallization and feedback of crystals on their reaction cycle by which I can create bistability. I explore the bistable behavior to create volatile memory, i.e., memory of a past event that lasts longer than the lifetime of the molecules that play a role in the memory. Finally, I close the thesis with a summary and outlook.

3 Fuel-driven reaction cycles

Many biological processes are regulated by reaction cycles in which a molecule is activated and deactivated for a function at the expense of a small molecule.[24] A prominent example is the dynamic self-assembly of proteins to form the cytoskeletal network.[25–28] In such cycles, inactivated precursor building blocks are temporarily activated by fuel molecules. The fuel either binds to the precursor non-covalently or reacts with it forming covalent bonds. These modifications can change the physical interactions between building blocks leading to their assembly. After activation, a second reaction pathway exists. This reaction deactivates the activated product which yields the original precursor and its escape from the assembly. Thus, the molecular assemblies reside outside the thermodynamic equilibrium and its material properties are controlled by the kinetics of the reaction cycle. Although this process is wasteful in terms of energy, its benefits lie in high degrees of adaptivity and spatio-temporal control.[29] In the case of the cytoskeleton for example,

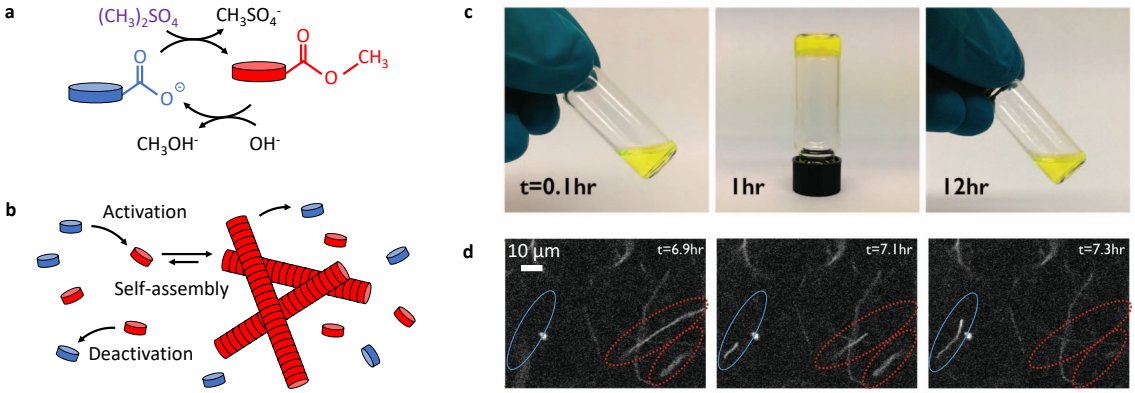

Figure 1: Methylation and ester hydrolysis reaction drive the formation of transient assemblies. a Carboxylates of precursor molecules get methylated by methylsulfate. The ester hydrolysis reaction is driven at alkaline pH. **b** Schematic overview of the activation, deactivation and molecular self-assembly taking place simultaneously. **c** Time-lapse photograph of transient hydrogel formation.[33] **d** Fluorescence microscope micrograph of dynamic fiber formation.[33] Reprinted by permission from the American Association for the Advancement of Science, Copyright © 2015.

nucleoside triphosphate[30,31] (fuel) binds non-covalently to monomeric proteins (precursor) and thereby induces a conformational change. Polymeric fibers start to grow such as actin filaments or microtubules.[32] Meanwhile, the fuel molecule hydrolyses to nucleoside diphosphate (waste) which causes disassembly of the biopolymers.

3.1 A synthetic reaction cycle driven by the hydrolysis of methylating agents

The goal of systems chemistry is to recreate the emergent behaviors observed in biologic systems.[34–39] These behaviors are often regulated outside of equilibrium by chemical reaction cycles and thus effort has been made to develop synthetic analogs.[40–42] Van Esch and co-workers pioneered the field by introducing a methylation reaction to activate small molecule building blocks.[33,43] In that work, the precursor molecules carried carboxylic acid groups which were well solubilized at pH values above their pKa (Fig. 1 a, b). Upon addition of methylating agents like methylsulfate, the precursor is activated by converting its carboxylates into their corresponding methylesters. Consequently, their negative charges are abolished. Due to the removed repulsive forces and the unchanged attractive forces of the remainder of the precursor, the molecules self-assemble into fibrillar networks (Fig. 1 c, d). Given the hydrolytic instability of the methylester, the building block can hydrolyze back to the precursor (deactivation). After deactivation, the precursor can cycle through further rounds of activation and deactivation until all fuel is depleted. Thus, the lifetime of the self-assembled material can be tuned by the amount of fuel added. The fibrillar network disappears after all fuel has been consumed (Fig. 1 c).

3.2 A reaction cycle driven by the hydrolysis of condensing agents

The charge abolishment strategy to induce molecular self-assembly has also been used by converting carboxylate groups into anhydrides (Fig. 2 a).[44,45] As a fuel, several carbodiimide condensing agents have been reported to drive the reaction cycle like N,N'-dicyclehexylcarbodiimide (DCC), N,N'-diisopropylcarbodiimide (DIC) or 1-ethyl-3-(3-dimethylaminopropyl)carbodiimide (EDC).[45] The latter is preferentially applied due to its high activation yields and its high water solubility. The activation reaction is most efficient at acidic pH as the carbodiimide is activated by protona-

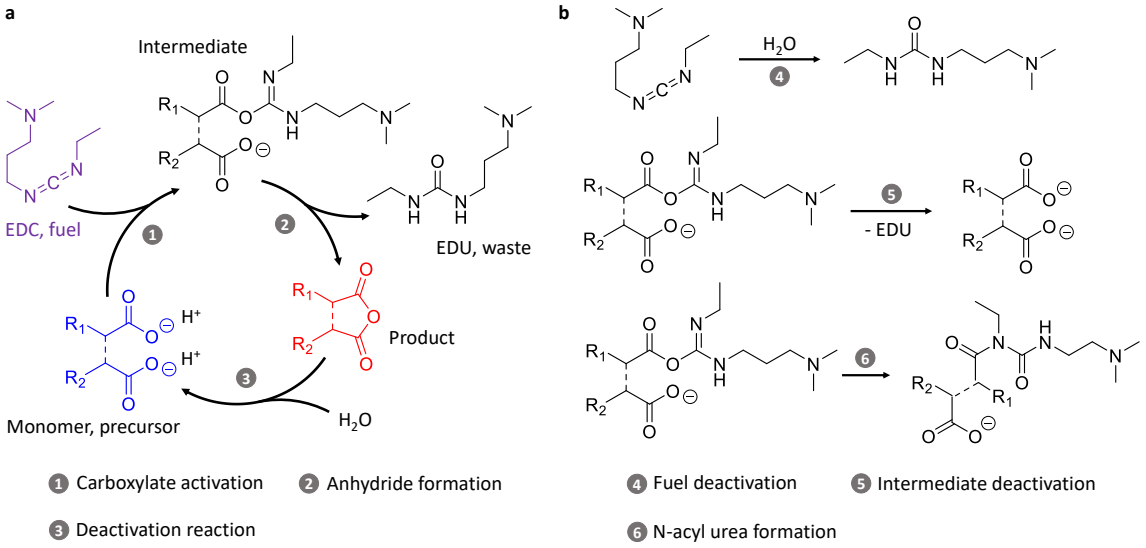

Figure 2: The carbodiimide-driven reaction cycle. **a** Main reactions taking place in the reaction cycle. **b** Occurring side reactions which have been observed.

tion of one nitrogen atom. The strong electrophile is attacked by the anionic carboxylate resulting in a high energy O-acylisourea intermediate. In a subsequent step, a second carboxylate attacks to form an anhydride. An intramolecular attack results in a ring closure or an intermolecular reaction occurs when a second precursor molecule attacks. In that second step, urea is released. The formed anhydride is hydrolytically instable and reacts with water, the solvent, reverting the product molecule into the precursor. Thus, effectively, the precursor catalyzes the conversion of the fuel molecule (carbodiimide) to a low energy waste molecule (urea). While catalyzing the hydration, the precursor is transiently activated into a higher energy anhydride state. As the reaction cycle also transiently consumes protons, the reaction cycle is performed in buffered media and thus constant reaction rates are preserved throughout the cycle. 2-Morpholino-ethanesulfonic acid (MES) is mostly used as its functional groups do not interfere with the reaction cycle's reactions. The deactivation rates can be adjusted by functional groups in the proximity of the anhydride. Structural effects on hydrolysis rates can be explained in terms of steric and electronic effects of substituents. Electron-attracting substituents assist, and electron-repelling substituents hinder the degradation rates of e.g., benzoic anhydride derivatives.[46–48] Besides the described reactions, several side reactions have been observed (Fig. 2 b). For example, the fuel molecule hydrates to the urea waste product by reaction with the water. This reaction is neglectable as the rate is very low. Besides the formation of the anhydride, two more pathways exist for the intermediate O-acylisourea. Apart from the anhydride formation, the intermediate can hydrolyze, commonly at low rates, without forming the product molecule. Furthermore, it can rearrange into an N-acylurea side product. This reaction is usually observed with bulky precursor molecules as steric hindrance slows down the intramolecular ring closure. This stable sideproduct prohibits the precursor from further activation, and thus its formation should be suppressed. Apart from redesigning the precursor molecule, pyridine can be added which forms more stable intermediates.[44]

Various kinds of assemblies have been coupled to the carbodiimide-driven reaction cycle (Fig. 3). The scope is high given the simplicity of the cycle. Readily available precursor molecules like N-protected aspartic (D) or glutamic (E) acids self-assemble into supramolecular structures upon activation with carbodiimides. The self-assembly behavior can be further designed by the usage of short peptide sequences like N-Fmoc-AAD-OH (single letter code for amino acids; A stands for

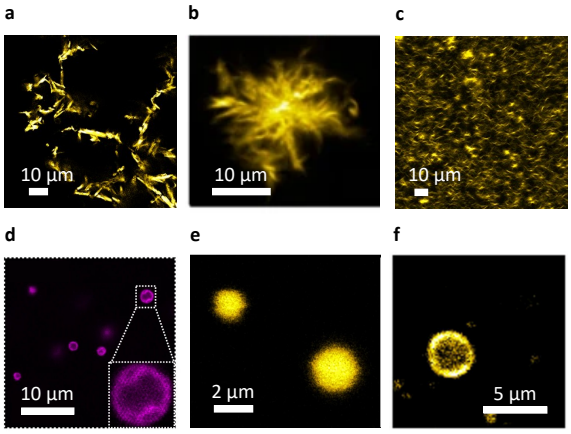

Table 1 | Different precursors and the emergent type of assembly

	Type of assembly	Precursor
a	Crystals	N-Boc-Asp-OH
b	Colloids	Fmoc-D-OH, Fmoc-E-OH, Fmoc-GD-OH
c	Fibers	Fmoc-AAD-OH, Fmoc-AVD-OH, Fmoc-AAE-OH, Fmoc-AVE-OH, Ac-FIID-OH
d	Coacervates	Ac-FRGRGRGD-OH
e	Oil droplets	2-octen-1-ylsuccinic acid, 2-decen-1-ylsuccinic acid, valeric acid, caproic acid
f	Vesicles	Fmoc-GGD-OH, Fmoc-GGE-OH

Figure 3: The carbodiimide reaction cycle can be used to drive a large array of morphologies. Amongst them are (**a**), crystals[55] (**b**), colloids[45,56] (**c**), hydrogel fibers[45,57] (**d**), coacervates[50] (**e**), oil droplets[52,58] and (**f**), vesicles.[59]

alanine), which forms dynamic hydrogel fibers.[45] Self-assembly into fibrillar structures is driven by hydrophobic interactions between the fluorenylmethoxycarbonyl (Fmoc) protecting groups in combination with the alanine residues. The latter have a high propensity to form beta-sheet structures, directed by the peptide backbone and sidechain.[49] Abolishing negative charges can also increase electrostatic interactions to negatively charged molecules such as DNA or polystyrene sulfonate. Thereby, complex coacervate-based droplets can be formed.[50] These assemblies are a great model for the study of membraneless organelles,[51] which are also complex coacervate-based droplets regulated through chemical reactions. Furthermore, the reaction cycle has been used for the development of chemically fueled emulsions based on oils. These transient emulsions have the exciting property that they decay through zero-order kinetics. As such, the carbodiimide driven reaction cycle showed the zero-order release of hydrophobic drugs in the time course of several hours.[52,53] In addition, by tuning deactivation rates transient, self-erasing inks have been created.[54] These labels could be used to e.g., display the expiration date of food.

4 Outlook - Kinetic analysis

To understand and program the kinetics of the self-assembling system, typically concentrations of intermediates in the reaction cycle are measured over time. By recording the EDC consumption and anhydride evolution, the rate constants for activation and deactivation can be determined empirically which are used for kinetic modelling (Fig. 4 a, b). Various spectroscopy-related techniques can be applied to determine concentrations such as UV-Vis spectroscopy or nuclear magnetic resonance spectroscopy (NMR).[60,61] UV-Vis spectrophotometry can be used when the precursor-product conversion produces a change in absorbance at a specific wavelength over time. With a fast data collection speed, this technique visualizes the reaction progress almost in real time. Combined techniques like high performance liquid chromatography (HPLC) are preferentially used for analyzing multi component reaction cycles as each component can be separated before analysis. Additionally, the obtained chromatogram provides valuable information such as the formation of intermediate species. Those can be identified qualitatively after separation. However, the data collection frequency is limited by the time it takes to elute the components from the stationary phase of the HPLC column. To retain the building blocks applied in the carbodiimide-driven reaction cycle, non-polar stationary phase is used which interacts with the hydrophobic

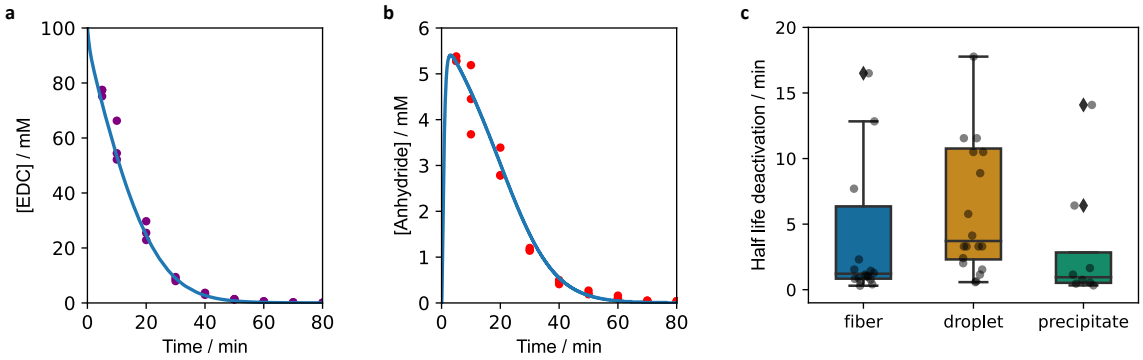

Figure 4: Typical kinetic behavior of a carbodiimide-fueled reaction cycle. The transient evolution of (**a**), EDC fuel and (**b**), anhydride product as measured by HPLC. The markers represent experimental data and the lines are predicted values by a kinetic model.[62] **c** A summary of deactivation rates derived from both published and un-published activated precursor building blocks. The products' half-lives are plotted by groups of fibers, droplets, and precipitates.

moieties within the building block. In such reversed phase condition, the mobile phase partially contains water and thus the reaction cycle's reactions continue during the separation process. For complex reaction mixtures, the runtime of an HPLC experiment is around ten minutes.[45,56,58] The additional hydrolysis taking place in the time between injection and detection has no dramatic effect on the data quality of reaction cycles with low deactivation rates. But it becomes a problem when measuring fast deactivation rates, i.e., molecules with half-lives in the range of minutes (Fig. 4 c). With such compounds, most anhydride degrades during the separation process on the stationary phase in an HPLC experiment. An alternative method of measuring concentrations is by NMR experiments. However, with NMR, the time resolution is mostly determined by the number of scans required to obtain a good signal to noise ratio. At low concentrations, the data collection rate would be in the range of minutes as well. Furthermore, one is limited to the experimental infrastructure of the NMR experimental setup. The NMR tube cannot be exchanged easily by other reaction containers which might allow the possibility to stir the sample. Furthermore, changing the reaction conditions like temperature is inconvenient. Taken together, there is a need for a method to separate the reaction cycle experiment from the kinetic analysis of its component's concentrations. Such an approach is typically done by quenching all the reactions taking place before analyzing, which we will be exploring in the next chapter.

5 A Method to Quench Carbodiimide-Fueled Self-Assembly

Abstract.

In this work, a method is proposed to precisely determine the rate constants of carbodiimide driven reaction cycles. To recreate the dynamics observed in life-like systems, faster cycles have been designed. Dealing with half-lives in the order of few minutes or even seconds, it is beneficial to quench all the reactions before analyzing with classical methods. Therefore, aliquots of the reaction mixture were treated with excess of aqueous benzylamine solutions. The benzylamine rapidly reacts with the anhydride, forming stable amide bonds. Furthermore, mixing the benzylamine solution with the reaction cycle's components, pushes the pH to alkaline conditions. It is shown that the activation reaction is completely suppressed at pH values above pH 9. Thus, benzylamine stops both the deactivation and activation reaction. When analyzing the quenched reaction mixture, the formed amide was taken as a measure for the anhydride concentration at the timepoint of quenching. Analyzing the formed amide bears additional advantages. Only one calibration curve is needed to measure distinct anhydride reaction cycles, given the characteristic absorbance of the benzylic ring structure at 254 nm. Furthermore, it improves the detection of compounds with no significant absorption in the examined spectral range. Whereas the amide concentration did not change for days, the EDC fuel concentration decayed within 20 hours. It is shown that EDC reacts with benzylamine forming a guanidine moiety. Therefore, the EDC concentration at the timepoint of quenching is the sum of unreacted EDC and formed guanidine. In this work the method is validated by measuring the fast activation and deactivation rate constants of the protected amino acid N-Boc-aspartic acid. Applying the quench improved data quality, a lot. It is shown that around 50% of the anhydride hydrolyzed on the column without using the quench. Apart from N-Boc-aspartic acid, other reaction cycles with various morphologies have been tested. The work demonstrates the rapid dissolution and conversion of crystals, droplets, colloids, and fibers. Besides improving the data quality, the proposed method also facilitates data acquisition. Data can now be obtained more frequently without the limit of the instrumental setup and instrument acquisition times.

This work has been published:

Title:	A Method to Quench Carbodiimide-Fueled Self-Assembly
Authors:	Fabian Schnitter, Job Boekhoven
First published:	24. July 2020
Journal:	ChemSystemsChem 2021, 3, e2000037.
Publisher:	WILEY-VCH
DOI:	10.1002/syst.202000037

Reprinted with permission of John Wiley and Sons.

This section states the individual work of each author in the publication below. F. Schnitter designed and conducted all experiments. J. Boekhoven and F. Schnitter outlined and wrote the manuscript. The work was performed under the supervision and guidance of J. Boekhoven.

ChemSystemsChem
Communications
doi.org/10.1002/syst.202000037

Special Collection

A Method to Quench Carbodiimide-Fueled Self-Assembly

Fabian Schnitter[a] and Job Boekhoven*[a, b]

In chemically fueled self-assembly, the activation and deactivation of molecules for self-assembly is coupled to a reaction cycle. In biological examples, these reactions are typically fast, such that the building blocks remain activated for mere seconds. In contrast, synthetic reaction cycles are slower for self-assembly, *i.e.*, with half-lives on the order of minutes. In search of life-like, dynamic behavior in synthetic systems, several groups explore faster reaction cycles that form transient labile building blocks with half-lives of tens of seconds. These cycles show exciting properties, but brought about a new challenge, *i.e.*, accurately analyzing the fast cycle is impossible with classical techniques. We thus introduce the notion of quenching chemical reaction cycles for self-assembly. As a model, we use the fast carbodiimide-fueled chemical reaction cycle and demonstrate a method that quenches all reactions immediately. We show its accuracy and demonstrate the application for several reaction cycles and a range of dissipative assemblies. Finally, we offer preliminary design rules to quench other chemically fueled reaction cycles.

In molecular self-assembly, molecules are designed to interact with each other via non-covalent interactions.[1] The range of molecular assemblies that consequently form is enormous, ranging from anisotropic fibers,[2] tapes,[3] and tubes,[4] to isotropic assemblies like (block-copolymer)micelles,[5][6] vesicles[7] and colloids.[8] The field has slowly evolved from rather serendipitous findings to well-defined design rules allowing for a range of applications, so-called supramolecular materials.[9] Inspired by biology, the field has recently focused on the assembly of molecules, driven out of equilibrium by energy-consuming chemical reaction cycles.[10] In these chemically-fueled assemblies, the assembly and disassembly of molecules is coupled to a chemical reaction cycle.[11] The reaction cycle comprises at least two reactions: a building block activation and deactivation reaction (Figure 1A). A precursor molecule is converted into a building block for self-assembly at the expense of a high energy reagent (chemical fuel) in the activation. In the deactivation, the building block is reverted to the precursor spontaneously, *e.g.*, by solvolysis or by reaction with an abundant species in solution. The sum of the reaction thus means that a precursor is temporarily converted into a self-assembling building block driven by the conversion of a molecule of fuel.

The consequence of the fuel-driven self-assembly is that the assembly and disassembly rates are now, in part, regulated by the rates in the chemical reaction cycle. For example, the cytoskeletal microtubules and actin filaments are tightly regulated by the hydrolysis of GTP and ATP, respectively.[12] Because of the kinetic control over self-assembly, their corresponding behavior is rich and includes dynamic instabilities,[13] as well as the treadmilling of actin filaments. It is important to note that the reaction rates of deactivation in these biological examples are fast. For example, tubulin-bound GTP has a half-life of less than a second.[14]

Inspired by the dynamic behavior of biological chemically fueled assemblies, researchers have developed synthetic coun-

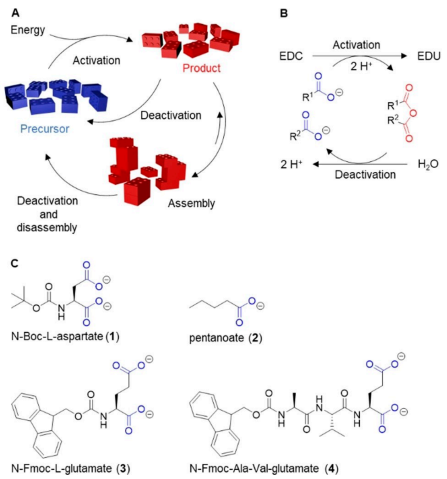

Figure 1. Chemical reaction cycle that fuels self-assembly. A) A generalized reaction scheme for chemically fueled self-assembly. B) The formation of a transient anhydride product from a carboxylate precursor is driven by the hydrolysis of EDC as carbodiimide fuel. C) Precursors used in this work as precursors for the chemical reaction cycle.

[a] F. Schnitter, Prof. Dr. J. Boekhoven
Department of Chemistry
Technical University of Munich
Lichtenbergstrasse 4, 85748 Garching (Germany)
[b] Prof. Dr. J. Boekhoven
Institute for Advanced Study
Technical University of Munich
Lichtenbergstrasse 4, 85748 Garching (Germany)
E-mail: job.boekhoven@tum.de

Supporting information for this article is available on the WWW under https://doi.org/10.1002/syst.202000037

An invited contribution to a Special Collection on Fuelled Self-Assembly

terparts. Exciting behaviors of these assemblies have been described, which include solutions that spontaneously oscillate between different types of assemblies,[15] molecular fibers that undergo dynamic instabilities,[16] and molecular assemblies that can select molecules from a pool of reactants.[17] One of the challenges in the synthetic approach towards dynamic materials is the lack of fast chemical reaction cycles. For example, the early work by van Esch and Eelkema used the carboxylic acid alkylation and its hydrolysis as a chemical reaction cycle.[18] At a pH of 10, the product had a half-life of roughly 0.3 hours.[16] To accelerate the rates of activation and deactivation, our group and the group of Hartley recently introduced the activation of carboxylates into transient anhydrides driven by the hydrolysis of carbodiimide-based condensing agents like 1-ethyl-3-(3-dimethylaminopropyl) carbodiimide (EDC) (Figure 1B).[19] These anhydrides are prone to hydrolysis resulting in a half-life ranging from several minutes to tens of seconds, depending on the nature of the anhydride. We indeed observed that such systems had high dynamics with rapid assembly and disassembly.[20] The carbodiimide fuel has been further explored by us and others to yield symmetric,[19c,21] and asymmetric anhydrides,[19a,20,22] activated esters like N-hydroxysuccinimide esters,[23] and phenol esters.[24] Due to the fast reaction cycle with tunable kinetics, the carbodiimide driven cycle has successfully been used for the self-assembly of peptide-based gels,[19a] catalytic nanofibers,[25] vesicles,[20], coacervates,[26] and others. However, as the hydrolysis rate of the product increased, we encountered a new challenge: the techniques we used for quantification (HPLC and NMR) are not able to accurately measure concentration because of the rapid deactivation of the compound of interest. For example, when a labile anhydride retains on the HPLC column, we observed significant amounts were hydrolyzed. Similarly, the acquisition times of NMR were too long to acquire reliable spectra of the compounds related to the reaction cycle. Other research groups have also introduced new chemical reaction cycles with fast kinetics. For example, Hermans recently introduced a redox-chemistry driven reaction cycle that operates with half-lives of minutes.[27] Likewise, Fletcher uses redox coupled (autocatalytic) reaction cycles that operate on minute timescales. These fast reaction cycles potentially also suffer from the inaccurate and complicated kinetic analysis by HPLC or NMR as they are further accelerated in the future.

In this work, we thus introduce the notion of quenching chemical reaction cycles to perform kinetic analysis. We describe a simple method to accurately analyze several carbodiimide-fueled chemical reaction cycles. We used a reagent that can almost immediately stop all four reactions taking place in the reaction cycle. We demonstrate that quenching chemistry can be applied to several types of anhydrides and works in the presence or absence of assemblies. Due to the effectiveness of the chemistry, the quenched samples can either be stored for up to several weeks or directly be analyzed. Finally, we establish design rules for quenching chemistry for chemical reaction cycles. Our method opens the door to further accelerate chemical reaction cycles and explore rapid dynamic behavior while retaining a quantitively understanding of the reactions involved.

Chemically fueled reaction cycles that can drive self-assembly comprise at least two reactions: a chemical reaction that activates building blocks for self-assembly and one that deactivates them (Figure 1A). In the carbodiimide driven reaction cycle, the precursor in the cycle carries at least one carboxylate (Figure 1B). In the first reaction, the precursor's carboxylate reacts with a carbodiimide based condensing agent to form the corresponding O-acyl urea intermediate (Figure S1). In the second reaction, the O-acyl urea reacts with a second nucleophile, *i.e.*, an intra- or inter-molecular carboxylate yielding, respectively, an intra- or inter-molecular anhydride. Regarding asymmetric precursor molecules like **1** the ring closure is favored compared to dimer formation because of the near proximity of the second carboxylic group. In the aqueous environment, the anhydride product is rapidly hydrolyzed to the corresponding precursor, which constitutes the deactivation reaction. Finally, the O-acyl urea can hydrolyze directly to the precursor without forming the anhydride (Figure S1). In summary, the overall reaction cycle forms a transient anhydride driven by the hydrolysis of a carbodiimide condensing agent into its corresponding urea.

In this study, we use 1-ethyl-3-(3-dimethylaminopropyl)-carbodiimide (EDC) as a condensing agent because of its high solubility in water, but other work has shown that this cycle can also be driven by other carbodiimide derivatives. In the first part of these studies, we use N-Boc-L-aspartate (**1**) as a precursor molecule (Figure 1C). Its rapid deactivation makes it a great test compound for our quenching chemistry. In order to accurately determine the rate constant of deactivation for the reaction cycle in Figure 2A Figure 2A, we synthesized N-Boc-L-aspartic anhydride (see the synthesis section in the Supporting Information). The powder was dissolved in acetonitrile and further diluted in 200 mM aqueous MES buffer at pH 6. After dilution, the decreasing concentration of anhydride was monitored by HPLC. We were surprised to find that the anhydride concentration of 20 mM had decreased from 20 to 7.5 mM after the first 30 seconds in the reaction cycle (Figure 2B). From there on, the concentration decayed with first-order kinetics. We could not fit the unconventional decay properly using first-order hydrolysis kinetics. Thus, we reasoned that the peculiar kinetics was not due to hydrolysis of the anhydride in the reaction mixture, but rather due to hydrolysis in the mobile phase of the HPLC. If additional hydrolysis in the mobile phase occurred, the concentration anhydride measured would be drastically lower than at given times in the reaction mixture. To test this hypothesis, we injected N-Boc-L-aspartic anhydride dissolved in dry acetonitrile into the HPLC. Even though 20 mM of the anhydride was injected, only 11 mM anhydride was detected, pointing to a loss of over 40% of the initially injected anhydride.

Moreover, when we increased the anhydride retention time, by changing the HPLC-method, we observed less anhydride (Figure S2) confirming that the labile anhydride rapidly hydrolyzes during the analysis resulting in inaccurate data. Given that the acquisition times for 1H-NMR are typically in the range of

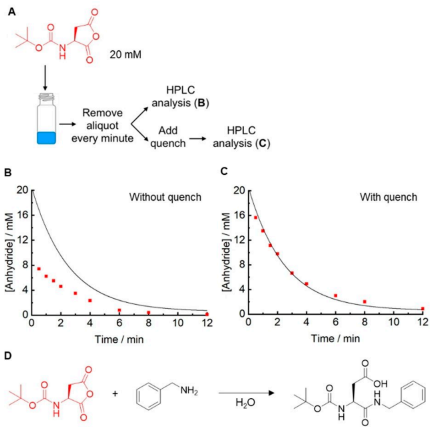

Figure 2. Does the anhydride hydrolyze during the HPLC analysis? A) The hydrolysis reaction of the activated precursor **1**. We injected 20 mM N-Boc-L-aspartic anhydride in water at pH 6. B–C) The concentration anhydride against time as measured by B) directly injecting the reaction mixture, and C) injecting a quenched reaction mixture into HPLC. The black line represents a first-order decay profile as the best fit. D) The quenching solution converts the anhydride of **1** into a stable N-benzyl amide.

several minutes, it is expected that following the hydrolysis of the anhydride by 1H-NMR would not yield much more accurate data. We thus set out to introduce a quenching method that rapidly stops all the reactions in our reaction cycle. We were seeking a method that (i) reacts with the anhydride rapidly to a stable product, (ii) stops the activation reaction, and (iii) reacts with the fuel to stop any side reactions. We used benzylamine as a reagent in our method because: (i) it rapidly reacts with the anhydride forming the stable amide. It will also react with the O-acyl urea forming the same amide. (ii) Due to its basicity, it will immediately increase the pH of the reaction mixture, thus inhibiting the pH-sensitive activation. Moreover, (iii) we found that benzylamine slowly reacts with EDC to the non-reactive guanidine moiety, stopping any further side reaction. Finally, the products (guanidine-derivative and N-benzyl amides) will carry the aromatic benzyl ring, which vastly facilitates HPLC-detection at 254 nm.

We repeated the above-described experiment (20 mM N-Boc-L-aspartic anhydride) and removed aliquots from the reaction mixture at given time points, which we injected in a quenching solution (400 mM benzylamine in water at pH 12). After the quench, we determined the concentration of the stable amide as a measure for the anhydride concentration at the time benzylamine was added (Figure 2C–D). The opening of asymmetric anhydrides formed by precursors like **1** yields two products, which is the benzylamine added either at the side-chain or the backbone of the amino acid. When determining the anhydride concentration, it is not necessary to discriminate between both products and thus the whole signal area assigned to the corresponding benzyl amide is considered for calculation. This method yielded much higher quality data that could be fitted with first-order decay. Another advantage of the quenching method became apparent. Without the quenching chemistry, each data point in the time series required the preparation of a new sample. For example, when the 15 minute HPLC method was finished with determining the concentration anhydride in the first data point (minute 1), all anhydride had hydrolyzed, and a new sample had to be started to measure the concentration in a second data point. With the quenching method, each time interval, an aliquot could be injected into the benzylamine solution. That solution could be stored and analyzed later. Finally, it is worth mentioning that the reaction of the anhydride with the benzylamine is fast, and all anhydride is converted within a minute after addition (Figure S3). Since full conversion was detected, we conclude that the amide formation outcompetes the accelerated hydrolysis reaction at an elevated pH. With this simple quenching method, we determined the half-life of the anhydride to be two minutes under these conditions.

Besides quenching the deactivation reaction, all other reactions in the cycle have to be quenched too. To test the effects of benzylamine on the activation reaction, we reacted N-Boc-L-aspartate (**1**) in aqueous buffer at pH 6 with EDC. After 1 minute, the entire solution was quenched by the addition of benzylamine. We measured that the quenched sample contained 6 mM of N-Boc-aspartate (**1**), 3 mM of amide (Figure 3A–B), and 36 mM of EDC (Figure 3C–D). We were interested in the

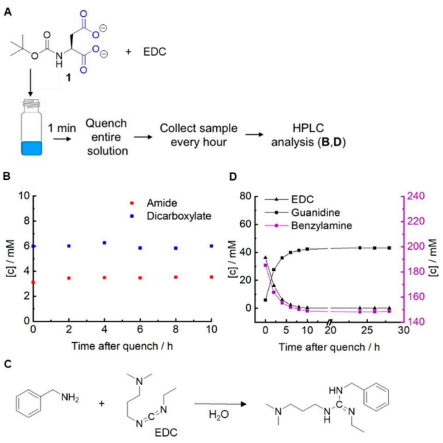

Figure 3. Does the quench stop our activation reaction? A) The activation reaction converts the dicarboxylate of **1** into its corresponding anhydride by the consumption of EDC. B) The concentration of dicarboxylate and N-benzyl amide against time after quenching the activation reaction. C) The reaction of EDC with benzylamine to form a stable guanidine-derivative. D) The concentration of EDC, benzylamine, and the guanidine-derivative against time as measured by HPLC. The markers represent HPLC data, and the lines are added to guide the eye.

activity of the remaining EDC in the quenched solution, *i.e.*, is EDC in the presence of benzylamine able to form new anhydride and thereby compromise our measurements? To test the reactivity of the remaining EDC, we followed the concentration of **1**, its corresponding N-benzyl amide, and EDC over the course of 10 hours at room temperature. We were surprised to find that the EDC was fully consumed within 10 hours, but no conversion of new anhydride or amide was apparent (Figure 3A–B). We explain the lack of the conversion of the acid to the anhydride by a sudden increase in pH upon quenching the reaction mixture (Figure S4). The O-acyl urea formation is highly pH-dependent, with the highest reactivity around pH 2–4, depending on the carboxylic acid (Figure S5). At the pH of the quenching solutions, the activation reaction was completely halted. In contrast, we found that EDC reacted with benzylamine to form its guanidine-derivative (Figure 3C–D). The HPLC data shows that this transformation was completed within 10 hours. Because this reaction did not produce further side products, the concentration EDC at the time of the quench could be determined accurately by measuring the remaining concentration of EDC and the concentration of the guanidine derivative.

Next, we set out to test the quenching method on the full chemical reaction cycle using EDC as fuel and **1** as a precursor (Figure 4A). To analyze the kinetics of the chemical reaction cycle, we added 100 mM EDC to 20 mM precursor dissolved in 200 mM MES buffer at pH 3.5 and, every minute, quenched an aliquot of the mixture. The quenched samples were stored overnight and analyzed by HPLC (Figure 4A–C). One downside of our method is that it cannot discriminate between the intermediate O-acyl urea or the anhydride product, *i.e.*, both will react to form the benzylamide. Nevertheless, due to the fast conversion of the O-acyl urea to the anhydride, only very low concentrations of the O-acyl urea are present in the reaction mixture. For example, our model calculates the concentration O-acyl urea to 0.63 mM in comparison to 17 mM of anhydride within the first minute. Thus, less than 5 % of the amide formed stems from the O-acyl urea.

The assay showed that in the reaction mixture, the EDC concentration dropped rapidly in the first minute, after which it decayed linearly. As the EDC was being consumed, the anhydride concentration rapidly increased to 16 mM, while the precursor concentration dropped to 4 mM. Because a large fraction of the precursor was converted, the anhydride concentration settled to a pseudo-steady state. The pseudo-steady state implies that activation and deactivation occur at almost equal rates. This state was sustained for about 5 minutes, which is the time until most EDC had reacted. After that, the concentration anhydride decayed until it had all hydrolyzed. When we used a simple kinetic model, we could accurately predict the concentrations of EDC, precursor, and anhydride. From the kinetic model, we calculated an anhydride half-life (ln (2)/$k_{hydrolysis}$) of 50 seconds. This value differs from the above mentioned 2 minutes because of the increased water content. It is worth mentioning that we found no evidence of self-assembly when we mixed 20 mM precursor with 100 mM EDC.

We tested if the supramolecular structures formed by the activated precursor molecules interfere with our quenching method. Specifically, we were interested to see whether the benzylamine quench was sufficiently fast to simultaneously dissolve and amidate the anhydrides in an assembly. In contrast to the experiment above, we used 100 mM of N-Boc-L-aspartate (**1**) precursor with 100 mM of EDC. The higher precursor concentration allows for the formation of more anhydride than the experiment above. We found that the solution almost immediately turned turbid (Figure 4D). The increased turbidity

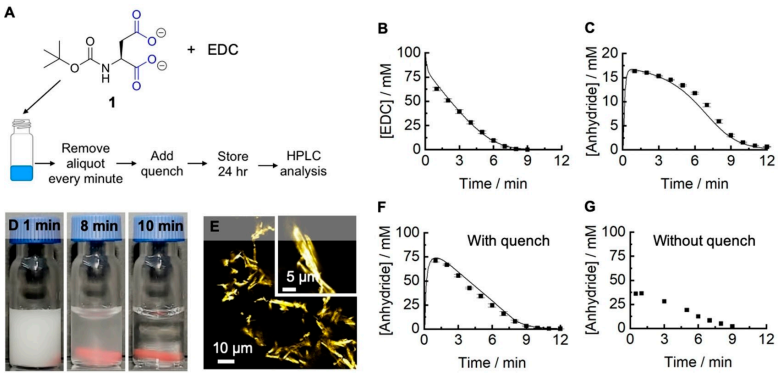

Figure 4. Analysis of a carbodiimide fueled reaction cycle with N-Boc-L-aspartate (**1**) as a precursor. A) Schematic overview of the quenching experiment. The concentration of B) EDC and C) anhydride against time as measured by HPLC. The initial concentration was 100 mM in EDC and 20 mM in **1**. The markers represent HPLC data, and the lines are predicted values from our kinetic model. The error bars depict the standard deviation from the average (n = 3). D) Time-lapse photography of a solution of 100 mM EDC and 100 mM N-Boc-L-aspartate (**1**). E) Fluorescence microscopy micrographs of the turbid solution. F) The concentration anhydride against time as measured by injecting quenched aliquots into HPLC. G) The concentration anhydride against time as measured by directly injecting the reaction mixture into HPLC.

was present for roughly eight minutes, after which the solutions turned clear. Fluorescence microscopy of these turbid solutions revealed the presence of micron-sized rectangular crystals, which explains the increased turbidity (Figure 4E). We measured the concentration anhydride and fuel with the method described above. It is worth noting that the turbid solution turned transparent immediately upon injecting it in the benzylamine quenching solution, pointing to a rapid dissolution of the anhydride. We found that all fuel was consumed within two minutes (Figure S6), after which the anhydride decayed linearly (Figure 4F). We explain the linear decay with a self-protection mechanism that we described in earlier work.[22b] In the self-protection mechanism, the hydrolysis reaction only takes place on the fraction of anhydride that remains in solution after self-assembly. Thus, when the concentration anhydride passes its solubility, the hydrolysis converts from first-order kinetics to zero-order kinetics. We incorporated the self-protection mechanism into our kinetic model and could accurately predict the HPLC data. Importantly, the same rate constants were used in the model as described above, which is a good indication that the benzylamine quench is effective in samples that contain assemblies or not.

Finally, we aim to show the generality of our quenching method, both for different types of activated carboxylate precursors and different types of assemblies. First, we tested the precursor pentanoate (**2**), which forms the non-cyclic pentanoic anhydride (C_5C_5) when activated by EDC. Several research groups, including ours, have used symmetric anhydride formed carbodiimide-fueled chemical reaction cycles to drive dissipative self-assembly.[19b,21a,23a] Given the slightly different reactivities of these anhydrides, we were first interested in whether our quenching method would yield the N-benzyl amide. We prepared a solution of 10 mM pentanoic anhydride in acetonitrile and quenched the mixture with benzylamine. The approximately 10 mM of amide measured (Figure S7) serves as strong evidence that the quenching method can also be adapted to anhydrides containing weaker electrophilic centers. To test if the method also works on the fueled reaction cycle with pentanoate (**2**) as the precursor, we fueled 300 mM of **2** at pH 6.0 with 10 mM of EDC and tested the evolution of the anhydride and EDC concentration (Figure 5A, S8). These conditions reflect earlier work we carried out on this precursor.[19c] Even though the solution forms droplets (Figure 5B–C), we found that the quenching method yielded reliable data.

Fmoc-protecting groups are frequently used in the design of self-assembling peptides,[28] and have also been used in the carbodiimide-driven reaction cycles.[19a,22b] We thus tested our quenching method on peptide precursors that contained this group, *i.e.*, N-Fmoc-L-glutamate (**3**) and N-Fmoc-Ala-Val-glutamate (**4**). It should be noted that these protecting groups are labile under basic conditions, which resulted in partial deprotection by our quenching chemistry. We showed that the deprotection can be reduced to an insignificant amount by using a less concentrated quenching solution, such that the pH does not exceed 9 (Figure S9, S10).

Nevertheless, the benzylamine remained in a 20-fold excess relative to the maximum anhydride concentration. In addition

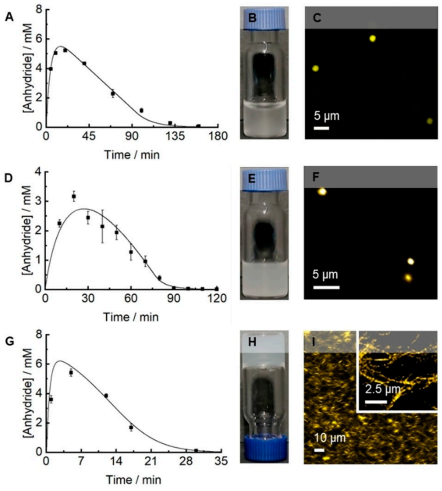

Figure 5. Analysis of different self-assembling reaction networks by our quenching method. A–C) Dissipative self-assembly of 300 mM pentanoate (**2**) fueled with 10 mM EDC. A) The concentration anhydride against time as measured by HPLC. The markers represent HPLC data, the lines are predicted values from our kinetic model. The error bars depict the standard deviation from the average (n = 3). B) Photograph of a turbid solution. C) Fluorescence microscopy micrograph of the turbid solution. D–F) Dissipative self-assembly of 10 mM N-Fmoc-L-glutamate (**3**) fueled with 10 mM EDC. D) The concentration anhydride against time as measured by HPLC. E) Photograph of a turbid solution. F) Fluorescence microscopy of the turbid solution. G–I) Dissipative self-assembly of 10 mM N-Fmoc-Ala-Val-glutamate (**4**) fueled with 50 mM EDC. H) Photograph of a self-sustaining hydrogel. I) Fluorescence microscopy of the hydrogel.

to that we stored the quenched samples at 8 C. With the adjusted method, we measured the kinetics of the reaction cycle when 10 mM N-Fmoc-L-glutamate (**3**) was fueled with 10 mM EDC at pH 6.0 (Figure 5D, S11). Moreover, **3** self-assembled into colloids in response to the fuel, further demonstrating the versatility of our method (Figure 5E–F). To further demonstrate the generality of our method, we measured the kinetics of the chemical reaction cycle with N-Fmoc-Ala-Val-glutamate (**4**) as a precursor at pH 6.0. Upon EDC fueled activation, the peptide precursor can self-assemble into fibers, which subsequently yields a hydrogel (Figure 5H–I).[19a] We were particularly interested if the increased viscosity of the material interfered with our quenching method. We used a wide-bore pipette to remove samples and analyzed those by HPLC after applying our quenching method (Figure 5G, S12). The kinetic data showed close correspondence to the predictions by our kinetic model.

Why should one use the benzylamine quenching method? The strongest argument in favor of the benzylamine quench is that it vastly improves the data quality. This argument is particularly valid for labile anhydrides that hydrolyze during the analysis. Even for somewhat more stable anhydrides (*e.g.*, C_5C_5,

$t_{1/2} = 12$ minutes), we found improvement in data quality when applying the quenching method (Figure S13). Furthermore, a strong argument for the quenching method is that it vastly facilitates data acquisition. Without the quench, the rate of data acquisition was determined by the length of the analysis method. Specifically, we can inject one sample in the HPLC every ~20 minutes. Thus, our data acquisition is limited to ~0.05 data points min^{-1}. For ^{1}H-NMR that is somewhat faster, providing one acquisition every ~2 minutes (0.5 data points min^{-1}). Due to the quenching method, the limiting factor of data acquisition frequency is the pipetting frequency. For example, with our pipetting robot, the highest data acquisition frequency is now 6 data points min^{-1} (Figure S16). That means that samples can be collected in real-time and analyzed overnight, which significantly accelerates data throughput. Finally, an argument in favor of the benzylamine quenching method is that it further facilitates the detection of the anhydride product by converting an anhydride into the N-benzyl amide. The benzyl ring vastly facilitates the detection of the product by HPLC because of its absorbance at 254 nm.

The arguments in favor of using quenching chemistry above apply to other chemically fueled reaction cycles, too.[21a,24,29] To aid the broader community of scientists exploring the field of chemically fueled self-assembly, we set out some preliminary design rules for such quenching chemistry.

Firstly, quenching chemistry should be identified that immediately stops both the activation and deactivation reaction. If the activation is partly deactivated, the concentration product is overestimated. Likewise, the product is underestimated in case of an insufficient quench of the deactivation. To test whether the deactivation quench is quantitative and sufficiently fast, the pure product should be synthesized and added to the quenching solution (See the experiment in Figure S3, S7). In the case of instantaneous quenching, the product concentration matches the amount added. Similarly, to test if the activation reaction is completely quenched, a solution of the precursor and fuel should be quenched and analyzed immediately after, and several hours after addition of the quench. If the product concentrations are similar, the activation is completely stopped (See the experiment in Figure 3B).

Secondly, the quenching chemistry of the activation and deactivation should be orthogonal to each other. Finding such chemistry can be challenging. We thus describe our thought process when designing the benzylamine quench. The deactivation is a pseudo-first-order reaction (hydrolysis). That means that, realistically, there is only one reagent that can be quenched, *i.e.,* the anhydride. That severely limits the possible chemistry, and we therefore first designed chemistry for quenching the deactivation, *i.e.,* reaction with benzylamine. The activation is a second-order reaction between fuel and precursor. That offers two possibilities to quench the reaction, *i.e.*, we decrease the reactivity of the precursor or the fuel. We thus tested possible chemistries while keeping in mind the orthogonality to the benzylamine quench of the deactivation. We chose to decrease the reactivity of the fuel by increasing the pH, which is orthogonal.

Finally, to quench reactions, there are several possible chemical strategies. One can add a reactive species that yields a stable product (benzylamine in the case of the anhydride) or one can change the environmental conditions to quench reactions (change the pH or temperature).

We introduced a method to quench a carbodiimide-driven reaction cycle. This reaction cycle is frequently used by us and others to drive the dissipative self-assembly of molecules or nanoparticles. We found that the quenching method can successfully stop all reactions in the cycle. Moreover, we described that the quench works both for reaction cycles that yield assemblies or not. Finally, we showed that the quench can be applied to a diverse set of anhydrides. We trust that the method will be further used to more accurately, more conveniently, and more reliably analyze carbodiimide-driven chemical reaction cycles. Moreover, we believe that our work also lays the groundwork for the development of quenching methods for other reaction cycles that are used to fuel dissipative assemblies. In future work, we aim to further facilitate the quench using fluorogenic amines. In such an assay, the concentration anhydride can be read-out using plate reader fluorescent assays. Finally, we foresee that the described quenching method will help with the further acceleration of the reaction cycles and the search for new dynamic behavior of chemically fueled assemblies.

Acknowledgements

This work was supported by the Technische Universität München-Institute for Advanced Study , funded by the German Excellence Initiative and the European Union Seventh Framework Programme under grant agreement n 291763. F.S. acknowledges funding from the Deutsche Forschungsgemeinschaft (DFG, German Research Foundation) under Germany's Excellence Strategy – EXC-2094 – 390783311. J.B. is grateful for funding by the European Research Council (ERC starting grant) under 852187. Open access funding enabled and organized by Projekt DEAL.

Conflict of Interest

The authors declare no conflict of interest.

Keywords: chemical fuels · dissipative self-assembly · kinetics · reaction cycles

[1] S. I. Stupp, L. C. Palmer, *Chem. Mater.* **2013**, *26*, 507.
[2] M. P. Hendricks, K. Sato, L. C. Palmer, S. I. Stupp, *Acc. Chem. Res.* **2017**, *50*, 2440.
[3] S. Yagai, T. Iwashima, K. Kishikawa, S. Nakahara, T. Karatsu, A. Kitamura, *Chem. Eur. J.* **2006**, *12*, 3984.
[4] K. Yazaki, L. Catti, M. Yoshizawa, *Chem. Commun. (Cambridge, U. K.)* **2018**, *54*, 3195.
[5] A. H. Groschel, A. Walther, *Angew. Chem. Int. Ed.* **2017**, *56*, 10992.
[6] M. Kellermann, W. Bauer, A. Hirsch, B. Schade, K. Ludwig, C. Bottcher, *Angew. Chem. Int. Ed.* **2004**, *43*, 2959.

[7] E. P. Holowka, D. J. Pochan, T. J. Deming, *J. Am. Chem. Soc.*, **2005**, *127*, 12423.
[8] S. Sacanna, M. Korpics, K. Rodriguez, L. Colon-Melendez, S. H. Kim, D. J. Pine, G. R. Yi, *Nat. Commun.* **2013**, *4*, 1688.
[9] a) M. de Loos, B. L. Feringa, J. H. van Esch, *Eur. J. Org. Chem.* **2005**, *2005*, 3615; b) R. J. Macfarlane, B. Lee, M. R. Jones, N. Harris, G. C. Schatz, C. A. Mirkin, *Science* **2011**, *334*, 204.
[10] N. Singh, G. J. M. Formon, S. De Piccoli, T. M. Hermans, *Adv. Mater.* **2020**, 1906834.
[11] S. De, R. Klajn, *Adv. Mater.* **2018**, *30*, 1706750.
[12] A. A. Hyman, S. Salser, D. N. Drechsel, N. Unwin, T. J. Mitchison, *Mol. Biol. Cell* **1992**, *3*, 1155.
[13] D. K. Fygenson, E. Braun, A. Libchaber, *Phys. Rev.* **1994**, *50*, 1579.
[14] a) R. G. Burns, *Biochem. J.* **1991**, *277*, 239; b) H. Bowne-Anderson, M. Zanic, M. Kauer, J. Howard, *BioEssays* **2013**, *35*, 452.
[15] J. Leira-Iglesias, A. Tassoni, T. Adachi, M. Stich, T. M. Hermans, *Nat. Nanotechnol.* **2018**, *13*, 1021.
[16] J. Boekhoven, W. E. Hendriksen, G. J. Koper, R. Eelkema, J. H. van Esch, *Science* **2015**, *349*, 1075.
[17] I. Colomer, A. Borissov, S. P. Fletcher, *Nat. Commun.* **2020**, *11*, 176.
[18] J. Boekhoven, A. M. Brizard, K. N. Kowlgi, G. J. Koper, R. Eelkema, J. H. van Esch, *Angew. Chem. Int. Ed.* **2010**, *49*, 4825.
[19] a) M. Tena-Solsona, B. Riess, R. K. Grotsch, F. C. Lohrer, C. Wanzke, B. Kasdorf, A. R. Bausch, P. Muller-Buschbaum, O. Lieleg, J. Boekhoven, *Nat. Commun.* **2017**, *8*, 15895; b) L. S. Kariyawasam, C. S. Hartley, *J. Am. Chem. Soc.* **2017**, *139*, 11949; c) M. Tena-Solsona, C. Wanzke, B. Riess, A. R. Bausch, J. Boekhoven, *Nat. Commun.* **2018**, *9*, 2044.
[20] C. Wanzke, A. Jussupow, F. Kohler, H. Dietz, V. R. I. Kaila, J. Boekhoven, *ChemSystemsChem* **2019**, *2*, e1900044.
[21] a) S. Panja, B. Dietrich, D. J. Adams, *ChemSystemsChem* **2019**, *2*, e1900038; b) L. S. Kariyawasam, J. C. Kron, R. Jiang, A. J. Sommer, C. S. Hartley, *J. Org. Chem.* **2020**, *85*, 682; c) B. Zhang, I. M. Jayalath, J. Ke, J. L. Sparks, C. S. Hartley, D. Konkolewicz, *Chem. Commun. (Cambridge, U. K.)* **2019**, *55*, 2086.
[22] a) C. Wanzke, M. Tena-Solsona, B. Rieß, L. Tebcharani, J. Boekhoven, *Mater. Horiz.* **2020**; b) B. Riess, C. Wanzke, M. Tena-Solsona, R. K. Grotsch, C. Maity, J. Boekhoven, *Soft Matter* **2018**, *14*, 4852.
[23] a) R. K. Grotsch, A. Angi, Y. G. Mideksa, C. Wanzke, M. Tena-Solsona, M. J. Feige, B. Rieger, J. Boekhoven, *Angew. Chem. Int. Ed.* **2018**, *57*, 14608; b) R. K. Grotsch, C. Wanzke, M. Speckbacher, A. Angi, B. Rieger, J. Boekhoven, *J. Am. Chem. Soc.* **2019**, *141*, 9872.
[24] S. Bal, K. Das, S. Ahmed, D. Das, *Angew. Chem. Int. Ed.* **2019**, *58*, 244.
[25] Z. Feng, H. Wang, B. Xu, *J. Am. Chem. Soc.* **2018**, *140*, 16433.
[26] C. Donau, F. Späth, M. Sosson, B. Kriebisch, F. Schnitter, M. Tena-Solsona, H.-S. Kang, E. Salibi, M. Sattler, H. Mutschler, J. Boekhoven, *Nat. Commun.* **2020**, DOI 10.26434/chemrxiv.11648598.v1.
[27] J. Leira-Iglesias, A. Sorrenti, A. Sato, P. A. Dunne, T. M. Hermans, *Chem. Commun. (Cambridge, U.K.)* **2016**, *52*, 9009.
[28] R. Orbach, L. Adler-Abramovich, S. Zigerson, I. Mironi-Harpaz, D. Seliktar, E. Gazit, *Biomacromolecules* **2009**, *10*, 2646–2651.
[29] a) S. Maiti, I. Fortunati, C. Ferrante, P. Scrimin, L. J. Prins, *Nat. Chem.* **2016**, *8*, 725; b) E. Del Grosso, L. Prins, F. Ricci, *Angew. Chem. Int. Ed.* **2020**; c) A. Sorrenti, J. Leira-Iglesias, A. Sato, T. M. Hermans, *Nat. Commun.* **2017**, *8*, 15899; d) B. Fan, Y. Men, S. A. P. van Rossum, G. Li, R. Eelkema, *ChemSystemsChem* **2019**, *2*, e1900028; e) T. Heuser, A. K. Steppert, C. M. Lopez, B. Zhu, A. Walther, *Nano Lett.* **2015**, *15*, 2213; f) I. Colomer, S. M. Morrow, S. P. Fletcher, *Nat. Commun.* **2018**, *9*, 2239; g) S. M. Morrow, I. Colomer, S. P. Fletcher, *Nat. Commun.* **2019**, *10*, 1011; h) S. Dhiman, R. Ghosh, S. J. George, *ChemSystemsChem* **2019**, *2*, e1900042; i) A. Jain, S. Dhiman, A. Dhayani, P. K. Vemula, S. J. George, *Nat. Commun.* **2019**, *10*, 450; j) W. A. Ogden, Z. Guan, *ChemSystemsChem* **2019**, *2*, e1900030; k) C. S. Wood, C. Browne, D. M. Wood, J. R. Nitschke, *ACS Cent. Sci.* **2015**, *1*, 504.

Manuscript received: July 22, 2020
Accepted manuscript online: July 24, 2020
Version of record online: August 24, 2020

ChemSystemsChem

Supporting Information

A Method to Quench Carbodiimide-Fueled Self-Assembly

Fabian Schnitter and Job Boekhoven*

Author Contributions

F.S. Conceptualization:Equal; Data curation:Lead; Validation:Lead; Visualization:Lead; Writing - Original Draft:Equal; Writing - Review & Editing:Equal

Materials

N-Boc-L-aspartic acid and N-Fmoc-L-glutamic acid were purchased from Alfa-Aesar. Pentanoic acid, 1-ethyl-3-(3-dimethylaminopropyl)carbodiimide (EDC), N,N'-dicyclohexylcarbodiimide (DCC), 2-(N-morpholino)ethanesulfonic acid hydrate (MES), Nile red, benzylamine and solvents were purchased from Sigma-Aldrich. The peptide N-Fmoc-Ala-Val-glutamic acid was synthesized using solid-phase synthesis via a published procedure.[1] All components were used without further purification unless otherwise indicated. Water was obtained from a Millipore water purifier system.

Synthesis

Preparation of tert-butyl (2,5-dioxotetrahydrofuran-3-yl)carbamate.[2]

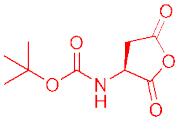

N-Boc-L-aspartic acid (2.0 g, 8.6 mmol, 1.0 equiv) was dissolved in 30 mL ethyl acetate. To this solution was added N,N'-dicyclohexylcarbodiimide (1.9 g, 9.4 mmol, 1.1 equiv) dissolved in 20 mL ethyl acetate. The reaction was stirred at 0 °C for 1 hour followed by 2 hours at room temperature. The precipitated urea side product was filtered off. From the filtrate, the solvent was removed by evaporation *in vacuo*. The crude product was recrystallized from acetone-hexane yielding 1.2 g (67%) of white crystals.

^{1}H NMR (300 MHz, DMSO-d6): δ / ppm 7.75 (d, *J* = 7.7 Hz, 1H), 4.70 – 4.40 (m, 1H), 3.22 (dd, *J* = 18.4, 10.0 Hz, 1H), 2.84 (dd, *J* = 18.4, 6.3 Hz, 1H), 1.38 (s, 9H).

^{13}C NMR (101 MHz, DMSO-d6): δ / ppm = 172.4, 170.0, 155.2, 79.6, 50.2, 34.9, 28.0.

IR (Platinum-ATR, neat): $\tilde{\nu}$ / cm^{-1} = 3352, 1689, 1516, 1409, 1367, 1288, 1249, 1167, 931, 646.

Preparation of (Z)-1-benzyl-2-(3-(dimethylamino)propyl)-3-ethylguanidine.

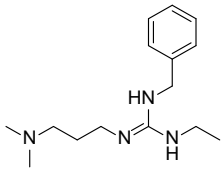

1-ethyl-3-(3-dimethylaminopropyl)carbodiimide (1.8 g, 9.2 mmol, 1.0 equiv) was dissolved in 25 mL water and benzylamine (1.0 g, 9.2 mmol, 1.0 equiv) was added directly to the solution. The reaction mixture was stirred over night at room temperature. The solvent was removed by lyophilization and the crude product was redissolved in acetonitrile/water (2%/98%). Purification was performed on a Thermofischer Dionex Ultimate 3000 equipped with a Hypersil Gold 250x21.2 mm column. A linear gradient of acetonitrile (MeCN, 2% to 98%) and water with 0.1% TFA was applied for elution. From the combined fractions, the solvent was removed by evaporation *in vacuo* and lyophilization. It was obtained 0.70 g (29%) of the product as a viscous liquid.

^{1}H NMR (300 MHz, D_2O): δ / ppm 7.60 – 7.17 (m, 5H), 4.47 (s, 2H), 3.29 (m, *J* = 8.1, 7.6 Hz, 4H), 2.73 (s, 8H), 1.86 (dq, *J* = 11.3, 5.8, 5.2 Hz, 2H), 1.18 (t, *J* = 7.2 Hz, 3H).

^{13}C NMR (101 MHz, D_2O): δ / ppm 154.2, 136.4, 129.0, 128.0, 126.7, 54.7, 44.0, 42.7, 37.9, 36.4, 23.3, 13.4.

MS-ESI: *m/z* $[M+H]^+$ calc. for $C_{15}H_{26}N_4$: 263.22, found: 263.17.

IR (Platinum-ATR, neat): $\tilde{\nu}$ / cm^{-1} = 3171, 2960, 2657, 1612, 1480, 1249, 1152, 965, 704, 626.

Methods

Sample preparation. Stock solutions of the precursor were prepared by dissolving the carboxylic acids in 200 mM MES buffer and adjusting the pH. Stock solutions of EDC were prepared by weighing in the EDC and the water. A typical concentration for the EDC stock solution was 2M. The stock solutions were prepared freshly before usage. Reaction networks were started by addition of the high concentration EDC to the precursor solution. The samples of crystal forming precursor **1** were stirred at 600 rpm.

Analysis of the reaction kinetics by HPLC. The kinetics of the chemical reaction cycles were monitored over time by means of analytical HPLC (HPLC, Thermofisher Dionex Ultimate 3000, Hypersil Gold 250x4.8 mm). A 750 *µL* sample was prepared (see general sample preparation) and placed into a screw cap HPLC vial. At predetermined time points, 50 *µL* of the sample was removed and added to a 400 mM benzylamine stock solution in water (200 mM benzylamine in acetonitrile for the Fmoc protected precursors). The diluted samples were injected into HPLC and all compounds involved in the reaction cycle were separated using a linear gradient of acetonitrile (MeCN, 2% to 98%) and water with 0.1% TFA. The quantification of the N-benzyl amides and guanidine was performed by calibrating benzylamine at λ = 254 nm. EDC was separately calibrated at λ = 220 nm. Measurements were performed at 25 °C for N-Boc-L-aspartate (**1**) and pentanoate (**2**) precursors, at 8 °C for the Fmoc protected precursors **3** and **4**.

Kinetic model. A kinetic model was used to predict the evolution of the anhydride concentration over time. The model is described in detail in our previous work.[1, 3] The rate constants we used in this work are given in Table S3. The Matlab-code we used is available here: https://github.com/BoekhovenLab/Quenching-Chemistry

Confocal Fluorescence Microscopy. Confocal fluorescence microscopy was performed on a Leica TCS SP8 confocal microscope using a x 63 water immersion objective. Samples were prepared as described above, but with 25 µM Nile red as dye. Twenty microliters of the sample were deposited on the glass slide and covered with a 12 mm diameter coverslip. Samples were excited with 543 nm laser and imaged at 580–700 nm.

ESI-MS. To align the N-benzyl amides and the guanidine correctly to the HPLC chromatogram, the compounds were collected after detection and their mass was determined. ESI-MS experiments were conducted on an LCQ Fleet Ion Trap Mass Spectrometer (Thermo Scientific). Interpretation of all recorded MS data was performed using the Thermo Xcalibur Qual Browser 2.2 SP1.48 software.

NMR. NMR spectra were recorded on a Bruker AV300 or a Bruker AV-NEO 400 instrument. Chemical shifts are reported as δ-values in ppm relative to the deuterated solvent peak: $(CD_3)_2SO$ (δH: 2.05; δC: 39.50) or D_2O (δH: 4.79). For the denotation of the observed signal

multiplicities, the following abbreviations were used: s (singlet), d (doublet), dd (doublet of doublets), t (triplet), dq (doublet of quartets), m (multiplet).

Time-lapse photography. In a 2 mL HPLC-vial, 500 - 750 µL of a precursor solution fueled with EDC were imaged with a high-definition camera. Time-lapse software was programmed to image the sample in a 1-minute interval.

Fourier-Transform Infrared Spectroscopy (FTIR). FTIR spectra were recorded on a Bruker Vertex 70 FTIR using a Platinum ATR from Bruker. The main transmission peaks are reported from 4000 cm^{-1} to 400 cm^{-1}.

5

Supplementary Figures

Figure S1. Reactions involved in the chemical reaction cycle.

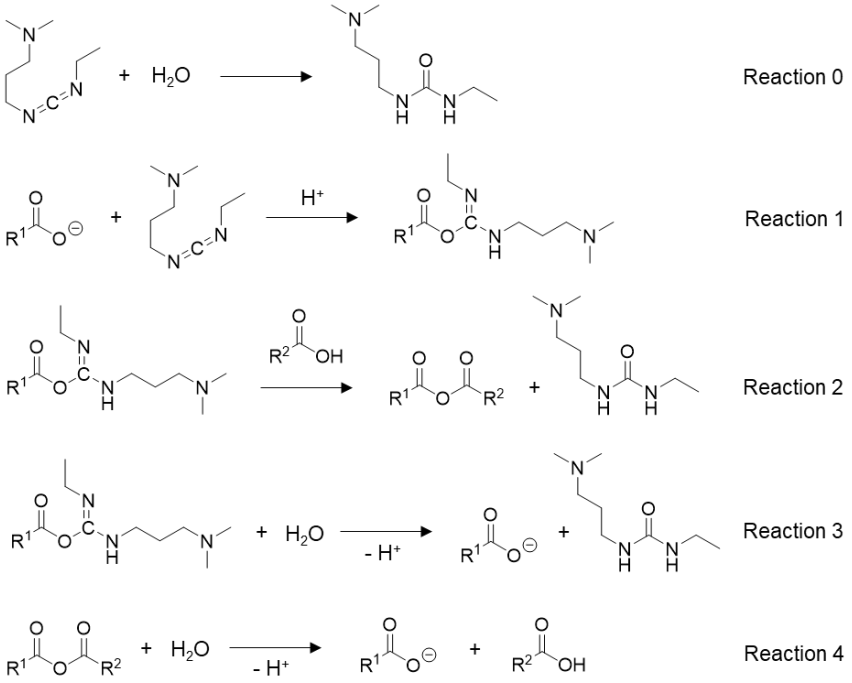

Figure S1. Reactions involved in the chemical reaction cycle. Reaction 0 represents the direct hydrolysis of EDC carbodiimide. Reaction 1 corresponds to the formation of O-acyl urea by reaction with EDC. Reaction 2 corresponds to the formation of the anhydride. Reaction 3 shows the direct hydrolysis of the O-acyl urea. Reaction 4 shows the hydrolysis of the anhydride.

Figure S2. On-column hydrolysis of anhydride during separation.

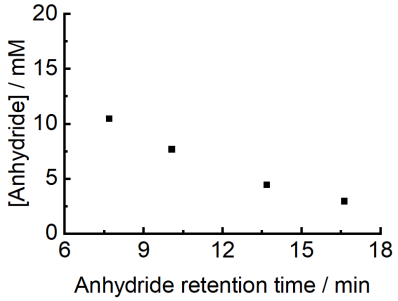

Figure S2. The concentration anhydride as a function of its retention time on a reversed-phase HPLC column. 20 mM of N-Boc-L-aspartic anhydride dissolved in acetonitrile was injected. Retention times were prolonged by decreasing the acetonitrile:water gradient.

Figure S3. Yield and conversion time of (1)-N-benzyl amide formation.

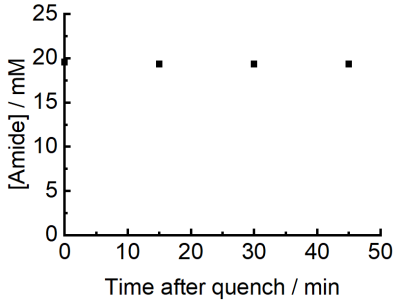

*Figure S3. The concentration (**1**)-N-benzyl amide as a function of time after adding the quenching solution. To a 100 mM of N-Boc-L-aspartic anhydride solution in acetonitrile, a 400 mM stock solution of benzylamine in water was added resulting in a final concentration of 20 mM N-Boc-L-aspartic anhydride. The sample was injected into HPLC right after dilution.*

Figure S4. The effect of injected benzylamine on the pH of the reaction mixture.

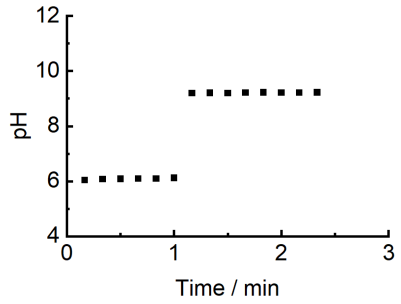

*Figure S4. The pH as a function of time. To a 20 mM solution of N-Boc-L-aspartate (**1**) in 0.2 M MES buffer at pH 6, 100 mM of EDC was added. After one minute, 400 mM of benzylamine was added to quench the cycle.*

Figure S5. The pH-dependence of the EDC activation reaction.

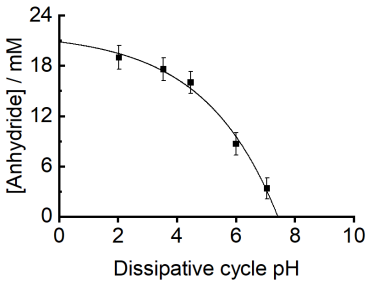

*Figure S5. The anhydride concentration as a function of pH. 20 mM of N-Boc-L-aspartate (**1**) stock solutions in 0.2 M MES at different pH were prepared. To these stock solutions, 100 mM of EDC was added. After one minute, the cycle was quenched by addition of 400 mM of benzylamine. The anhydride yield was determined by means of the N-benzyl amide detected by HPLC. The markers represent HPLC data, the line represents a guide for the eye. The error bars show the standard deviation from the average (n = 3).*

Figure S6. EDC consumption by N-Boc-L-aspartate (1).

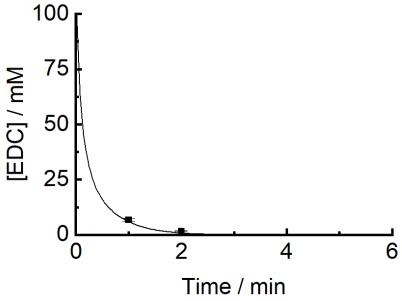

*Figure S6. The concentration EDC as a function of time. To a 100 mM solution of N-Boc-L-aspartate (**1**) in 0.2 M MES pH 3.5, 100 mM of EDC was added. Every minute, aliquots were taken and injected into a 400 mM benzylamine solution. The concentration EDC was measured by means of EDC remained in solution and concentration of formed guanidine-derivative. The markers represent HPLC data, the line represents predicted values from our kinetic model. The error bars show the standard deviation from the average (n = 3).*

Figure S7. Yield and conversion time of (2)-N-benzyl amide formation.

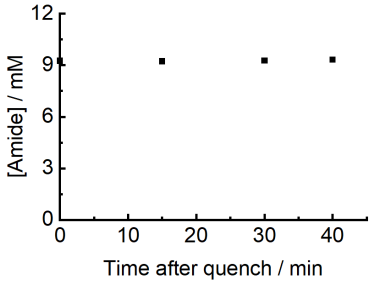

*Figure S7. The concentration (**2**)-N-benzyl amide as a function of time after adding the quenching solution. To a 50 mM of pentanoic anhydride solution in acetonitrile, a 400 mM stock solution of benzylamine in water was added resulting in an end concentration of 10 mM regarding pentanoic anhydride. The sample was injected into HPLC right after dilution.*

Figure S8. EDC consumption by pentanoate (2).

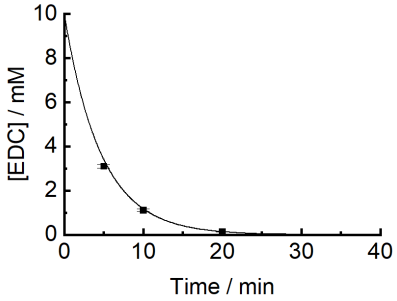

*Figure S8. The concentration EDC as a function of time. To a 300 mM solution of pentanoate (**2**) in 0.2 M MES pH 6, 10 mM of EDC was added. Aliquots were taken and injected into a 400 mM benzylamine solution. The concentration EDC was measured by means of EDC remained in solution and concentration of formed guanidine. The markers represent HPLC data, the line represents predicted values from our kinetic model. The error bars show the standard deviation from the average (n = 3).*

Figure S9. The Fmoc deprotection kinetics of N-Fmoc-L-glutamate (3) at elevated pH.

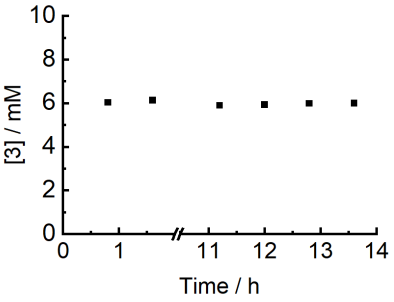

*Figure S9. The concentration of precursor **3** as a function of time. To a 10 mM solution of N-Fmoc-glutamate (**3**) in 0.2 M MES pH 6, a 200 mM solution of benzylamine in acetonitrile was added (1:1). The samples were stored at 8 °C and the amount of deprotection was estimated by monitoring the concentration of **3** by HPLC.*

Figure S10. The Fmoc deprotection kinetics of N-Fmoc-Ala-Val-glutamate (4) at elevated pH.

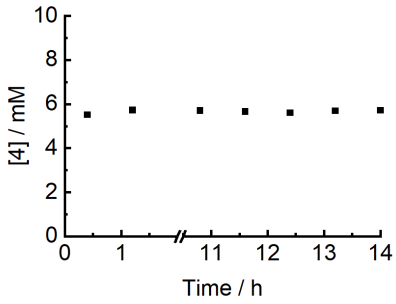

*Figure S10. The concentration of precursor **4** as a function of time. To a 10 mM solution of N-Fmoc-Ala-Val-glutamate (**4**) in 0.2 M MES pH 6, a 200 mM solution of benzylamine in acetonitrile was added (1:1). The samples were stored at 8 °C and the amount of deprotection was estimated by monitoring the concentration of **4** by HPLC.*

Figure S11. EDC consumption by N-Fmoc-L-glutamate (3).

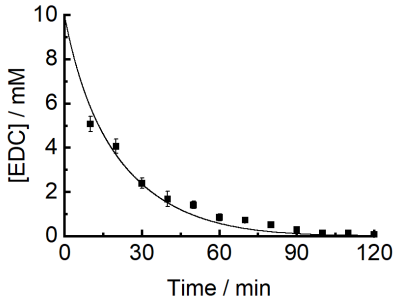

*Figure S11. The concentration EDC as a function of time. To a 10 mM solution of N-Fmoc-L-glutamate (**3**) in 0.2 M MES pH 6, 10 mM of EDC was added. Every 12 minutes, aliquots were taken and injected into a 200 mM benzylamine solution. The concentration EDC was measured by means of EDC remained in solution and concentration of formed guanidine. The markers represent HPLC data, the line represents predicted values from our kinetic model. The error bars show the standard deviation from the average (n = 3).*

Figure S12. EDC consumption by N-Fmoc-Ala-Val-glutamate (4).

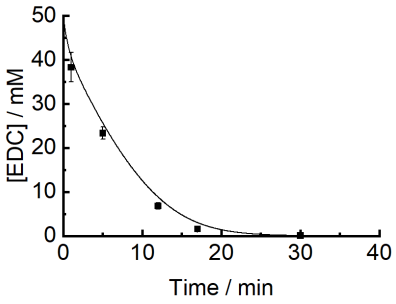

*Figure S12. The concentration EDC as a function of time. To a 10 mM solution of N-Fmoc-Ala-Val-glutamate (**4**) in 0.2 M MES pH 6, 50 mM of EDC was added. The reaction cycle was quenched by the addition of 200 mM benzylamine. The concentration EDC was measured by means of EDC remained in solution and concentration of formed guanidine. The markers represent HPLC data, the line represents predicted values from our kinetic model. The error bars show the standard deviation from the average (n = 3).*

Figure S13. Comparing the quenching method with data obtained from direct HPLC injections.

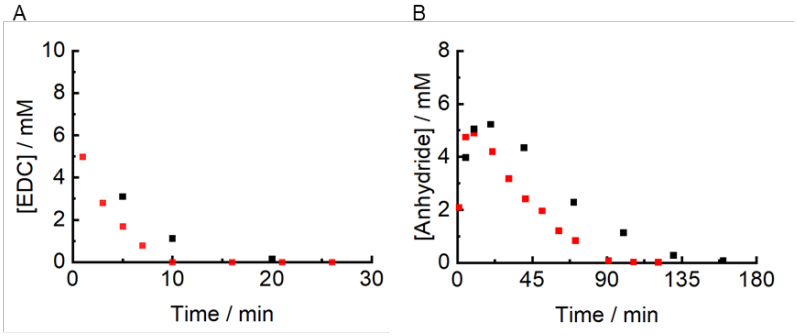

*Figure S13. The concentration A) EDC and B) anhydride against time when fueling 300 mM pentanoate (**2**) with 10 mM EDC. The black markers represent concentrations determined by the quenching method, whereas the red markers represent data obtained by direct injections into HPLC.*

Figure S14. Comparing the quenching method with data obtained from direct HPLC injections.

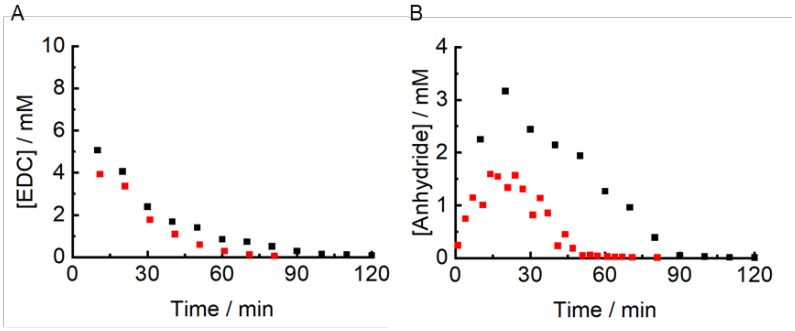

*Figure S14. The concentration A) EDC and B) anhydride against time when fueling 10 mM N-Fmoc-L-glutamate (**3**) with 10 mM EDC. The black markers represent concentrations determined by the quenching method, whereas the red markers represent data obtained by direct injections into HPLC.*

Figure S15. Comparing the quenching method with data obtained from direct HPLC injections.

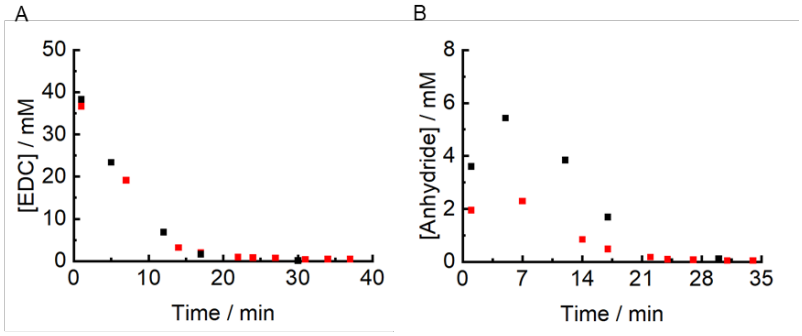

*Figure S15. The concentration A) EDC and B) anhydride against time when fueling 10 mM N-Fmoc-Ala-Val-glutamate (**4**) with 50 mM EDC. The black markers represent concentrations determined by the quenching method, whereas the red markers represent data obtained by direct injections into HPLC.*

Figure S16. Frequency of the data acquisition.

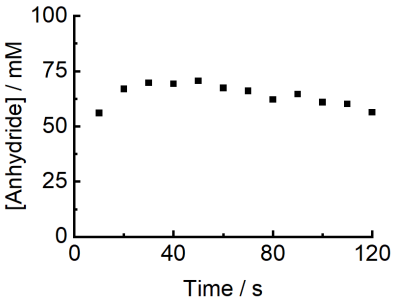

*Figure S16. The concentration anhydride as a function of time. To a 100 mM solution of N-Boc-L-aspartate (**1**) in 0.2 M MES pH 3.5, 100 mM of EDC was added. Every 10 seconds, aliquots were taken and injected into a 400 mM benzylamine solution. The concentration anhydride was determined by means of measured benzyl amide.*

Figure S17. Representative HPLC traces of the quenched reaction cycle.

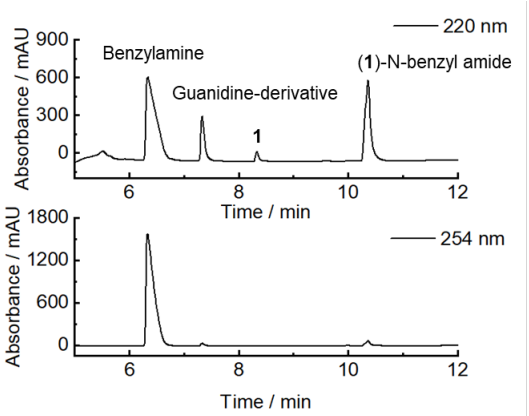

*Figure S17. HPLC traces of 100 mM N-Boc-L-aspartate (**1**) fueled with 100 mM EDC. The traces reflect the sample quenched at 3 min and stored at room temperature for 24 h. The EDC consumption and anhydride evolution were monitored by means of guanidine and amide respectively at 254 nm.*

Figure S18. Representative HPLC traces of the quenched reaction cycle.

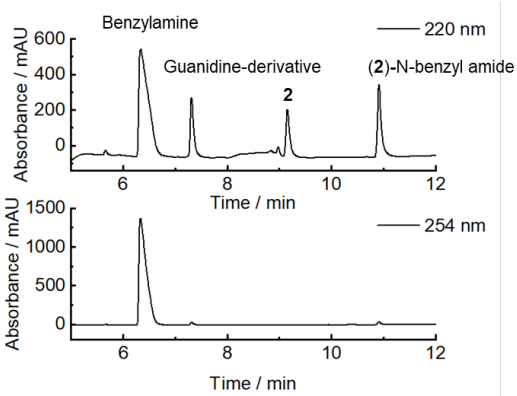

*Figure S18. HPLC traces of 300 mM pentanoate (**2**) fueled with 100 mM EDC. The traces reflect the sample quenched at 5 min and stored at room temperature for 24 h. The EDC consumption and anhydride evolution were monitored by means of guanidine and amide respectively at 254 nm.*

Figure S19. Representative HPLC traces of the quenched reaction cycle.

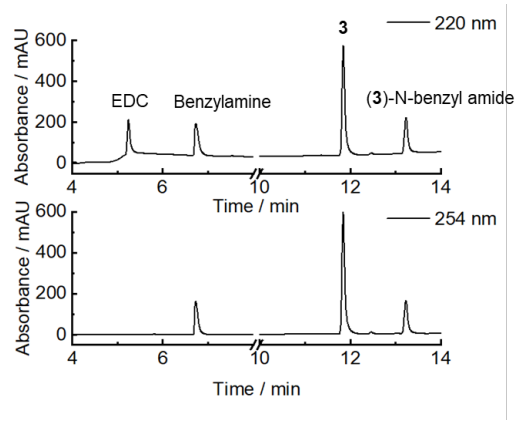

*Figure S19. HPLC traces of 10 mM N-Fmoc-L-glutamate (**3**) fueled with 10 mM EDC. The traces reflect the sample quenched at 10 min and injected directly. The EDC consumption was monitored at 220 nm. The anhydride evolution was monitored by means of amide at 254 nm.*

Figure S20. Representative HPLC traces of the quenched reaction cycle.

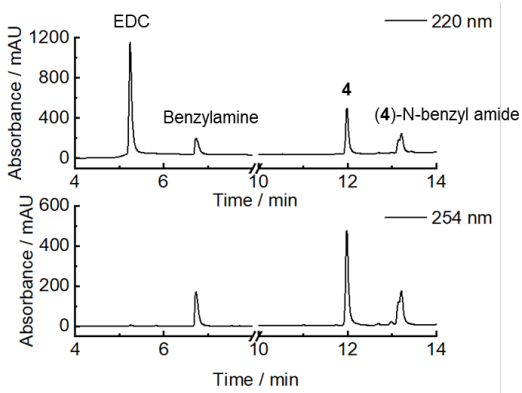

*Figure S20. HPLC traces of 10 mM N-Fmoc-Ala-Val-glutamate (**4**) fueled with 50 mM EDC. The traces reflect the sample quenched at 1 min and injected directly. The EDC consumption was monitored at 220 nm. The anhydride was monitored by means of amide at 254 nm.*

Supplementary Tables

Supplementary Table 1. Characterization of the main components applied in the reaction cycle by HPLC.

Name	Injection volume	HPLC retention time	HPLC calibration value
EDC	1 µL	5.2 min	5.09 mAU.mM^{-1} (220 nm)
Benzylamine	10 µL	6.3 min	1.62 mAU.mM^{-1} (254 nm)
1	10 µL	8.3 min	1.16 mAU.mM^{-1} (220 nm)
2	10 µL	9.2 min	N/A
3	1 µL	11.8 min	12.77 mAU.mM^{-1} (254 nm)
4	1 µL	12.0 min	12.77 mAU.mM^{-1} (254 nm)

Supplementary Table 2. Characterization of the main components formed in the reaction cycle by HPLC and ESI-MS. The calibration value of the guanidine-derivative was determined being 1.51 mAU.mM^{-1} (10 µL injection, 254 nm).

Name	HPLC ret. time	Mass calculated	Mass found
Guanidine-derivative	7.3 min	263.22 g.mol^{-1} $[M+H]^+$	263.17 g.mol^{-1}
(**1**)-Anhydride	10.0 min	N/A	N/A
(**1**)-N-benzyl amide	10.4 min	323.15 g.mol^{-1} $[M+H]^+$	322.73 g.mol^{-1}
(**2**)-N-benzyl amide	10.9 min	192.14 g.mol^{-1} $[M+H]^+$	192.2 g.mol^{-1}
(**3**)-N-benzyl amide	13.2 min	459.19 g.mol^{-1} $[M+H]^+$	459.1 g.mol^{-1}
(**4**)-N-benzyl amide	13.2 min	629.30 g.mol^{-1} $[M+H]^+$	629.2 g.mol^{-1}

Supplementary Table 3. k-values for all the reactions described in our kinetic model. The rate constant for k_0 was set to 0.135x10^{-4} sec^{-1}.

	k_1 / M^{-1}.sec^{-1}	**k_2 / sec^{-1}**	**k_3 / sec^{-1}**	**k_4 / sec^{-1}**	**Half-life of anhydride (calculated by: ln(2)/k_4)**	**Solubility**	**CAC**
	2nd order	1st order	1st order	1st order			
1	6.0x10^{-1}	0.60*k_1	0.0070*k_1	1.4x10^{-2}	0.83 min	12 mM	30 mM
2	6.0x10^{-3}	10*k_1	5.0*k_1	1.0x10^{-3}	12 min	1.0 mM	1.0 mM
3	5.0x10^{-2}	3.0*k_1	1.5*k_1	2.6x10^{-3}	4.4 min	0.5 mM	0.5 mM
4	2.5x10^{-1}	5.0*k_1	2.0*k_1	7.0x10^{-3}	1.7 min	N/A	N/A

NMR-Spectra

NMR-Spectra of tert-butyl (2,5-dioxotetrahydrofuran-3-yl)carbamate

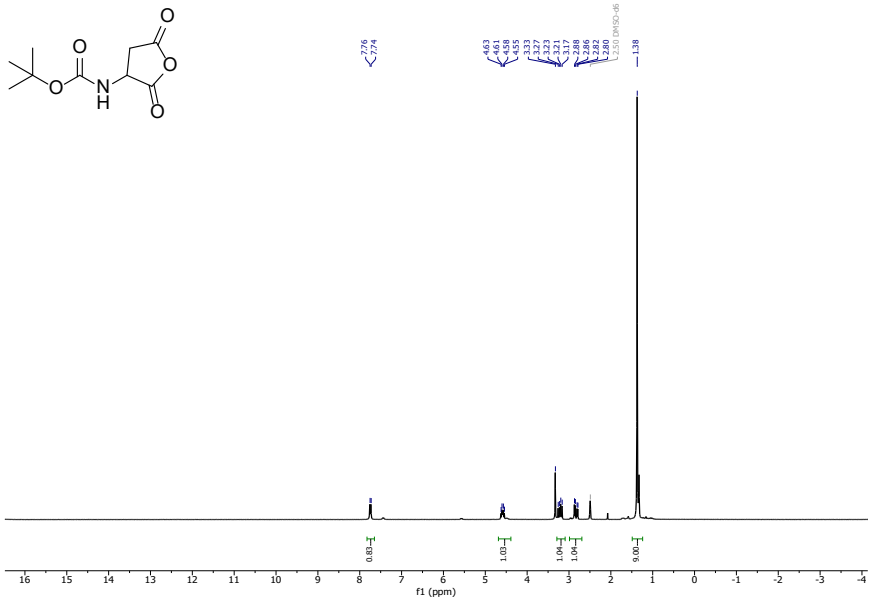

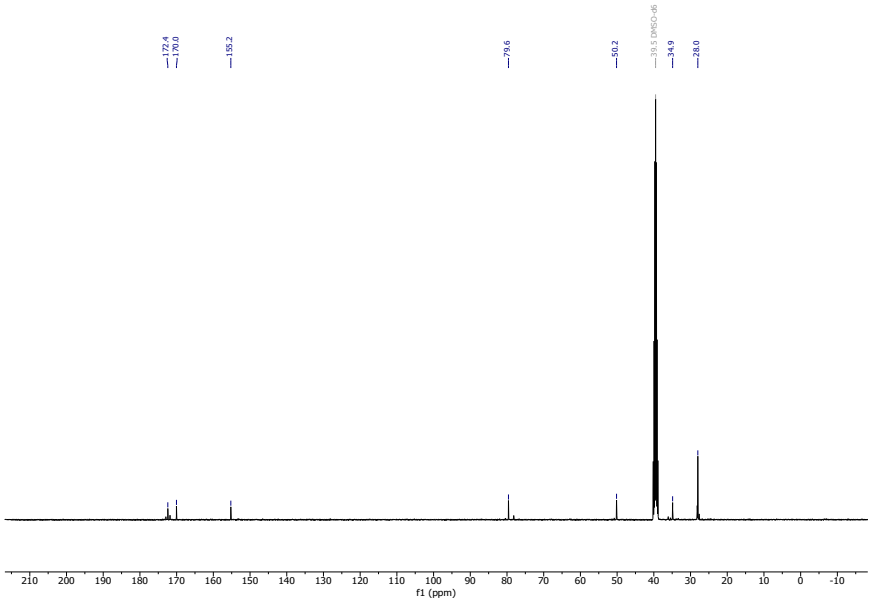

18

NMR-Spectra of (Z)-1-benzyl-2-(3-(dimethylamino)propyl)-3-ethylguanidine

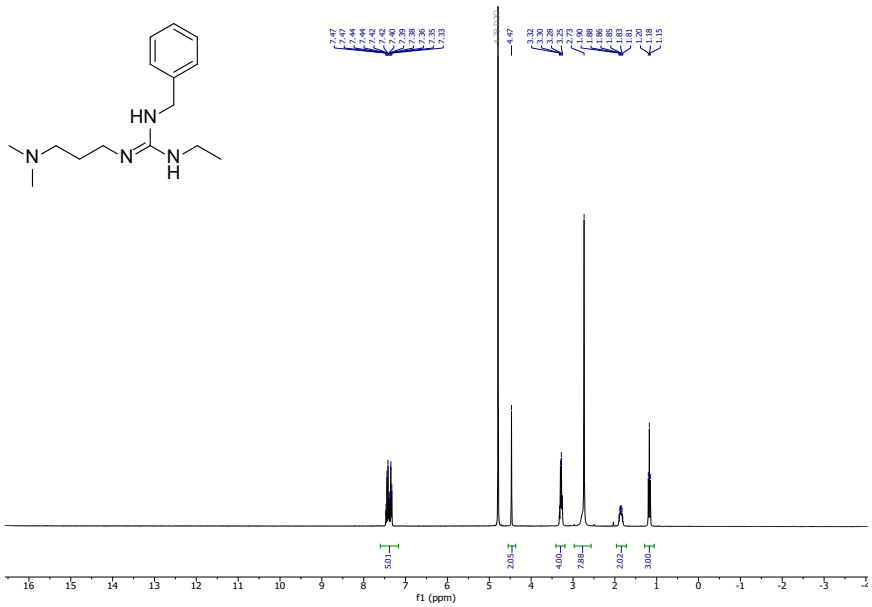

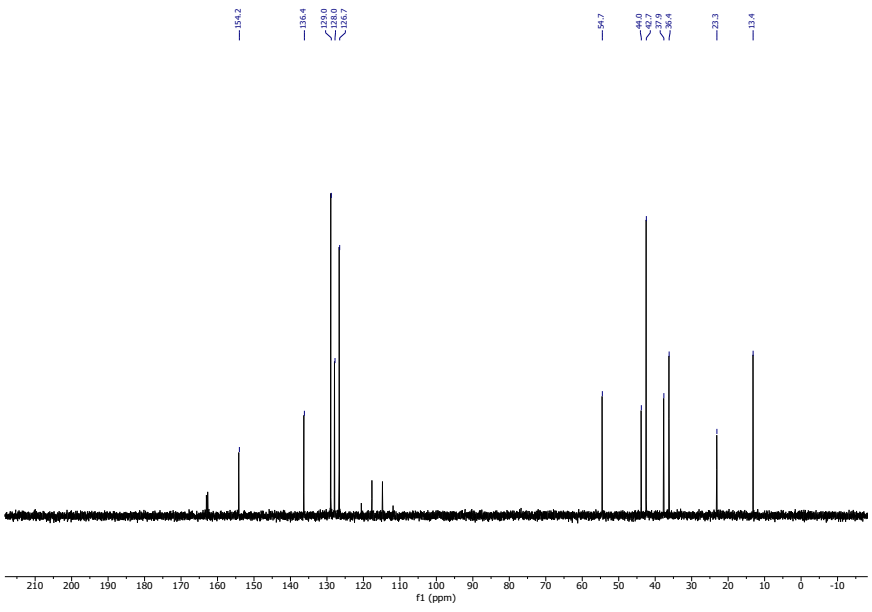

References

[1] M. Tena-Solsona, B. Riess, R. K. Grotsch, F. C. Lohrer, C. Wanzke, B. Kasdorf, A. R. Bausch, P. Müller-Buschbaum, O. Lieleg, J. Boekhoven, *Nat. Commun.* **2017**, *8*, 15895.

[2] T. Munegumi, Y. Q. Meng, K. Harada, *Asian J. Chem.* **2014**, *26*, 4716.

[3] B. Riess, C. Wanzke, M. Tena-Solsona, R. K. Grotsch, C. Maity, J. Boekhoven, *Soft Matter* **2018**, *14*, 4852.

6 Synthesis and characterization of molecular assemblies driven by carbodiimide-based fuels

Abstract.

In biology, supramolecular structures are maintained by a constant influx of energy. Compared to thermodynamically stable structures, dynamic structures possess unique properties such as tunable lifetimes, adaptivity or the ability to self-heal. To equip artificial materials with such properties, synthetic reaction cycles have been developed which drive the self-assembly of precursor molecules. So far, the carbodiimide-driven reaction cycle has been used by several groups to create various dynamic structures.[44,45,63–65] Amongst them are hydrogel fibers, colloids, oil-droplets or coacervates. The aim of this work was to establish a protocol to synthesize and characterize carbodiimide-based reaction cycles. It shows how to synthesize peptide-based precursor molecules such as the short peptide N-Fmoc-AAD-OH both manually and automatically. Furthermore, it explains how to analyze the kinetic response of the precursors to a carbodiimide-based chemical fuel by HPLC and kinetic models. The response of the reaction cycle to various amounts of fuel is described by characterizing the macro- and microscopic properties of the assemblies. The protocol aims to make it easier for research groups to get started working with the reaction cycle. Thus, each individual step in the process is listed. The scope of information is higher compared to the information generally provided in the methods section of research articles. As such, the work contains a section to trouble shoot common complications. Furthermore, a general protocol helps to validate, interpret, and compare the data within the community.

This work has been published:

Title:	Synthesis and characterization of chemically fueled supramolecular materials driven by carbodiimide-based fuels
Authors:	Fabian Schnitter, Alexander M. Bergmann, Benjamin Winkeljann, Jennifer Rodon Fores, Oliver Lieleg, Job Boekhoven
First published:	30. June 2021
Journal:	Nat Protoc 16, 3901-3932 (2021)
Publisher:	Nature Publishing Group
DOI:	10.1038/s41596-021-00563-9

Reprinted with permission of Nature Publishing Group.

This section states the individual work of each author in the publication below. F. Schnitter conducted the experiments regarding kinetic analysis and UV-vis analysis and wrote the kinetic model. A. M. Bergmann conducted the experiments regarding peptide synthesis, time-lapse photography, fluorescence and cryo-TEM microscopy. B. Winkeljann conducted the experiments regarding rheology. J. Boekhoven, F. Schnitter and A. M. Bergmann outlined and wrote the manuscript. J. Rodon Fores outlined and wrote the manual synthesis part. B. Winkeljann outlined and wrote the rheology part. The work was performed under the supervision and guidance of J. Boekhoven and O. Lieleg.

nature protocols

PROTOCOL

https://doi.org/10.1038/s41596-021-00563-9

Check for updates

Synthesis and characterization of chemically fueled supramolecular materials driven by carbodiimide-based fuels

Fabian Schnitter[1], Alexander M. Bergmann[1], Benjamin Winkeljann[2], Jennifer Rodon Fores[1], Oliver Lieleg[2] and Job Boekhoven[1,3]✉

Many supramolecular materials in biological systems are driven to a nonequilibrium state by the irreversible consumption of high-energy molecules such as ATP or GTP. As a result, they exhibit unique dynamic properties such as a tunable lifetime, adaptivity or the ability to self-heal. In contrast, synthetic counterparts that exist in or close to equilibrium are controlled by thermodynamic parameters and therefore lack these dynamic properties. To mimic biological materials more closely, synthetic self-assembling systems have been developed that are driven out of equilibrium by chemical reactions. This protocol describes the synthesis and characterization of such an assembly, which is driven by carbodiimide fuels. Depending on the amount of chemical fuel added to the material, its lifetime can be tuned. In the first step, the protocol details the synthesis and purification of the peptide-based precursors for the fuel-driven assemblies by solid-phase peptide synthesis. Then, we explain how to analyze the kinetic response of the precursors to a carbodiimide-based chemical fuel by HPLC and kinetic models. Finally, we detail how to study the emerging assembly's macro- and microscopic properties by time-lapse photography, UV-visible spectroscopy, shear rheology, confocal laser scanning microscopy and electron microscopy. The procedure is described using the example of a colloid-forming precursor Fmoc-E-OH and a fiber-forming precursor Fmoc-AAD-OH to emphasize the differences in characterization depending on the type of assembly. The characterization of a precursor's transient assembly can be done within 5 d. The synthesis and purification of a peptide precursor requires 2 d of work.

Introduction

Supramolecular materials consist of molecular building blocks assembled into larger architectures by noncovalent interactions[1,2]. In the past decades, the field has emerged and evolved into a discipline with design rules and a plethora of prominent examples[3], such as liquid crystals[4–6], supramolecular polymers[7–9], or vehicles that can deliver pharmaceuticals[10,11].

Supramolecular materials are also present in biological systems; skin and bone are both examples of materials constructed using molecular self-assembly[12–15]. A property of most natural supramolecular materials is that their building blocks are continuously recycled, which allows them to adapt to changing conditions or to repair themselves[16]. These properties are seldom seen in synthetic materials.

Synthetic supramolecular materials almost always exist in or close to equilibrium[17]. In contrast, living materials exist far out of equilibrium[18,19]. To sustain biological materials out of equilibrium, these materials are continually dissipating energy, which is harvested from chemical reaction cycles that irreversibly consume high-energy molecules such as GTP or ATP[20–22]. Owing to their constantly active nature, these materials are endowed with a higher degree of dynamics than synthetic (static) materials.

Inspired by this dynamic, energy-consuming form of self-assembly of molecules, the field of supramolecular materials has more recently focused on developing synthetic counterparts of biological supramolecular materials: so-called chemically fueled supramolecular materials[23–31]. In such supramolecular materials, the self-assembly of molecules is regulated by a chemical reaction cycle (Fig. 1a,b). The chemical reaction cycle irreversibly consumes a high-energy reagent, called a chemical fuel, and thereby dissipates energy. Thus, in these systems, the formation of assemblies away from

[1]Department of Chemistry, Technical University of Munich, Garching, Germany. [2]Department of Mechanical Engineering and Munich School of Bioengineering, Technical University of Munich, Garching, Germany. [3]Institute for Advanced Study, Technical University of Munich, Garching, Germany. ✉e-mail: job.boekhoven@tum.de

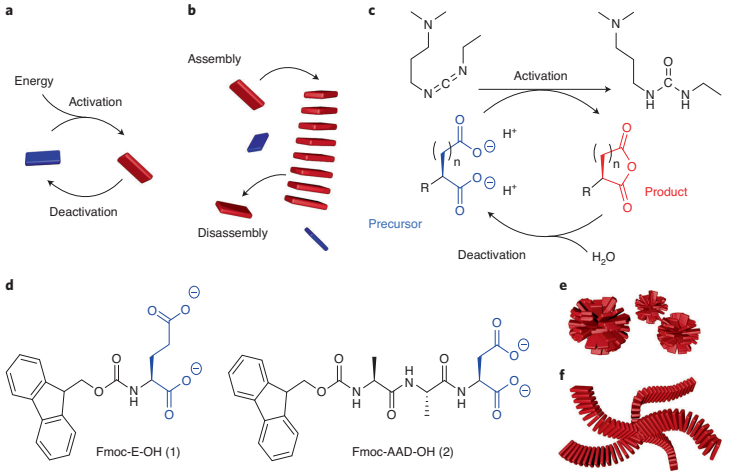

Fig. 1 | In chemically fueled self-assembly, molecules are activated and deactivated for assembly by a chemical reaction cycle. a, An energy-driven chemical reaction activates a precursor molecule for self-assembly. A spontaneous deactivation reaction reverts the activated product to the precursor state. **b**, The result is a transient product that, in its finite lifetime, can take part in a dynamic assembly. **c**, In the chemical reaction cycle, a dicarboxylate precursor molecule is converted into an asymmetric anhydride product. The hydration of EDC fuels the activation reaction and generates the waste byproduct EDU (1-ethyl-3-(3-dimethylaminopropyl)urea). The hydrolysis reaction reverts the formed anhydride to the original precursor. **d**, The molecular structures of precursors that are used in this work. **e**,**f**, The resulting supramolecular structures are schematically shown as colloids (**e**) and hydrogel fibers (**f**).

Table 1 | Different precursors and the corresponding types of assembly when fueled with EDC

Type of assembly	Precursor
Colloids	Fmoc-D-OH[39], Fmoc-E-OH[42], Fmoc-GD-OH[46]
Fibers	Fmoc-AAD-OH[39], Fmoc-AVD-OH[39], Fmoc-AAE-OH[39], Fmoc-AVE-OH[39], Ac-FIID-OH[41]
Aggregates of nanoparticles	5-hexenoic acid coated SiNCs[43], 3-mercaptopropionic acid coated AuNPs[44]
Coacervate-based droplets	Ac-FRGRGRGD-OH[47]
Oil droplets	2-octen-1-ylsuccinic acid[46], 2-decen-1-ylsuccinic acid[46], valeric acid[45], caproic acid[45]

equilibrium is driven by a kinetic asymmetry in the energy consumption pathway[32,33]. Examples are ubiquitous in biology (e.g., the GTP-fueled formation of microtubules), but only a few reactions have been tried synthetically. One approach is the use of biological fuel sources in chemical reaction cycles such as the phosphorylation and dephosphorylation with ATP or GTP[28,34]. These systems are conceptually close to biology, but the requirement of specialized enzymes limits the versatility of these systems compared with more artificial approaches. Simpler synthetic systems allow a more in-depth study of individual mechanisms in otherwise complex biological systems. Artificial approaches of fuel-driven assemblies include methylation[35], thiol–thioester exchange[36] or redox chemistry as the activation reaction[37,38]. Many of these systems require just one functional group and are more versatile compared with enzymatic reactions.

We recently introduced a carbodiimide-fueled reaction cycle that leads to dynamic assemblies[39,40]. In several studies, we showed how the chemical reaction cycle could drive the formation of different types of assemblies depending on the type of precursor used (Table 1). We showed the formation of fibers[39,41] colloids[42], aggregates of nanoparticles[43,44], oil droplets[45,46] and coacervate-based droplets[47].

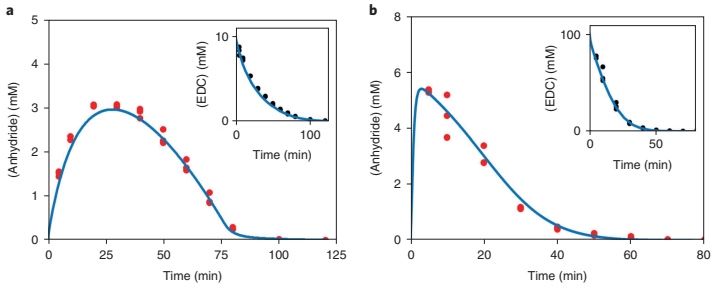

Fig. 2 | Kinetic analysis of the reaction cycle. a,**b**, The analysis was performed with precursor **1** in response to 10 mM EDC (**a**) and precursor **2** in response to 100 mM EDC (**b**). HPLC measures the concentration of anhydride and EDC (inset). The markers represent triplicate HPLC data, and the lines are predicted values from our kinetic model.

Due to the emerging material properties, a wide variety of different applications can be envisioned. For example, coacervate-based droplets serve as a model for membranelles organelles and protocells[47]. The out-of-equilibrium formation of oil droplets from a set of primitive carboxylic acids exhibits self-selective behavior[45]. Temporal control over aggregation of silicon nanocrystals shows potential as a platform for controlled uptake of nanoparticles into cells[43]. Fuel-driven fiber formation can serve as a model to study cytoskeleton structures such as microtubulin and actin filaments[48]. Moreover, other research groups are also starting to use this chemical reaction cycle[49,50].

Overview of the protocol

In this protocol, we use a chemical reaction cycle that transiently activates dicarboxylate precursors by converting them into their corresponding cyclic anhydrides at the expense of a carbodiimide-based condensing agent (Fig. 1c). In the activation reaction, the precursor reacts irreversibly with the 1-ethyl-3-(3-dimethylaminopropyl)carbodiimide (EDC or fuel) to yield its corresponding anhydride. In the deactivation reaction, the anhydride product reacts with water to yield the original precursor. Consequently, the precursor is activated into its temporary, anhydride state. The anhydride state is uncharged, whereas the precursor carries two anionic carboxylate groups. We use the loss of charges to induce self-assembly of the precursors (Fig. 1d). For example, if the precursor carries a relatively large hydrophobic group (e.g., Fmoc-E-OH (**1**)), it is soluble in its precursor state but assembles into colloids in the product state (vide infra)[39]. We found that, when we add amino acids with a high propensity to form β-sheets in the precursor design, it is more likely to form anisotropic assemblies in its activated state. For example, in this protocol, we will show that Fmoc-AAD-OH (**2**) will form fibers when fueled with EDC.

We start the protocol by describing the synthesis and purification of the precursors. Precursor **1** is commercially available and used without further purification. Precursor **2** was synthesized using solid-phase peptide synthesis, purified by preparative HPLC, and finally freeze-dried to yield a fluffy, white powder on a 100 mg scale. Both precursors are dissolved in 2-morpholinoethanesulfonic acid (MES)-buffered water. The pH of the resulting solution is adjusted to 6.0.

In the next section of the procedure, we describe how to study the kinetics of the reaction cycle for the two precursors in the EDC-driven chemical reaction cycle. The cycle is initiated by adding the chemical fuel EDC to the precursor solutions. At predetermined intervals, we quench a sample of the experiment by adding benzylamine. Benzylamine freezes the reaction cycle in its current state by converting the reactive anhydride into the respective stable amide. Moreover, the addition of the quenching solution stops the activation reaction owing to an increase of the pH to 10. At this pH, EDC does not react with the carboxylic acids, and therefore, no more anhydride is formed. The quenched samples are studied by reversed-phase analytical HPLC. Using a nonpolar hydrocarbon stationary phase allows separation of the reaction cycle's components and determining the concentration of precursor, product and fuel (Fig. 2a,b).

We then explain how to use a kinetic model, written in MATLAB, to predict both the concentration of the components in the mixture and the reaction rates. This model is especially powerful for predicting for how long the anhydride product is present when adding different amounts of EDC.

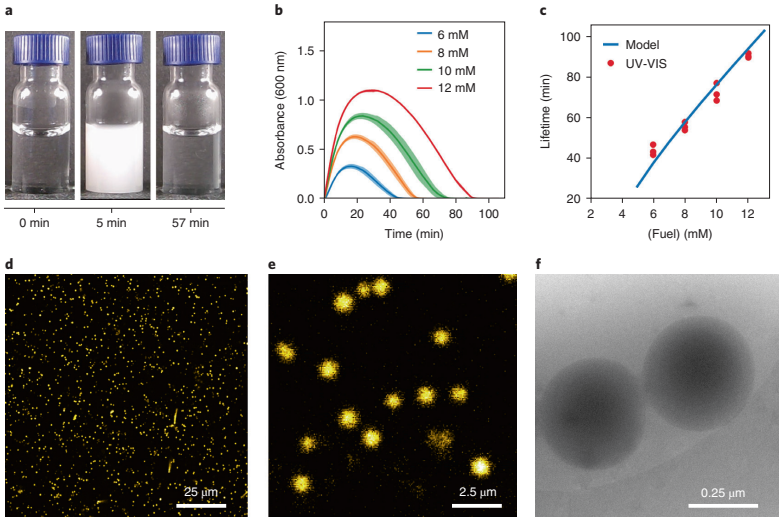

Fig. 3 | Material properties of 10 mM precursor 1 in response to fuel. a, Time-lapse photography shows the transient increase in turbidity in response to 10 mM EDC. **b**, The absorbance at 600 nm is a measure for turbidity of **1** in response to EDC's varying concentrations. The shaded area represents the deviation from triplicate data. **c**, The lifetime of the turbidity as a function of fuel added is determined from the data of **b** (markers) and the kinetic model (line). **d**,**e**, Fluorescence microscopy micrograph as recorded by confocal microscopy (**d**) and a magnification (**e**). **f**, Cryo-TEM microscopy micrograph.

In later experiments, the anhydride lifetime can be correlated to the material's lifetime. For example, we show that increasing the amount of fuel results in a longer presence of the anhydrides, which corresponds to a prolonged presence of the material properties.

The next stage of the procedure involves studying the dynamic material properties of the emerging dissipative supramolecular materials. We describe how to set up a webcam to record time-lapsed photographs of the fueled reaction cycle (Figs. 3a and 4a and Supplementary Video 1 and 2). This is a cheap way to get rapid, qualitative information about the evolution of material properties such as turbidity or the ability to form self-standing hydrogels. To better quantify the turbidity and the time course of its evolution, we use UV-visible (UV-VIS) spectroscopy and measure the optical density at 600 nm in a plate reader over time (Fig. 3b). If the reaction generates a hydrogel, we follow the time course using shear rheology (Fig. 4b). The quantitative information of the material properties' evolution can be correlated to the previously described kinetic model. We do so by determining a threshold concentration of the anhydride product. Above this threshold, the property of the materials (turbidity or the formation of an elastically dominated hydrogel) can be expected. We find that, for precursor **1**, the model can accurately predict the lifetime of the turbid solution, which we describe in the next section of the protocol (Fig. 3c). The correlation between the lifetime of the gels formed by **2** is also calculated (Fig. 4c).

In the final section of the procedure, we describe how to characterize the structure of the temporary assemblies by confocal microscopy using the hydrophobic dye Nile red (Figs. 3d,e and 4d,e) and by cryogenic transmission electron microscopy (cryo-TEM) (Figs. 3f and 4f).

Experimental design

In the following sections, we describe the peptide synthesis, the kinetic analysis of the reaction cycles and the observation of the emerging macro-, micro- and nanoscopic properties (Fig. 5).

Synthesis of precursors

Precursor **1** was commercially available and used without further purification. Precursor **2** was synthesized via solid-phase peptide synthesis (Fig. 6). Different methods for peptide synthesis have

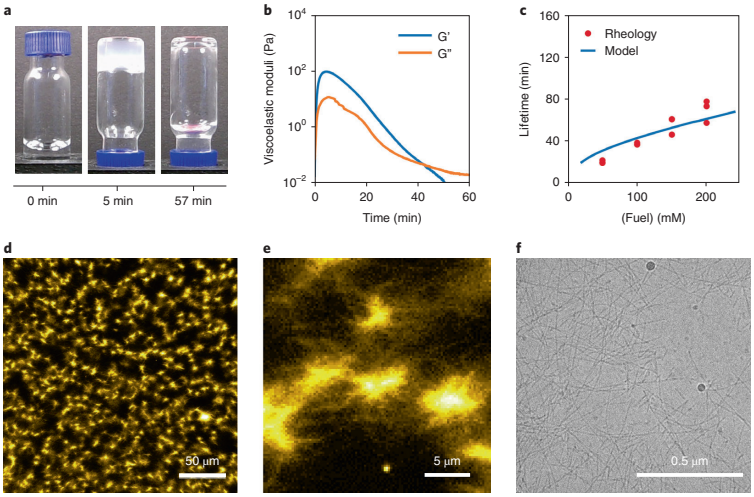

Fig. 4 | Material properties of precursor 2 in response to fuel. a, Time-lapse photography shows the formation of a transient hydrogel when fueling with 100 mM EDC. **b**, The viscoelastic response as represented by the storage (G′) and loss modulus (G″) of the hydrogel formed when adding 100 mM EDC as a function of time as measured by shear rheology. **c**, The lifetime of the hydrogel as a function of concentration fuel added. The lifetime is measured by rheology (markers) and predicted by the model (line). **d**,**e**, Fluorescence microscopy micrograph as recorded by confocal microscopy (**d**) and a magnification (**e**) to show the nucleation sites. **f**, Cryo-TEM shows the formation of a fiber network.

been described in previous protocols. These methods range from a general procedure to the synthesis of more complex sequences[51,52], and approaches for simultaneous synthesis of different peptide sequences[53]. In general, any Fmoc-based solid-phase peptide synthesis method is suitable for the synthesis of the peptide sequences listed in Table 1. A requirement is a free C-terminal carboxylic acid after cleavage from the resin. We thus used Wang resin, which was purchased preloaded with the first amino acid. The peptide was further reacted from the C to the N terminus by repeated deprotection and coupling steps. The resulting peptide is cleaved from the resin, the identified product peak is purified by preparative HPLC and the final product is characterized by analytical HPLC, electrospray ionization mass spectrometry (ESI-MS) and NMR. The synthesis can either be performed using a microwave-assisted automated peptide synthesizer or performed manually using a peptide synthesis vessel. The advantage of automated synthesis is that it takes only ~1 h to complete. However, the type of peptide synthesizer used limits the reaction scale (0.5 mmol, which is the equivalent of 122 mg Fmoc-AAD-OH (**2**) after purification). In contrast, the manual synthesis of **2** takes 5 h, but bigger scales can be obtained. Both techniques yield roughly equal amounts of the peptide product at a scale of 0.5 mmol. We recommend manual peptide synthesis if a peptide synthesizer is not available or when scales >0.5 mmol are synthesized.

Nile red assay

In carbodiimide driven self-assembly, the precursor's carboxylate groups react to form an anhydride group, which means that this section of the molecule becomes more hydrophobic. This transition often affects only a small domain of the overall precursor; therefore, the precursor itself needs to be quite hydrophobic for the modification to induce self-assembly. Thus, it is possible that the precursor might assemble without the addition of fuel, especially when the precursor is present at high concentrations. A fast method to test whether the precursor is unimolecularly dissolved is a Nile red assay. Nile red is a solvatochromic dye. Its solubility and quantum yield are low in polar solvents such as water, but are substantially higher in nonpolar environments. Additionally, the absorption and emission wavelength is blue-shifted in nonpolar environments[54,55]. When structures like micelles are present in an aqueous solution, Nile red accumulates in the hydrophobic microenvironment, resulting in a high fluorescence intensity that is blue-shifted. Both the enhancement and shift in

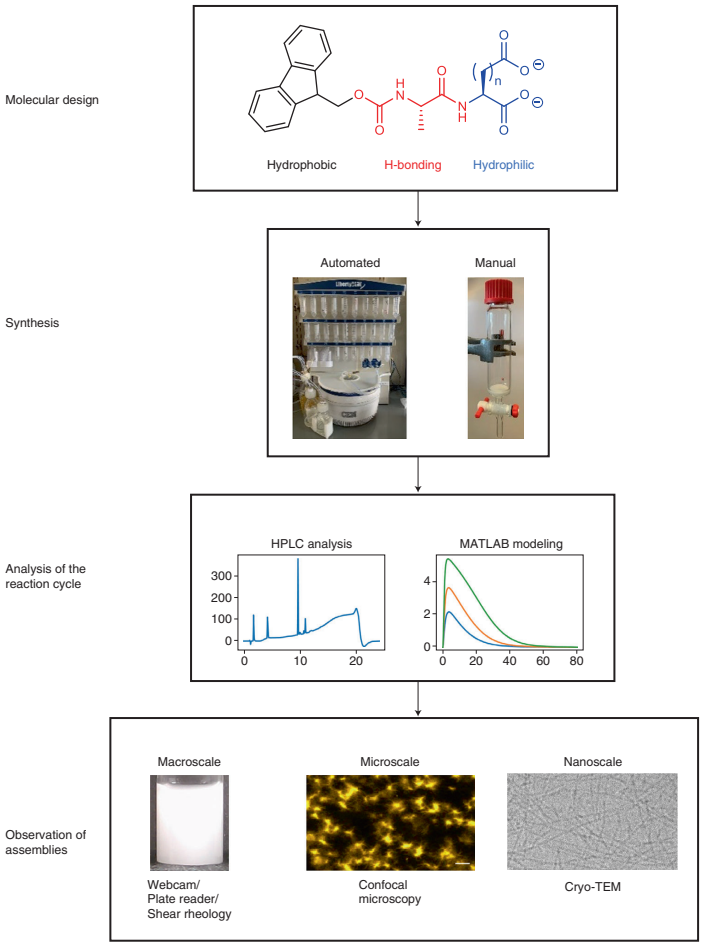

Fig. 5 | Overview of the experimental design. The precursor is designed by balancing attractive and repulsive interactions. While the charge repulsion of the inactivated precursor suppresses self-assembly, self-assembly occurs upon transformation into an anhydride. The peptide precursor is synthesized by applying manual or automated solid-phase peptide synthesis and purified by reversed-phase HPLC. Analytical HPLC measures the concentrations of fuel and product upon fuel addition. By fitting the experimental data to a computational model, the reaction cycle's rate constants are determined. Finally, the assemblies' lifetimes as well as their morphologies are analyzed on the macro-, micro- and nanoscopic scale.

fluorescence are used to identify the critical aggregation concentration. We measure the fluorescence intensity at 635 nm at an excitation wavelength of 550 nm for various concentrations of **1** and **2**. An increase in the fluorescence intensity indicates the presence of assemblies or aggregates in absence of the chemical fuel. As a final test to exclude preassembly, we record cryo-TEM micrographs of the applied reaction cycle's precursor stock solutions (Extended Data Fig. 1).

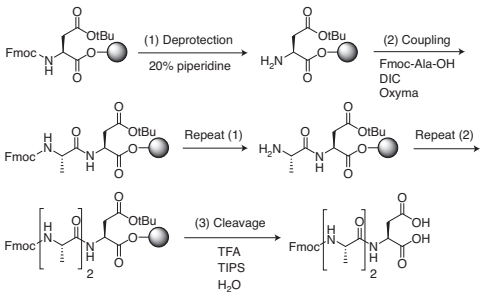

Fig. 6 | Reaction scheme of the proposed solid-phase peptide synthesis of 2. The solid support is Wang resin. Repeated Fmoc deprotection and coupling steps promote chain growth. The final product is obtained after cleavage from the resin and simultaneous removal of the protection groups.

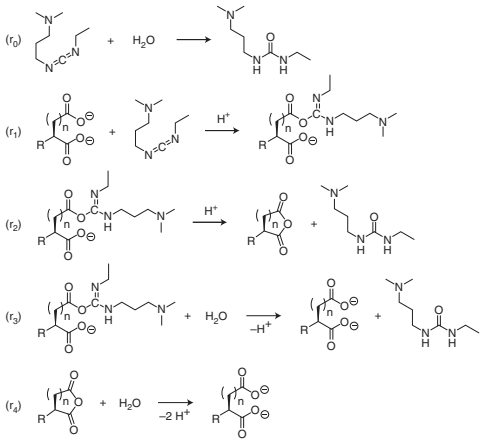

Fig. 7 | Reactions involved in the chemical reaction cycle. Reaction (r_0) shows the direct hydration of EDC in the reaction medium. The reaction (r_1) shows the activation as EDC is added to a carboxylate. The anhydride product formation is depicted by (r_2). A side reaction taking place is shown by (r_3), which is the activated precursor's direct hydrolysis. The deactivation reaction is described by (r_4) showing the anhydride hydrolysis reaction.

Analysis of kinetics by HPLC

The kinetics of the fuel-driven chemical reaction cycle for both precursors **1** and **2** are analyzed with analytical HPLC (Fig. 7). In these experiments, we measure the concentration of the carbodiimide-based fuel (EDC) and the anhydride product. The chemical reaction cycle is initiated by the addition of fuel to the precursor solution. At 7 min intervals, aliquots of the reaction mixture are added to a previously prepared benzylamine solution. The benzylamine solution quenches all reactions in the reaction cycle and converts the anhydride product into its corresponding amide[56]. The quenched samples are stored and analyzed after the reaction cycle is completed by injection into the HPLC. The signals in the chromatograms corresponding to the benzylamide and EDC are integrated. A calibration curve is measured for both components to determine their corresponding concentrations in the experiment.

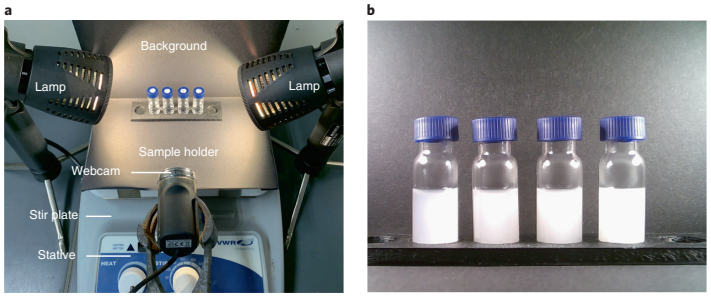

Fig. 8 | Time-lapse photography setup. a,**b**, The experimental setup of a webcam experiment (**a**) and the webcam view 5 min into the reaction cycle of Fmoc-E-OH (**1**) with 6, 8, 10 and 12 mM EDC from left to right (small differences in the turbidity for highly turbid solutions cannot be observed with this technique) (**b**).

Using a kinetic model in MATLAB

We use the data from the kinetic experiments to fit rate constants for a kinetic model. This kinetic model describes five chemical reactions to predict the concentration of the reactants involved at every second in the experiment (r_0, … r_4). The first reaction is the direct hydration of EDC (r_0). The second is the reaction of EDC with the precursor to yield O-acylisourea (r_1). The third reaction is the conversion of the O-acylisourea to the anhydride product (r_2). The other fate of the O-acylisourea is that it hydrolyzes to the precursor (r_3). Finally, the anhydride product hydrolyzes in the deactivation reaction (r_4). The rate constants of these reactions will be estimated by fitting the concentration profiles measured by HPLC. For example, k_0 can be estimated by fitting the EDC decay in the absence of precursor. Similarly, by fitting the EDC depletion curve in the presence of precursor, the rate constant for the reaction of the precursor with EDC (k_1) can be estimated.

Time-lapse photography

The materials we describe change their turbidity and viscoelastic properties during the reaction cycle; i.e., they transit from a solution to gel state and vice versa (Fig. 8). Changes in turbidity can be observed with the naked eye and can be monitored using a simple webcam setup without the need for laborious and time-consuming experiments. For example, for precursor **1**, a fuel-induced, temporary increase in turbidity was observed (Fig. 3a, Fig. 12). The time for which the increased turbidity is present gives an estimation about the lifetime of the assemblies and can be further investigated by UV-VIS analysis. Similarly, precursor **2** shows a temporary increase in turbidity in response to fuel. An inverted tube test is used as an indication for a temporary transition from a solution to a gel state (Fig. 4a). However, this transition needs to be further characterized by rheology measurements as the inverted tube test can give false-positive results[57].

UV-VIS analysis to measure the evolution of the turbidity

For more accurate kinetic information, the evolution of the turbidity as a function of time can be recorded with a UV-VIS instrument or plate reader. We measure the absorbance at 600 nm as a measure for turbidity as the evolving particles scatter light. This experiment can be done using a plate reader or using cuvettes; the plate reader experiment allows multiple experiments to be performed simultaneously. For example, we can measure the evolution of five different initial concentrations of fuel in triplicate in a single experiment. We use these acquired data to determine the lifetime of the assemblies of precursor **1** in response to varying amounts of fuel. Comparison of the measured lifetimes with anhydride concentrations at these time points provides mechanistic information about the dissipative system such as solubility or kinetic trapping.

Rheology measurements

The viscoelastic properties of a gel can be determined in a quantitative manner using macrorheology. The material response σ^* to an induced oscillating deformation γ^* is mapped to describe such viscoelastic materials. The corresponding modulus $G^*(\omega)$ is a complex parameter and can be

separated into a real and an imaginary part. The real part $G'(\omega)$ describes the elastic response of a material, whereas the imaginary part $G''(\omega)$ describes its viscous properties:

$$G'(\omega) = \frac{\sigma_0}{\gamma_0}\cos(\delta)$$
$$G''(\omega) = \frac{\sigma_0}{\gamma_0}\sin(\delta)$$

Here, σ_0 and γ_0 denote the amplitude of the shear stress and the shear strain, respectively. The phase shift between the deformation of the material and its stress response is denoted with δ, dependent on the angular frequency ω of the stimulation. Dominance of the storage modulus ($G' > G''$) indicates the formation of a gel, whereas a dominance in the loss modulus ($G'' > G'$) indicates a liquid-like behavior of the material.

In addition to time-lapse imaging and turbidity measurements, which together can provide a time-resolved visualization of the gelling process, macrorheology can offer a quantitative assessment of the gel formation process, not only over time but also determining absolute mechanical values.

Analysis by confocal laser scanning fluorescence microscopy

Confocal laser scanning fluorescence microscopy is used to examine the dissipative supramolecular materials' evolution on the microscopic scale. As the self-assembling building blocks are not fluorescently labeled, a fluorescent dye incorporated into the assemblies is used. We use the hydrophobic dye Nile red as it is sufficiently hydrophobic to incorporate into our assemblies. Moreover, due to its solvatochromic shift and increased quantum yields between hydrophilic and hydrophobic environments, it is possible to selectively observe the assembled product resulting in a high signal-to-noise ratio in the micrographs[58]. The sample is placed in a grease chamber on a glass microscope slide. The grease chamber offers an efficient method to prevent evaporation and flow of the sample throughout the experiments. In our experiments, confocal microscopy shows the formation of colloids for Fmoc-E-OH (**1**) (Fig. 3d,e) and the formation of entangled fibers for Fmoc-AAD-OH (**2**) (Fig. 4d,e).

Analysis by cryo-TEM

In our laboratoy, we use cryo-TEM to study the assemblies on the nanometer scale, e.g., to determine the diameter of fibers. We prefer cryo-TEM to conventional TEM, because the cryofixation process prevents ice crystal formation and, therefore, preserves all structures in their native aqueous state. Immediate cryogenic freezing at specific times during the reaction cycle further ensures temporal integrity of the assemblies. For precursor **1** with fuel, colloids with a mean diameter of 300–400 nm were found (Fig. 3f), whereas precursor **2** showed the presence of long and entangled fibers with a uniform diameter of ~6 nm in response to fuel (Fig. 4f).

Limitations

This protocol is written for carboxylate precursor molecules, forming assemblies that include colloids and hydrogel-fiber networks. In our experience with chemically fueled assemblies, we found that the emerging materials' dynamic properties are highly dependent on the amino acid sequence of the precursor. For example, this protocol describes the formation of transient hydrogels formed by Fmoc-AAD-OH (**2**). We found that changing the amino acid sequence to Fmoc-AVD-OH resulted in solutions that would convert into a hydrogel upon fuel application. However, these hydrogels would remain kinetically trapped and would not revert to their initial solutions state[39].

We have also found that the reaction cycle is highly pH-dependent. The EDC activation reaction is most active at acidic pH[59], but the closer the pH is to the pK_a of the carboxylic acids, the higher is the degree of protonation. Upon protonation of the carboxylic acids, self-assembly of the precursor can be induced without the need of anhydride formation. In contrast, increasing the pH from 6.0 to 7.0 would be sufficient to decrease the yield of anhydride sufficiently that no hydrogel is formed for Fmoc-AAD-OH (**2**)[39].

Finally, the design of our experimental protocol aims at anhydride-based assemblies. Minor parts such as the quenching method or the kinetic model are tailored to this specific system. The major part, however, focuses on the study of the dynamic material's properties. These techniques are independent of a specific chemical functionality. As a result, e.g., the described webcam setup can be applied to other reported forms of out-of-equilibrium systems to screen initial conditions. In general, the protocol instructions can be adapted to dynamic materials that possess the required physical properties of the applied technique. Limitations like the ability to scatter light or the incorporation of a hydrophobic dye are mentioned in the procedures part of this protocol.

Materials

Reagents

! CAUTION Chemical reagents are potentially harmful. Apply the appropriate safety procedures. Wear gloves, a laboratory coat and safety glasses. Take care to appropriately dispose of all chemicals used.

- MES hydrate, 99.5% (Sigma-Aldrich, cat. no. M8250)
- NaOH (Sigma-Aldrich, cat. no. S5881-1KG) **! CAUTION** Sodium hydroxide is highly corrosive and can cause severe skin and eye damage. Wear the appropriate protective equipment when handling this reagent.
- HCl (Sigma-Aldrich, cat. no. 320331-500ML) **! CAUTION** Hydrogen chloride is highly corrosive and can cause severe skin and eye damage. Inhalation might lead to respiratory damage. Wear the appropriate protective equipment, and use a fume hood when handling this reagent.
- Fmoc-E-OH (Alfa Aesar, cat. no. H62936)
- EDC (Sigma-Aldrich, cat. no. 03450-5G) **! CAUTION** *N*-(3-dimethylaminopropyl)-*N*′-ethylcarbodiimide hydrochloride has acute oral (category 4) and skin (category 3) toxicity and can cause severe skin and eye damage. Wear the appropriate protective equipment, and use a fume hood when handling this reagent.
- Benzylamine (Sigma-Aldrich, cat. no. 77869-25ML) **! CAUTION** Benzylamine has acute oral (category 4) and skin (category 4) toxicity and can cause severe skin damage. Wear the appropriate protective equipment, and use a fume hood when handling this reagent.
- Acetonitrile, HPLC grade (Sigma-Aldrich, cat. no. 34851-2.5L) **! CAUTION** Acetonitrile is highly flammable, has respiratory (category 4), skin (category 4) and oral (category 4) toxicity and can cause severe eye irritation. Wear the appropriate protective equipment, and use a fume hood when handling this reagent.
- Dimethylformamide (DMF), for peptide synthesis (Sigma-Aldrich, cat. no. 1003972500) **! CAUTION** DMF is flammable and has reproductive (category 1), respiratory (category 4) and skin (category 4) toxicity. Wear the appropriate protective equipment, and use a fume hood when handling this reagent.
- Diisopropylcarbodiimide (DIC; Sigma-Aldrich, cat. no. D125407-25G) **! CAUTION** DIC has acute respiratory (category 2) toxicity and can cause severe eye damage. Wear the appropriate protective equipment, and use a fume hood when handling this reagent.
- Piperidine (Sigma-Aldrich, cat. no. 104094-100ML) **! CAUTION** Piperidine has acute oral (category 4), skin (category 3) and respiratory (category 3) toxicity and can cause severe skin and eye damage. Wear the appropriate protective equipment, and use a fume hood when handling this reagent.
- Oxyma Pure (Sigma-Aldrich, cat. no. 8510860100)
- Fmoc-L-Ala-OH (Sigma-Aldrich, cat. no. 531480-100G)
- Fmoc-L-Asp(OtBu)-Wang resin, loading 0.6–1.0 mmol/g, 100–200 mesh (Iris Biotech, cat. no. WAA11305.0005)
- 4-Dimethylaminopyridine, ReagentPlus (Sigma-Aldrich, cat. no. 107700-25G) **! CAUTION** 4-Dimethylaminopyridine has acute oral (category 2) and skin (category 3) toxicity and can cause skin and eye damage. Wear the appropriate protective equipment, and use a fume hood when handling this reagent.
- Dichloromethane (DCM), HPLC grade (Sigma-Aldrich, cat. no. 34856-1L) **! CAUTION** DCM can cause skin and eye damage and is suspected to be carcinogenic. Wear the appropriate protective equipment, and use a fume hood when handling this reagent.
- Triisopropylsilane (TIPS; Sigma-Aldrich, cat. no. 233781-50G) **! CAUTION** TIPS is flammable.
- Diethyl ether, anhydrous (Sigma-Aldrich, cat. no. 346136-1L) **! CAUTION** Diethyl ether has acute oral (category 4) toxicity and is highly flammable. Wear the appropriate protective equipment, and use a fume hood when handling this reagent.
- Trifluoroacetic acid (TFA, Sigma-Aldrich, cat. no. T6508-500ML) **! CAUTION** TFA has respiratory (category 4) toxicity. It is highly corrosive (category 1) and can cause severe skin and eye damage. It is hazardous to aquatic environments, with long-lasting effects. Wear the appropriate protective equipment, and use a fume hood when handling this reagent.
- Dry ice **! CAUTION** Dry ice is a deep-cold solid and can cause cold burns. Wear cryogenic gloves, and work in a ventilated room. Wear the appropriate protective equipment, and use a fume hood when handling this reagent.
- Liquid nitrogen **! CAUTION** Liquid nitrogen is a deep-cold liquid and can cause cold burns. Wear cryogenic gloves, and work in a ventilated room. Wear the appropriate protective equipment, and work in a fume hood.

- Liquid ethane **! CAUTION** Liquid ethane is a deep-cold liquid and can cause cold burns. Wear cryogenic gloves, and work in a ventilated room. Ethane is highly flammable. Wear appropriate protective equipment, and work in a fume hood.
- Potassium cyanide (KCN), BioUltra (Sigma-Aldrich, cat. no. 60178-25G) **! CAUTION** KCN has acute oral (category 2), skin (category 1) and respiratory (category 2) toxicity. It is hazardous to aquatic environments, with long-lasting effects. Wear appropriate protective equipment, and work in a fume hood. Do not dispose in acidic aqueous waste to prevent the formation of volatile hydrogen cyanide.
- Pyridine, anhydrous (Sigma-Aldrich, cat. no. 270970-100ML) **! CAUTION** Pyridine has acute oral (category 4), skin (category 4) and respiratory (category 4) toxicity. It is flammable and can cause eye damage. Wear appropriate protective equipment, and work in a fume hood.
- Ninhydrin, ACS grade (Sigma-Aldrich, cat. no. 151173-25G) **! CAUTION** Ninhydrine has acute oral (category 4) toxicity and can cause skin and eye irritations. Wear appropriate protective equipment, and work in a fume hood.
- N-butanol (Sigma-Aldrich, cat. no. B7906-500ML) **! CAUTION** N-butanol is flammable. It has acute oral toxicity (category 4) and can cause skin and severe eye damage. Wear appropriate protective equipment, and work in a fume hood.
- Phenol (Sigma-Aldrich, cat. no. P1037-100G) **! CAUTION** Phenol has acute oral (category 3), skin (category 3) and respiratory (category 3) toxicity. It can cause severe skin and eye damage. It shows germ cell mutagenicity, and it is hazardous to aquatic environments, with long-lasting effects. Wear appropriate protective equipment, and work in a fume hood.

Equipment

General equipment

- High-resolution balance (with a minimum resolution of 0.1 mg, VWR, cat. no. 611-2265)
- Glass bottles (250 ml, Schott, cat. no. 21 801 365)
- Magnetic stir bar and magnetic stirrer (VWR, cat. no. 444-0614)
- Volumetric flasks (250 ml, 50 ml, 5 ml, 2 ml, 1 ml, VWR)
- Conical centrifuge tube (50 ml, 15 ml, Carl Roth, cat. no. N462.1)
- Microcentrifuge tube (1.7 ml, Carl Roth, cat. no. 4182.1)
- Funnel (VWR, cat. no. 221-0175)
- Single-channel pipettes (1 ml to 0.5 µl) and corresponding tips and wide bore tips (Eppendorf Research plus, cat. no. 3120000046)
- Glass HPLC vials (1.7 ml, Carl Roth, cat. no. XC64.1)
- Countdown timer (VWR, cat. no. 609-0226)
- Round-bottom flask (100 ml, VWR, cat. no. 201-1326)
- Glass sample vials with snap caps (5 ml, VWR, cat. no. MANA70271)
- Vortex mixer (IKA Vortex 2 8000, VWR, IKAA25000258)
- Liquid nitrogen dewar (VWR, cat. no. 478-4411)
- High-precision tweezers for microscopy (VWR, cat. no. 232-0143)

Peptide synthesis

- 50 ml peptide synthesis vessel for solid-phase peptide synthesis with a medium frit porosity (FengTecEx, cat. no. P120050M)
- Freezer (−30 °C)
- Flask shaker. For this study, we used the Stuart SF1 Flask Shaker (Sigma-Aldrich, cat. no. Z675245-1EA)
- Pressured nitrogen or air

Automated peptide synthesis

- For the automated synthesis, a microwave-assisted automated peptide synthesizer with a reaction vessel suitable for 20 ml batches is needed. For this study, we used a CEM Liberty Blue automated peptide synthesizer equipped with a Discovery Bio microwave module

Peptide purification

- Rotary evaporator. We used the Hei-VAP Core (VWR, 531-1111)
- Preparative HPLC setup capable of detecting and separating peptides. For this study, we used an Ultimate 3000 (Dionex/Thermo Fisher Scientific, cat. no. IQLAAAGABHFAPBMBFB) HPLC system with a Hypersil Gold, reversed-phase C_{18} column (particle size: 5 µm, length: 250 mm, ID: 20 mm;

Thermo Fisher Scientific, cat. no. 25005-259270A) and an automated fraction collector (Thermo Fisher Scientific, cat. no. VF-F11-A-01)
- ESI-MS setup to detect peptides with an *m*/*z* value of 500. For this study, we used an LCQ Fleet Ion Trap Mass Spectrometer (Thermo Fisher Scientific) with an electrospray ionization source
- NMR setup to measure ^{1}H-NMR at 400 MHz. For this study, we used a Bruker AVNeo 400. Chemical shifts are reported as δ-values in ppm relative to the deuterated solvent peak: $(CD_3)_2SO$ (δH: 2.05). MestReNova is used to analyze the spectra
- Lyophilizer to dry the peptides. The lyophilizer should hold 50 ml conical centrifuge tubes. In this study, we used a Christ Freeze Dryer Alpha 2-4 LDplus (VWR, cat. no. 535-3157)

Nile red assay
- Fluorescence spectrometer. We used a Jasco (Jasco FP-8300) spectrofluorometer with external temperature control (Jasco MCB-100)
- Quartz cuvette (10 mm path length, Hellma, cat. no. HL100-10-40)

Kinetic measurements
- An analytical HPLC setup is used for separation and detection of the various compounds in the reaction cycle. The setup also determines the purity of the synthesized peptides. For this study, we used a Vanquish Duo (Thermo Fisher Scientific, cat. no. VF-S02-A-02) HPLC system with a Hypersil Gold, reversed-phase C_{18} column (particle size: 3 µm, length: 100 mm, ID: 2.1 mm, Thermo Fisher Scientific, cat. no. 25003-102130)

Webcam-based experiments
- Webcam with manual focus connected to a computer. For this study, we used a full HD 1080p 12.0 megapixel webcam. To record the time-lapse series, we used the software Webcam Time-lapse from TNL Enterprises
- Magnetic stirrer and lifting ramp (VWR, cat. no. 444-0614)
- Retort stand with a clamp to hold the camera
- USB-powered LED lights
- Carton box to adjust light conditions
- Double-sided sticky tape
- Paper/cardboard

UV-VIS measurements
- Quartz cuvette (1 mm path length, Hellma, cat. no. HL100-1-40)
- UV-VIS spectrophotometer to perform turbidity measurements. For this study, we used Multiskan Go Microplate Spectrophotometer (Thermo Fisher Scientific)

Rheology based experiments
- Research-grade macrorheometer with torque resolution in the sub-micro-Newton range, an appropriate detection limit of the angular deflection and a temperature control unit. Here we used an MCR302 (Anton Paar, Graz, Austria). P-PTD200/Air (Anton Paar, Graz, Austria) and PP25 (Anton Paar, Graz, Austria) were used as bottom plate and measuring head, respectively
- Plate/plate measuring setup with a minimum diameter of the measuring head of 25 mm
- Humidity trap

Confocal microscopy
- Confocal microscope capable of exciting and detecting Nile red stained samples. For this study, we used a Leica TCS SP8 Lightning Confocal Microscope equipped with a 552 nm continuous wave laser (solid-state laser 20 mW), an HC PL APO CS2 63× water immersion objective, and a hybrid detector (HyD).
- High-vacuum silicon grease (Carl Roth, cat. no. 0855.1)
- 5 ml disposable syringe (Carl Roth, cat. no. 0057.1)
- Glass microscope coverslips (thickness 1, 24 × 60 mm, Carl Roth, cat. no. H878.2)
- Glass microscope coverslips (thickness 1, ∅ 12 mm, Carl Roth, cat. no. P231.1)

Cryo-TEM microscopy

- Transmission electron microscope suitable for cryogenic samples. For this study, we used a Tecnai spirit, FEI/Thermo Fisher Scientific
- C-Flat 2/2 Cryo-EM Grid–Copper (400 grid mesh, 20 nm carbon thickness, ScienceServices, cat. no. ECFT-224C-50)
- Cryo-TEM grid box
- Paraffin film (VWR, cat. no. 291-0057)
- Microscope slide (thickness 1 mm, 76 × 26 mm, Carl Roth, cat. no. H869.1)
- EMS Glow discharger K100X
- A controlled environment vitrification system to prepare cryogenic samples for TEM. In this study, we used an FEI Vitrobot Mark IV (Thermo Fisher Scientific)
- Cryo-transfer-specimen holder (Gatan)

Software

- The processing of the recorded data from both confocal and cryo-TEM microscopy was done using ImageJ in combination with the Fiji distribution

Reagent setup

Preparation of reagents and stock solutions

For the preparation of the stock solutions, deionized water was used. We obtained the water from a Millipore Milli-Q laboratory water system.

200 mM MES pH 6.0

For the preparation of 250 ml MES buffer at 200 mM, dissolve 9.76 g MES hydrate in ~200 ml of water in a glass bottle equipped with a stir bar. After dissolution, transfer the bottle to a calibrated pH meter, and adjust the pH to 6.0 by titration with NaOH and HCl stock solutions. Pour the buffer solution into a 250 ml volumetric flask, and fill it up to the water calibration line. The pH should not have been changed by dilution, but it is worth a second control with the pH meter. The resulting buffer can be stored for weeks, but the pH should be checked occasionally. When a color change is observed, the buffer should be renewed. ▲ **CRITICAL** Take care of the temperature dependency of the pH, and use the temperature sensor while adjusting.

10 mM precursor stock solution of Fmoc-E-OH (1) for HPLC calibration

For the HPLC calibration of precursor **1**, we prepare a 1 ml solution in 200 mM MES with 10 mM of precursor **1**. Therefore, 3.7 mg of **1** is weighed in a 1 ml volumetric flask, and 200 mM MES pH 6.0 is added to the calibration line. There is no need to adjust the pH. ▲ **CRITICAL** Use buffered water instead of pure water to increase the solubility of **1**.

10 mM precursor stock solutions of Fmoc-E-OH (1) and Fmoc-AAD-OH (2) for kinetic analyses

The preparation of 5 ml stock solutions is sufficient to conduct the experiments described below. Weigh in 18.5 mg of precursor **1** in a 15 ml conical centrifuge tube. Similarly, 24.9 mg of **2** is weighed in a 15 ml conical centrifuge tube. Dissolve the solid in slightly less than 5 ml 200 mM MES pH 6.0. Then, transfer the solutions to a pH meter, and adjust the pH to 6.0 by titration with NaOH and HCl stock solutions. After pouring the solution into a 5 ml volumetric flask, add 200 mM MES pH 6 buffer solution up to the calibration line. The precursor stock solutions can be stored in conical centrifuge tubes for weeks in a refrigerator. ▲ **CRITICAL** The peptide synthesis typically yields low amounts of product. When doing kinetic experiments, the results can change for varying synthesis batches due to differing impurities. Therefore, better repeat the synthesis and combine the batches for the precursor stock solution preparation.

2.0 M EDC stock solution

We prepare 100 µL of a 2.0 M EDC stock solution by weighing in 38.3 mg of EDC in a 1.7 ml microcentrifuge tube. The solid is dissolved by adding 61.4 mg of water to yield a final volume of 100 µL. The water is added to the microcentrifuge tube and should be equal to the mass of 100 µL water, which is 99.7 mg. ▲ **CRITICAL** EDC reacts with water, albeit slowly. The EDC solutions should be prepared fresh right before the experiment.

22 mM benzylamine stock solution in acetonitrile/H_2O (6%/94%)
A 22 mM benzylamine stock is prepared by weighing in 117.9 mg in a 50 ml volumetric flask. Dissolve the benzylamine by adding 3 ml acetonitrile. Finally, add water to a final volume of 50 ml. The stock solution can be stored in conical centrifuge tubes in the refrigerator for ~1 week. ▲ **CRITICAL** Benzylamine reacts with air carbon dioxide, forming carbamic acid (white crusts around the bottleneck).

2.5 mM Nile red stock solution
A 2.5 mM Nile red stock solution is prepared by weighing in 7.96 mg of Nile red and subsequent dissolution in 10 ml of methanol. The stock solution can be stored for several weeks in a refrigerator when adequately sealed with parafilm.

Procedure

Synthesis of precursor Fmoc-AAD-OH (2)

1 The following describes the 0.5 mmol scale synthesis of **2** using (A) an automated peptide synthesizer or (B) manually using a peptide synthesis vessel. The yield and purity are equivalent.

(A) **Automated solid-phase peptide synthesis**

(i) **Preparation of amino acid solutions** (steps i–iii; Timing 1 h) In separate 50 ml centrifugal tubes, weigh in Fmoc-Ala-OH, Oxyma, DIC and piperidine. Afterwards, add DMF to dissolve the reagents. Find the required amounts for a 0.5 mmol batch of Fmoc-AAD-OH (**1**) in the table below.

▲ **CRITICAL STEP** For calculation, a dead volume in the peptide synthesizer tubing of 4 ml has been considered. When too little reagent solution is used, it may cause an error during the automated peptide synthesis.

! **CAUTION** DIC is flammable and highly toxic. Wear gloves and protective gear, and use a fume hood while working with DIC.

! **CAUTION** DMF is flammable and has suspected reproductive toxicity. Wear gloves and protective gear and use a fume hood while working DMF.

! **CAUTION** Piperidine has acute oral, skin and respiratory toxicity and can cause skin and eye damage. Wear appropriate protective equipment, and use a fume hood.

Compound	Concentration	Total volume	Amount
Fmoc-Ala-OH	0.20 M	44 ml	2.7 g
Oxyma	1.0 M	15 ml	2.1 g
DIC	0.50 M	20 ml	1.6 ml
Piperidine	20 vol%	60 ml	12 ml

(ii) For the solid support, weigh Fmoc-Asp(OtBu)-Wang resin (773 mg, 0.68 mmol/g, 1 eq.) in a 15 ml centrifugal tube to yield a total loading of 0.5 mmol.

▲ **CRITICAL STEP** Make sure to use resins with a mesh size recommended for the used peptide synthesizer. Using the wrong mesh size can damage the machine.

(iii) Add 10 ml of DMF to the resin, vortex it and allow it to swell for 10 min.

■ **PAUSE POINT** The prepared stock solutions can be stored for up to 1 week at room temperature (RT, 25 °C).

(iv) **Automated peptide coupling** (iv–vi, Timing 1 h) Mount the prepared stock solutions on the Liberty Blue peptide synthesizer at their respective positions, and add the resin to the reaction vessel.

(v) Empty the waste container, fill up the DMF solvent container and open the supply line for the peptide synthesizer's inert gas.

(vi) Switch on the peptide synthesizer, and start the synthesis protocol for Fmoc-AAD-OH (**2**). The coupling protocol we are using includes double deprotection and double coupling for each addition of amino acid. We list the procedures for deprotection, coupling and washing performed by the peptide synthesizer in the table below.

Step	Procedure	Action
1	Deprotection	(1) Add 10 ml piperidine (20% in DMF) (2) Run microwave at 205 W for 30 s (max temp. of 80 °C) (3) Run microwave at 50 W for 65 s (max temp. of 90 °C) (4) Drain reaction vessel
2	Wash	(1) Add 5 ml solvent (2) Drain reaction vessel
3	Deprotection	
4	Wash (3×)	
5	Coupling	(1) Add 10 ml of the amino acid (2) Add 4 ml DIC (3) Add 2 ml Oxyma (4) Run microwave at 220 W for 35 s (max temp. of 85 °C) (5) Run microwave at 50 W for 120 s (max temp. of 90 °C) (6) Drain reaction vessel
6	Wash	
7	Coupling	
8	Wash (2×)	

? TROUBLESHOOTING

(vii) **Workup** (vii–viii, Timing 30 min) After finishing all the steps, add 5 ml DMF to the reaction vessel. Carefully shake the reaction vessel to suspend the resin, and pour the DMF together with the resin in a peptide vessel. Repeat this step two times.

(viii) Filter off the DMF, and wash the resin three times with DCM. Use pressured air to speed up the filtration and to dry the resin.

! CAUTION DCM is flammable and suspected to be carcinogenic. Wear gloves and protective gear, and use a fume hood while working with DCM.

■ PAUSE POINT The resin can be stored for up to 1 month in the freezer at −20 °C.

(B) **Manual solid-phase peptide synthesis**

▲ CRITICAL The peptide synthesis (from step v) is explained for Fmoc-AAD-OH (**2**) but can be performed in a similar way for other sequences.

(i) **Preparation of stock solutions for the Kaiser test** (steps i–iii, Timing 30 min) Dissolve 16.5 mg KCN in 25 ml water. Dilute 1 ml of this aqueous KCN solution with 49 ml of pyridine.

! CAUTION KCN is highly toxic. Wear gloves and protective gear, and use a fume hood while working with KCN. Highly toxic hydrogen cyanide forms when acidifying the solution.

! CAUTION Pyridine is flammable and toxic. Wear gloves and protective gear, and use a fume hood while working with pyridine.

(ii) Dissolve 1 g of ninhydrin in 20 ml of n-butanol.

! CAUTION Ninhydrin is toxic and can cause skin and eye irritations. Wear appropriate protective equipment, and use a fume hood.

(iii) Dissolve 40 g of phenol in 20 ml of n-butanol.

! CAUTION Phenol is toxic and can cause severe skin and eye damage. It shows germ cell mutagenicity, and it is hazardous to aquatic environments, with long-lasting effects. Wear appropriate protective equipment, and use a fume hood.

■ PAUSE POINT The stock solutions for the Kaiser test can be stored for up to 1 month at RT.

(iv) **Stock solutions for the peptide coupling reactions** (step iv, Timing 30 min) Weigh in Fmoc-Ala-OH, Oxyma, DIC and piperidine in a 50 ml conical centrifuge tube each, and dissolve them in DMF by the help of vortexing. Find the corresponding amounts for the synthesis of 0.5 mmol Fmoc-AAD-OH (**2**) in the table below.

Compound	Concentration	Total volume	Amount
Fmoc-Ala-OH	0.20 M	33 ml	2.1 g
Oxyma	1.0 M	10 ml	2.1 g
DIC	0.50 M	15 ml	1.6 ml
Piperidine	20 vol%	50 ml	12 ml

(v) **Peptide coupling reactions** (steps v–xvii, Timing 5 h) Add Fmoc-Asp(OtBu)-Wang resin (773 mg, 0.68 mmol/g loading, 1 eq.) with a total loading of 0.5 mmol into a 50 ml peptide vessel, and swell the resin in 20 ml DMF for 20 min. Use the shaker to accelerate the swelling.
(vi) Remove the solution by filtration through the frit with the assistance of a nitrogen gas flow.
(vii) To remove the Fmoc protection group, add 10 ml of 20 vol% piperidine to the resin and shake it for 15 min.
▲ **CRITICAL STEP** Do not let it react for more than 20 min to avoid epimerization of the last amino acid.
(viii) Remove the solution by filtration through the frit with the assistance of a nitrogen gas flow.
(ix) Wash the resin with 5 ml DMF three times.
(x) To perform the Kaiser test as a reaction control, transfer a small number of resin beads (less than 20 beads is sufficient) into a 5 ml glass sample vial.
(xi) Add one drop of the KCN, ninhydrin and phenol solutions (prepared in steps i–iii).
(xii) Carefully heat the tube to 100 °C for a few seconds with a heat gun. A blue coloration of the beads and the solution indicates a successful deprotection.
? TROUBLESHOOTING
(xiii) For the coupling of the next amino acid, add 10 ml of the 0.2 M Fmoc-Ala-OH solution (5 eq.), 2 ml of the 1.0 M Oxyma solution (5 eq.) and 4 ml of the 0.5 M DIC solution (5 eq.) to a 50 ml conical centrifuge tube, and mix the solutions. Add the solution to the resin in the peptide vessel, and agitate it for 1 h at RT.
(xiv) Remove the solution by filtration through the frit with the assistance of a nitrogen gas flow.
(xv) Wash the resin with 5 ml DMF three times.
(xvi) Confirm the successful coupling with the Kaiser test (steps x–xii). The absence of a blue coloration of the beads and solution indicates a complete coupling.
? TROUBLESHOOTING
(xvii) Repeat steps vii–xvi for the deprotection and the coupling of the second Fmoc-Ala-OH amino acid.
■ **PAUSE POINT** The resin can be stored for up to 1 month in the freezer at −20 °C.

Microcleavage as reaction control ● Timing 2 h

▲ **CRITICAL** We perform microcleavage after completing the synthesis to check the quality of the product. However, it can also be performed at any step during the synthesis to test if unexpected errors occurred.

2 Take a small amount of the resin (one spatula tip), and transfer it into a peptide vessel. Add 0.95 ml of TFA, 0.025 ml of TIPS and 0.025 ml of water.
! CAUTION TFA is toxic and highly corrosive. Wear gloves and protective gear, and use a fume hood while working with TFA.
3 Agitate the peptide vessel for 1 h at RT.
4 Collect the deprotection solution in a 25 ml round-bottom flask by filtering it through the frit with a nitrogen gas flow assistance. Wash the resin once with DCM.
5 Remove the DCM under reduced pressure (850 mbar at 40 °C). Remove the TFA by coevaporation with 5 ml of diethyl ether under reduced pressure. Start to remove diethyl ether at 850 mbar and 40 °C until no more condensate is observed. Reduce the pressure slowly to 40 mbar, and wait for 15 min. Repeat the coevaporation procedure (roughly three times) until almost no liquid is left.
6 Add 1 ml of a water:acetonitrile 60:40 vol/vol mixture, and dissolve the residue.
7 Filter the residue with a syringe filter, and dispense the filtrate in an HPLC vial.
8 Analyze the presence and purity of the peptide by HPLC and ESI-MS. Perform an analytical HPLC run, and detect the compounds at 254 nm. At this wavelength, the Fmoc group dominates the absorption of the peptide. The number of signals and their proportion offer a first estimation about the product purity (Fig. 9). ESI-MS analysis qualitatively confirms the successful synthesis. An analytical dataset is listed in Step 21.
? TROUBLESHOOTING

Peptide deprotection and cleavage from the resin ● Timing 3 h

9 To deprotect and cleave the peptide off the resin, we use a solution of TFA. Add 9.5 ml of TFA, 0.25 ml of TIPS and 0.25 ml of water to a 15 ml conical centrifuge tube and shake the solution.
10 Add the cleavage solution to the resin in the peptide vessel, and close the vessel with the corresponding cap. Shake the peptide vessel for 1 h.

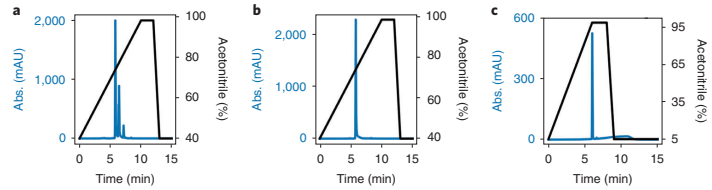

Fig. 9 | HPLC chromatograms of precursor Fmoc-AAD-OH (2) after purification detected at 254 nm and the applied pump gradient. a, The preparative HPLC chromatogram shows a synthesis approach yielding several side products, most likely caused by an old piperidine stock solution. **b**, A preparative HPLC chromatogram of a successful synthesis with only one observed product peak with high intensity. **c**, Analytical HPLC chromatogram to estimate the product purity. The peptide's purity is given by the proportion of the product integral compared with the combined integrals of all signals detected (product and impurities). The purity is determined to be 98% in the example shown.

11 Collect the deprotection solution in a 100 ml round-bottom flask by filtering it through the peptide vessel's frit with the assistance of a nitrogen gas flow. Wash the resin three times with DCM, and combine it with the deprotection solution.

12 Remove DCM and TFA as described in Step 5.
▲ **CRITICAL STEP** Use a dry ice cooling trap to prevent damage of the vacuum pump due to corrosion by TFA.
▲ **CRITICAL STEP** Do not store the peptide in concentrated TFA to prevent decomposition.

Preparative HPLC purification ● Timing 6 h

▲ **CRITICAL** The preferred method to purify the peptide is by reversed-phase HPLC with C_{18} as a stationary phase. We detect the compounds formed by absorption at 220 and 254 nm. The absorption at 254 nm is characteristic for the Fmoc-protected peptides and makes it easy to distinguish them from other side products. Detection at 220 nm gives an overview of further reaction products. Fractions are collected depending on the absorption at 254 nm with a start and end threshold of 15 mAU. As eluent, we used a mixture of water with 0.1 vol.% TFA and acetonitrile with 0.1 vol.% TFA. The eluents are degassed in a sonication bath for 30 min prior to use. A linear gradient of 40% acetonitrile to 98% acetonitrile over 10 min was applied at a flow rate of 20 ml/min, resulting in the successful separation of all reaction products (Fig. 9a,b). If the separation is not sufficient, the gradient can be prolonged to 20 or 30 min. The high acetonitrile content was maintained for 2 min to elute all compounds completely, and afterwards the starting condition was reset within 1 min. A final equilibration of 2 min resulted in a total runtime of 15 min per injection.

13 Dissolve the residual solution in 20 ml of a water:acetonitrile 60:40 vol/vol solution. Filter the solution with a polytetrafluoroethylene syringe filter (pore size 0.45 µm).
▲ **CRITICAL STEP** Different filters may be used, but make sure the filter material is resistant to acetonitrile.

14 Perform the first purification by using only 0.5 ml of the reaction solution. Check whether the separation is sufficient to collect individual peaks and whether the detector is not saturated.
▲ **CRITICAL STEP** A saturation of the detector can indicate a saturation of the stationary column phase, resulting in lower separation efficiency.

15 Analyze the peaks with the highest intensity at 254 nm by ESI-MS to verify the product peak.

16 For the subsequent runs, the amount of injected peptide solution can be gradually increased to reduce the total number of injections required. However, ensure that the peaks for the product do not start to overlap. Typically, 2–3 ml are injected, but the injection volume depends on the product concentration and the number of impurities. To reduce the collected fractions of unwanted side products with a low absorption at 254 nm, the threshold for peak collection at 254 nm can be increased. If the absorbance of side products is similarly high as the product peak, the collection can be done depending on the retention time instead of the absorbance.

17 According to the absorbance, combine all fractions that contain exclusively the product peak in a round-bottom flask. Additionally, combine in a separate round-bottom flask all fractions that partially contain the product peak. These fractions can be combined with the main product after analysis if they are of equal purity.

18 Remove the acetonitrile of the combined solutions under reduced pressure.

19 Transfer the remaining water solutions to 50 ml conical centrifuge tubes, and freeze them in liquid nitrogen.

! CAUTION Skin contact with liquid nitrogen leads to cold burn. Wear cryo gloves, safety glasses and a laboratory coat.

? TROUBLESHOOTING

20 Lyophilize the samples (2–3 d).

21 Perform analytical HPLC, ESI-MS (positive mode) and ^{1}H NMR analysis. Check that the product has the following analytical data before continuing with the procedure.

^{1}H-NMR (400 MHz, DMSO-d6): δ/ppm 8.10 (d, J = 8.0 Hz, 1H), 7.99 (d, J = 7.6 Hz, 1H), 7.90 (d, J = 7.6 Hz, 2H), 7.73 (t, J = 7.2 Hz, 2H), 7.52 (d, J = 7.7 Hz, 1H), 7.42 (t, J = 7.4 Hz, 2H), 7.34 (t, J = 7.4 Hz, 2H), 4.57–4.48 (m, 1H), 4.27 (td, J = 17.8, 6.9 Hz, 4H), 4.06 (d, J = 7.1 Hz, 1H), 2.72–2.55 (m, 2H), 1.28–1.17 (m, 6H).

ESI-MS: Fmoc-AAD-OH *m/z* calc.: 498.18 $[M + H]^+$, 520.17 $[M + Na]^+$, 536.14 $[M + K]^+$, found: 487.93 $[M + H]^+$, 520.27 $[M + Na]^+$, 536.07 $[M + K]^+$.

Analytical HPLC: gradient of acetonitrile:water (vol:vol) from 5:95 to 98:2 within 6 min and detection at 220 and 254 nm. Fmoc-AAD-OH (**2**) retention time 6.0 min.

22 The purity of the synthesized peptide can be estimated by integrating the signals in an analytical HPLC chromatogram (Fig. 9c). We typically obtain precursor **2** with a yield of 50% (122 mg) and a purity of 98% as a solid white powder.

Nile red assay

▲ CRITICAL For most precursors in dynamic self-assembly, there will be a concentration at which supramolecular structures will form directly from the precursor state. The critical aggregation concentration, which is determined by a Nile red assay[60], marks the upper limit at which concentration the precursor should be applied in the later-described fueling experiments ● Timing 2 h

23 Prepare 15 mM stock solutions of Fmoc-E-OH (**1**) and/or Fmoc-AAD-OH (**2**) by weighing in 11.1 mg and 14.9 mg of **1** and **2**, respectively. Transfer the compounds to a 2 ml volumetric flask, and dissolve them with 0.2 M MES pH 6.0.

▲ CRITICAL STEP There is no need to adjust the pH since the fluorescence is unaffected by pH between 4.5 and 8.5[54].

24 Set up a dilution row (from 15 mM to 2.5 mM) by mixing the stock solution with 0.2 M MES pH 6.0 inside microcentrifuge tubes. A final volume of 200 µl works well.

25 Prepare the 2.5 mM Nile red solution as described in 'Reagent setup'.

26 Add 0.4 µl of the Nile red solution to each centrifuge tube, and incubate the probe for 30 min in dark.

▲ CRITICAL STEP The dye should be added at low concentrations (<10 µM); higher concentrations may result in aggregation or self-quenching effects.

27 Transfer the solution to a quartz cuvette, and measure the fluorescence intensities at 635 nm when exciting the probes at 550 nm.

28 Plot the measured intensities against the applied precursor concentrations (Fig. 10a,b).

Kinetic analysis by HPLC

▲ CRITICAL For the kinetic analysis, we require calibration values for the applied precursor molecules and the chemical fuel. Both precursors Fmoc-E-OH (**1**) and Fmoc-AAD-OH (**2**) bear the large Fmoc-protecting group with a characteristic absorption at 254 nm. Since no other functional groups contribute substantially to the absorption, we use the calibration of **1** as a measure for **2** and the corresponding benzyl amides. The chemical fuel EDC is calibrated at 220 nm ● Timing Steps 29–34, 2 h; Step 35, 15 h automated HPLC measurement time

Setup and calibration

29 Create an HPLC method by defining the flowrate, pump gradient and detection wavelength. In our study, we used relatively short columns with a length of 100 mm. Thus, we applied a relatively low flow rate of 0.4 ml/min. We used the eluent 0.1% TFA in acetonitrile mixed with 0.1% TFA in water. The starting mixture was 2% acetonitrile, whose content increases up to 98% within 14 min. The high acetonitrile content was maintained for 3 min to elute all compounds completely, and afterwards the starting condition was reset within 1 min. Finally, the column was equilibrated for

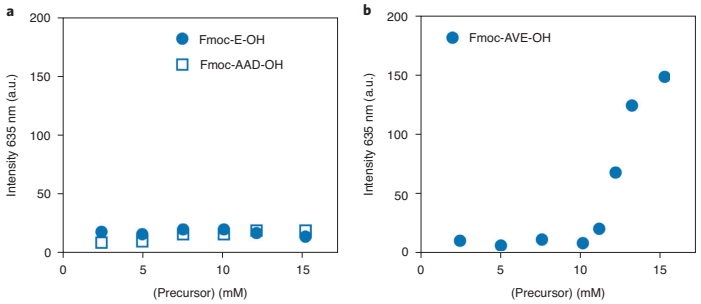

Fig. 10 | Nile red fluorescence intensity at 635 nm against concentration of the precursor. The intensity of the solvatochromic dye serves as an indication for self-assembly. **a**, No increase in fluorescence intensity of Nile Red is observed for concentrations <15 mM concerning precursor **1** and **2**. **b**, An example of a positive result of the Nile red assay. A sharp increase of the fluorescence intensity >10 mM of the more hydrophobic precursor Fmoc-AVE-OH indicates the formation of assemblies without EDC.

6 min at the original 2% acetonitrile in water. The detection was set to 220 nm and 254 nm at a data collection rate of 2.0 Hz.

▲ **CRITICAL STEP** TFA was added to the acetonitrile and water to improve the resolution as partial deprotonation of carboxylic groups is prevented at low pH.

30 Prepare in triplicate 1 ml stock solutions of **1** in 0.2 M MES pH 6 as described above. Create a dilution series starting from 10 mM and diluting down at 2 mM (10 mM, 8 mM, 6 mM … 0 mM). Typically, we prepare sample volumes of 100 µl in total. The resulting samples are further diluted 1:10 by the addition of 900 µl buffer.

▲ **CRITICAL STEP** The 1:10 dilution allows for higher injection volumes and removes the need for HPLC vial inserts, improving data quality.

31 Prepare 2.0 M EDC stock solutions in triplicate, as described above.

? TROUBLESHOOTING

32 Dilute the 2.0 M EDC stock to a final concentration of 100 mM by adding 285 µl water to 15 µl of 2.0 M EDC.

33 Set up a dilution row in triplicate as described in Step 30, starting from 100 mM and pipetting 20 mM intervals.

▲ **CRITICAL STEP** Prepare the EDC dilution row last, and use water instead of buffer to minimize hydrolysis.

34 Transfer the HPLC vials into the autosampler chamber.

35 Create an injection sequence at the HPLC. Apply the method created in Step 29. Consider that EDC reacts slowly with water and should thus be analyzed first. We used an injection volume of 1 µl. However, the injection volume can be increased depending on the sensitivity of the HPLC detector. Start the sequence.

▲ **CRITICAL STEP** The retention of the EDC is low on C_{18} columns. Start the gradient with a low percentage of acetonitrile (2%) to separate the EDC signal from the injection peak. If separation fails, the usage of longer columns increases the retention time.

▲ **CRITICAL STEP** When changing the solvent composition at the HPLC for the first injection, make sure to equilibrate the column with the new composition for around ten column volumes. At the applied settings, an equilibration time of 6 min is required.

? TROUBLESHOOTING

36 Integrate the peaks in each chromatogram for the peaks of EDC and **1**. Import the data in a data processing software. The mean area in mAU × min is plotted together with the standard deviation against the concentration injected (Fig. 11a,b). Then, the calibration value is calculated by the slope of the linear regression.

? TROUBLESHOOTING

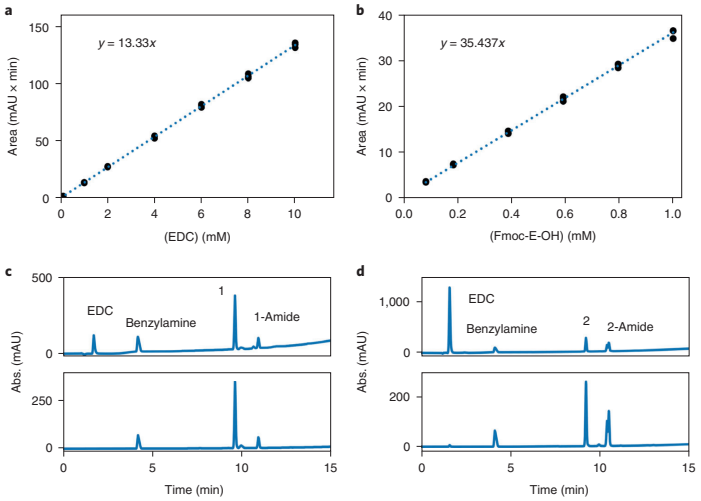

Fig. 11 | Calibration curves. a,**b**, The curves shown are of EDC (**a**) and precursor Fmoc-E-OH (**1**) (**b**) as measured at 254 nm. The markers represent HPLC data of injecting several concentrations in triplicate. The dotted line shows the linear regression of the experimental data and provides the calibration value given by the line equation. **c**,**d**, The chromatograms show the quenched reaction cycle of Fmoc-E-OH (**1**) (**c**) and Fmoc-AAD-OH (**2**) (**d**). The upper boxes show the retention profiles as detected at 220 nm, whereas the boxes below show the profiles recorded at 254 nm.

Kinetic analysis of the reaction cycle

▲ **CRITICAL** After the calibration values have been obtained, a kinetic analysis of the reaction cycle is started. The evolution of the reaction cycle's components is monitored for 120 min

● Timing Steps 37–44, 6 h; Step 45, 12 h automated HPLC measurement time

37 Prepare the benzylamine, EDC and corresponding precursor solution as described in 'Reagent setup'.
? TROUBLESHOOTING

38 For each datapoint in the time series, pipette 450 µl of the benzylamine solution in an HPLC vial.
▲ **CRITICAL STEP** Close each vial after pipetting to prevent evaporation of the solvent.

39 Prepare three HPLC vials for the actual reaction cycle by adding 995 µl of the Fmoc-E-OH (**1**) stock solution to each vial. For Fmoc-AAD-OH (**2**), 950 µl of the stock solution should be added.

40 Start the reaction cycle by adding 5 µl of the 2.0 M EDC stock solution to the first vial containing **1** (50 µl of the 2.0 M EDC to precursor **2**), and start the timer. Fuel the remaining two vials with a delay of 20 s.
▲ **CRITICAL STEP** Be aware of adequate mixing of the EDC and precursor solution by pipetting the solution up and down.
▲ **CRITICAL STEP** The dilution factor of the precursor solution should not exceed 5% when EDC is added; otherwise, the precursor concentration differs too much from the applied concentration.

41 Quench the reaction cycle at the planned time points. Start with the first vial activated by removing 50 µl of the reaction mixture, and add it to a vial with the quenching solution prepared in Step 38. Mix the solution by pipetting it up and down, which aids the dissolution of the assemblies. Quench the remaining two samples of the triplicate datapoint, which were started with a delay of 20 s and 40 s.
▲ **CRITICAL STEP** To accurately determine the anhydride concentration by means of the formed amide, the transformation should be complete and should outcompete the hydrolysis reaction. As a test, dissolve a definite amount of synthesized anhydride in acetonitrile and dilute with the quenching solution. Inject the sample into the HPLC right after dilution. The measured amide should equal the anhydride weighed in, and no acid signal should appear in the chromatogram.
? TROUBLESHOOTING

42 Store the quenched samples at 4–8 °C.
▲ CRITICAL STEP Do not store the samples longer than 12 h; at longer time periods, the Fmoc deprotection reaction will start to affect the reliability of the measurements (Extended Data Fig. 2a,b)[56].
43 Repeat Steps 41 and 42 for the remaining samples at the planned time intervals until the cycle is finished.
? TROUBLESHOOTING
44 Program the HPLC injection sequence as described in Step 29. Set the injection volume to 1 µl. Additionally, set the autosampler temperature to 8 °C to reduce side reactions.
45 Transfer the samples to the HPLC autosampler, and start the analysis sequence programmed in the step before. This step takes 7 h; this timing is mainly dependent on the components' retention time on the HPLC column.
46 The obtained chromatograms show four peaks corresponding to the EDC, the benzylamine, the precursor **1** or **2**, and their corresponding benzylamide (Fig. 11c,d). Over time, the EDC peak decreases, the precursor peak initially decreases but then returns to its original level, and the benzylamide follows the opposite trend.
▲ CRITICAL STEP To align the signals correctly, compare the retention times with the previously performed calibration experiments. In addition to that, the signals should be collected after detection and analyzed by ESI-MS.
? TROUBLESHOOTING
47 Calculate the area under the EDC and amide signals (at 220 nm and 254 nm, respectively) by integration.
48 Convert the values of the area into concentration by applying the corresponding calibration factors.
▲ CRITICAL STEP Determine the concentration of anhydride during the reaction cycle by calculating the concentration of the corresponding amide.
▲ CRITICAL STEP The dilution factor when adding the quenching solution must be considered to obtain the concentrations during the reaction cycle. Regarding the described 1:10 dilution, a multiplication by a factor of 10 is required.
49 Plot the EDC and anhydride concentration against the time the reaction cycle was quenched (Fig. 2).

Using a kinetic model in MATLAB

▲ CRITICAL We use a kinetic model written in MATLAB to predict the concentrations in the reaction cycle throughout our experiments. A download link for the model is provided in the supplementary information. The rate constants are determined by fitting the experimental concentration curves of EDC and anhydride obtained from HPLC measurements. The relevant reactions are the hydration of EDC (k_0), the second-order activation reaction (k_1), the transformation into a cyclic anhydride (k_2), the hydrolysis of the O-acylisourea intermediate (k_3) and, finally, the hydrolysis of the anhydride (k_4) ● Timing 2 h
50 Create a new folder, and rename it 'Model'.
51 Create a folder within 'Model', and name it 'Data'.
52 Open a basic text editor, and create and save the experimental datasets obtained by HPLC as comma-separated text files (.dat). For each kinetic experiment, three files should be created, i.e., time.dat, anhydride.dat and edc.dat. Each of these files should contain the data in a row with the datapoints separated by commas. The units of the data should be in min for time and mM for concentration. It is important that each file contains the same number of data points. Exemplary files can be downloaded from GitHub.
53 Download our MATLAB script 'kinetic_model.m' from the supporting, and save it in the 'Model' folder.
54 The main script 'kinetic_model' contains variables (lines 6–17) that are varied depending on the reaction conditions and the different precursors used. Set the time variable 't' to the time frame of the experiment in minutes.
55 Set the variable 'Acid' and 'Fuel' to the precursor and fuel concentration in mM used in the experiment.
56 Assign the reaction rate constant 'k_0' to the value 0.0000135 for reactions in 0.2 M MES buffer pH 6.0[39].
57 Set the 'feedback' variable to 1 or 0, depending on whether self-protection of the assemblies is expected or not. We showed that anhydrides that form colloids, such as Fmoc-E-OH (**1**), protect the anhydride from hydrolysis by water[42]. Only the fraction anhydride in solution hydrolyzes. The fraction that remains in solution is defined as the variable 'solubility' and has to be set as well.

For the anhydride of Fmoc-E (**1**) in 200 mM MES, that value is 0.4 mM. In the calculations, the model switches from pseudo first-order hydrolyses of the anhydride to zero-order hydrolysis when the concentration anhydride reaches a value above the solubility. The feedback variable is set to 0 for hydrogel-forming precursors such as Fmoc-AAD-OH (**2**).

58 Start the fitting process by finding the best fit for the decay of the EDC concentration. This concentration is only affected by the direct hydration (k_0) and the reaction with precursor (k_1). The direct hydration was entered in the Step 56. The decay curve can thus be fitted by varying k_1. For our dataset, k_1 for precursor **1** was set at 0.037 and for precursor **2** at 0.11.

59 Fit the evolution of the anhydride by varying the rate constants k_2, k_3 and k_4. k_2 is the first-order conversion of the O-acylurea to the anhydride. Because we cannot detect the O-acylisourea, we know that k_2 has to be higher than k_1. Therefore, we describe k_2 as a factor of k_1 (in the case of Fmoc-E (**1**) and Fmoc-AAD (**2**) $4 \times k_1$). Similarly, we set the second-order k_3 as a factor of k_1 (in the case of Fmoc-E (**1**), $0.01 \times k_1$ and Fmoc-AAD (**2**) $2 \times k_1$). k_4 is the anhydride hydrolysis and is set to 0.0048 for Fmoc-E (**1**) and 0.009 for Fmoc-AAD (**2**).

Time-lapse photography ● Timing Steps 60–65, 30 min; Steps 66–70, 1.5 h measurement time

60 Put an elevated flat surface like a magnetic stirrer or a lifting platform on the laboratory bench as a sample holder. Ensure that the surface is level.
▲ **CRITICAL STEP** Set the webcam up in an air-conditioned room with a constant temperature to avoid nonreproducible results due to, e.g., temperature changes during day and night.

61 Behind the sample holder, install a black sheet of paper glued to a flat piece of cardboard.
▲ **CRITICAL STEP** Other colors are possible, but a black background gives the best contrast for the turbid solutions.

62 Stick a strip of double-sided sticky tape to the flat and leveled sample holder, ~1 cm in front of the background (Fig. 8b). The sticky tape will prevent the samples from falling or moving during the time lapse. Alternatively, use a stand to place the samples.

63 Install the retort stand in front of the sample holder. Use a clamp to hold the webcam in place. Adjust the webcam to get a focused image with centered samples. Alternatively, use a tripod for the webcam.

64 Prepare the samples.
- **For Fmoc-E-OH** (**1**), use four 1.7 ml HPLC vials, and pipette 1 ml of the 10 mM stock solution of **1** into it.
- **For Fmoc-AAD-OH** (**2**), take a 1.7 ml HPLC vial, and pipette 400 µl of the 10 mM Fmoc-AAD-OH (**2**) stock solution into it.
▲ **CRITICAL STEP** Do not use smaller vials for hydrogel-forming precursors like **2**. The increased wall-surface area to volume may lead to false-positive results in the inverted tube test because of increasing capillary forces.

65 Position the samples, and adjust the lighting, background and webcam by checking the quality of the shots.

66 Start the imaging with the time-lapse software, and save the images with a time stamp. We recommend a time interval of 1 min between image acquisitions.
▲ **CRITICAL STEP** After 5 min, check the focus of the webcam and readjust it if necessary. The focus can drift as the camera is warming up during image acquisition.

67 Start the reaction cycle by the addition of EDC.
(A) For Fmoc-E-OH (**1**), add EDC to the samples according to the table below. Mix the samples by pipetting the solution up and down five times. Close the vials.

[EDC]	6.0 mM	8.0 mM	10 mM	12 mM
2 M EDC stock	3.0 µl	4.0 µl	5.0 µl	6.0 µl

(B) For Fmoc-AAD-OH (**2**), add 20 µl of a 2.0 M EDC stock solution to the sample to get a final concentration of 100 mM EDC. Mix the sample by pipetting the solution up and down five times. Close the vials. After 5 min, invert the vial on its cap for the inverted tube test.

68 Place a large cardboard box over the entire setup to avoid changes in the illumination conditions, e.g., due to sunset or reflections.

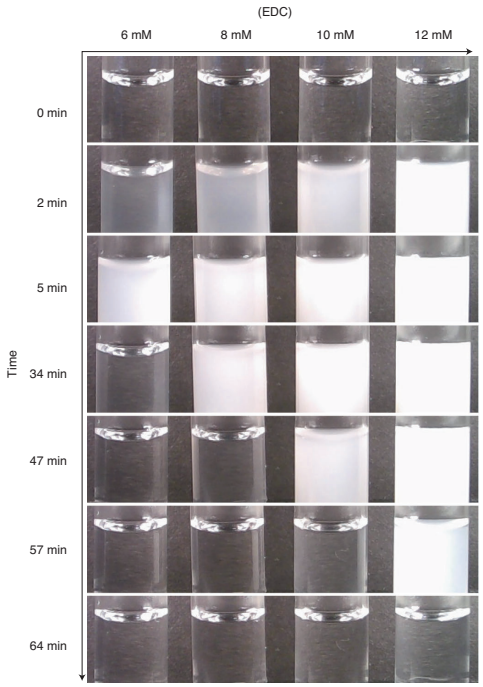

Fig. 12 | Time-lapse series of photographs shows the activation of 10 mM Fmoc-E-OH (1) with several amounts of EDC. An increase in fuel concentration results in a longer persistence of the assemblies. We show the photographs directly after the addition of fuel (0 min) and 2 min and 5 min after fuel addition. From there on, we show the timepoints after a sample has reached transparency (34, 47, 57 and 64 min).

69 After the reaction cycle is completed, determine the assemblies' lifetime for each fuel concentration according to the time the turbidity is depleted.

70 Present the data as photographs, indicating the amounts of fuel added and the timepoints when taking the image (Figs. 3a, 4a and 12).

UV-VIS measurement

▲ **CRITICAL** In UV-VIS spectroscopy, it is important that the absorption values are not much higher than one absorbance unit. At high concentrations, the response of the instrument is nonlinear, because insufficient light reaches the detector. Given Lambert–Beer's law, the extinction can be tuned by the path length of the light penetrating the sample. For precursor Fmoc-E-OH (**1**), a 1 mm quartz cuvette gave good results ● Timing Steps 71–73, 1 h; Steps 74–75, 2 h measurement time

71 A kinetic loop is programmed by the plate reader software, recording the absorbance of light at 600 nm at predetermined times. We estimate the length of the experiment by webcam experiments done beforehand. In the described experiment, we measured the absorbance every 30 s for 100 min.

72 A baseline is recorded, which is subtracted from the later fueled samples. Load the cuvette with 300 µl of the Fmoc-E-OH (**1**) stock solution, and monitor the baseline for ~10 min.

73 Then, prepare a 1.7 ml microcentrifuge tube with 300 µl of the Fmoc-E-OH (**1**) stock solution, and start the reaction cycle by adding 1.5 µl of the 2.0 M EDC stock solution. After mixing thoroughly, transfer the reaction mixture into the quartz cuvette and load the plate

reader's chamber. Start the measurement, and continue recording until the absorption reached its starting value.

▲ **CRITICAL STEP** The choice of the sample container can influence the data quality (Extended Data Fig. 3a,b).

74 Repeat Step 73 for various EDC concentrations by changing the volume of the EDC stock solution added.

75 Subtract the calculated mean baseline value from the obtained absorbance values. Then, plot the absorbance over time (Fig. 3b).

? TROUBLESHOOTING

Correlation with the kinetic model

▲ **CRITICAL** For a better understanding of the self-assembly process, we correlated the turbidity to the anhydride concentrations obtained by the kinetic model.

76 We used a threshold value of 0.01 absorbance units to define when assemblies were present or not. We determined when the solution passed through this threshold to determine when the assemblies had dissolved and plotted these timepoints against the amount EDC added (Fig. 3c).

77 Using the kinetic model, we calculated the concentrations of anhydride product when the assemblies had dissolved. This concentration was considered the solubility and was determined for several amounts of EDC added.

78 Determine the time point when the anhydride concentration passes below its solubility using the kinetic model for various EDC concentrations. The results are added to the graph drawn in Step 76 (Fig. 3c).

Rheological characterization

▲ **CRITICAL** We conduct rheological measurements to determine the time-dependent viscoelastic properties of the precursor **2** in response to EDC. A research-grade shear rheometer was used, applying a plate/plate measuring setup ● Timing Steps 79–84, 30 min; Step 85, 1 h measurement time

79 Make sure the device is heated up, i.e., switch the rheometer 'ON' at least 30 min before conducting the experiments.

80 Mount the bottom plate, and insert the measuring head into the device. Install a humidity trap, and switch on the temperature control (here, $T = 25$ °C) to allow for equilibration.

81 Initialize the setup by performing the following preset calibration protocols in the correct order, and check for success by running a blank.
(1) Set zero gap (determines the distance between the bottom plate and measuring head
(2) Motor adjustment (ensures the angular deflection is determined correctly)
(3) Determine inertia of the measuring head

82 Prepare a measuring protocol for oscillatory shear measurements. Set the measuring gap to $d = 300$ µm. The oscillating frequency should be fixed to a value of 1 Hz and the shear deformation to $\gamma = 1\%$ as, at those values, linear material response can be expected

▲ **CRITICAL** Always measure with the same gap size to allow for comparison.

? TROUBLESHOOTING

83 Start the measurement by lowering the measuring head to an appropriate loading position. As the measurements will record a dynamic material, data recording should start immediately after sample addition to not lose information in the beginning. Consequently, the ideal loading position should be as low as possible while still allowing to load the sample into the measuring gap. We here found 30 mm to be suitable for this purpose.

84 Quickly mix the 10 mM precursor stock solution of **2** with the 2.0 M EDC fuel in a 20:1 (vol:vol) ratio by using a pipette and transferring 150 µl of the mixture into the measuring gap. Immediately afterward, lower the head to the measuring position, close the humidity trap to avoid evaporation, and start the measurement.

▲ **CRITICAL STEP** As the initial gel formation happens very quickly, the transfer to the measuring system should be as fast as possible. Otherwise, mechanical shear during the pipetting process and when lowering the measuring head to the measuring position might already damage the supramolecular structure, thus falsifying the obtained results. First, it is recommended to fill the highly concentrated EDC solution into a microcentrifuge tube, then add the precursor solution that automatically mixes both components and, finally, pipette the mixture without further homogenization into the measuring gap.

85 Record data for a time span of 60 min at a data acquisition frequency of 1 Hz.
86 Plot the viscoelastic moduli against time (Fig. 4b).

Compare rheology lifetime with anhydride concentrations

▲ **CRITICAL** We compare the lifetimes derived from the rheology experiment to the anhydride concentrations obtained from the kinetic experiment.

87 Determine the timepoint of the storage modulus falling below the loss modulus, indicating a gel-to-sol transition. Regarding the activation of **2** with 100 mM fuel, this transition occurs at 42 min.
88 With the kinetic model, calculate the anhydride concentration at 42 min when fueled with 100 mM EDC. When falling below this anhydride concentration (0.45 mM), the end of the lifetime is expected.
89 Redo the calculation for several fuel concentrations, and note the anhydride concentration's timepoints falling below 0.45 mM.
90 Plot the lifetime against the applied fuel concentration of the experimental values together with the calculated ones (Fig. 4c).

Analysis by confocal laser scanning fluorescence microscopy

Sample preparation ● **Timing 10 min**

91 Take a 2 ml syringe, and fill it with vacuum grease by removing the plunger.
92 Cut the upper 4 mm of a 200 µl pipette tip, and mount it on the syringe.
93 Take a rectangular glass microscope cover slide, and draw a greased circle with a diameter of 5 mm onto it (Fig. 13a).
94 Take 200 µl of the 10 mM peptide stock solution of Fmoc-E-OH (**1**) or Fmoc-AAD-OH (**2**), and pipette them into a 1.7 ml centrifuge tube each.
95 Add 0.2 µl of a 2 mM Nile red stock to the samples, resulting in a concentration of 2 µM in the sample.
96 Start the reaction cycle.
(A) Fmoc-E-OH (**1**)
(i) Add 1 µl of a 2.0 M EDC stock to the precursor solution, resulting in 10 mM concentration, and mix with a 200 µl pipette five times.
(ii) Pipette 20 µl of the reaction solution into the grease chamber (Fig. 13b).
(B) Fmoc-AAD-OH (**2**)
(i) Pipette 1 µl of a 2.0 M EDC stock into the grease chamber (Fig. 13b).
(ii) Add 20 µl of the precursor solution of **2** on top of the EDC, and mix it with the pipette five times.
▲ **CRITICAL STEP** For hydrogel-forming precursors like Fmoc-AAD-OH (**2**), transferring the activated reaction mixture from a microcentrifuge tube to the microscope glass slide causes shear stress upon the built fiber network. The fiber network's damage can be avoided by adding the respective amount of EDC onto the glass slide first and then adding the peptide solution (Fig. 13e,f).
97 Seal the grease chamber with a small cover slide (Fig. 13c).
98 Gently press down the cover slide with a tweezer to remove air bubbles (Fig. 13d).
▲ **CRITICAL STEP** Prevent applying too much pressure. Otherwise, the sample will break through the grease and spill on the glass slide.

Imaging of the samples ● Timing 10 min

99 Excite the samples with a 552 nm laser or similar, and image them at 580–700 nm. Use a 63× objective and a HyD to image the samples.
100 Set the imaging parameters depending on the mobility of the samples. The following examples can be used as guidelines:
(A) Since the fibers formed by **2** in response to EDC are quite static, a slow scan speed and line averaging results in a good resolution. Use a scan speed of 10–100×, a line average of 4–16 and a pinhole size of 1 AU. For the image size in pixels, consider the ideal Nyquist sampling frequency according to the microscope setup used.
▲ **CRITICAL STEP** Do not image the assemblies that are close to the glass surfaces. Possible interactions with the surface lead to results that are not representative.
(B) The colloids formed by **1** in response to EDC move rapidly because of Brownian motion, and therefore, a quicker scan speed and lower line averages result in better-resolved images. Use a

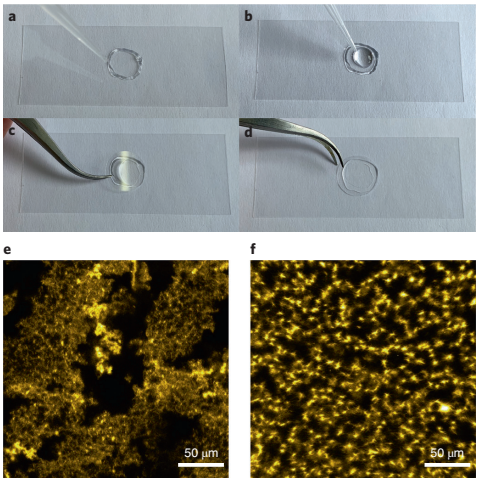

Fig. 13 | Preparation of a microscope glass slide with a grease chamber for microscope imaging. a, Preparation of a grease ring on a microscope slide by using a grease-filled syringe. **b**, Pipetting the sample into the grease ring. **c**,**d**, Closing the grease chamber with a cover slide. **e**, The micrographs show the effect of sample deposition. Confocal microscope micrographs of 10 mM Fmoc-AAD-OH (**2**) fueled with 100 mM EDC. We added EDC to a separate vial together with the precursor. Directly afterwards, the mixture was pipetted on the microscope slide. Shear forces of the pipetting after activation destroy the fibers. As a result, the fibers agglomerate and are not homogeneously distributed over the glass slide. **f**, The EDC was put on the microscope slide first, and the precursor is added on top of the EDC. This sample preparation prevents the rupture of peptide fibers and results in a homogeneous fiber network.

scan speed of 100–600×, no line averaging and a pinhole size of 1 AU. For the image size in pixel, consider the ideal Nyquist sampling frequency according to the microscope setup used.
▲ **CRITICAL STEP** Do not image the assemblies that are close to the glass surfaces. Possible interactions with the surface lead to results that are not representative.

101 Save the images in LIF format, and analyze them with Fiji-ImageJ.

102 Present the micrographs' relevant parts together with scale bars (Figs. 3d,e and 4d,e).

Analysis by cryo-TEM

Sample preparation ● **Timing 2 h**

103 Prepare two 50 µl samples, each of 10 mM Fmoc-E-OH (**1**) and Fmoc-AAD-OH (**2**) in a 1.7 ml centrifuge tube.

104 Set the Vitrobot temperature to 23 °C and the relative humidity to 100%. Set the automated blotting procedure to 30 s waiting time, 2.5 s blot time and −1 blot force.

105 Wrap paraffin film around a microscope slide, and put two Cu grids (2 µm hole size, 2 µm spacing, 400 mesh) for each sample and one additional as a backup on the paraffin film with the carbon side facing upwards. The paraffin film holds the grids in place during plasma cleaning and makes it easier to remove the microscope slide's grids.

106 Position the microscope slide in a plasma cleaner, and plasma treat the grids for 1.5 min at a 50 mA voltage and a pressure of 3×10^{-2} mBar. This step will hydrophilize the grids.

107 Cool the ethane pot with liquid nitrogen, and slowly fill in the gaseous ethane until the ethane pot is filled up with liquid ethane.
▲ **CRITICAL STEP** Use a low ethane flow to prevent it from spilling and freezing in the liquid nitrogen. Frozen ethane might impact the quality of the blotted grids during the transfer into the grid box.
! **CAUTION** Skin contact with liquid ethane leads to cold burn. Wear a face shield, a laboratory coat and gloves.

108 Insert the grid box in the liquid nitrogen of the ethane pot.

109 Start the reaction cycle by adding EDC to the precursor solution. At predetermined time points, take away the sample and process it in the Vitrobot. Blot at least two grids for each sample.
(A) **Fmoc-AAD-OH (2)**
(i) To a sample of 50 µl of 10 mM Fmoc-AAD-OH (**2**), add 2.5 µl of 1.0 M EDC to get a concentration of 50 mM of EDC.
▲ **CRITICAL STEP** The EDC concentration and waiting time are essential to obtain acceptable cryo-TEM images. These parameters determine how many assemblies will be present. If the assemblies' density is too high, the thickness of the sampled ice will increase, which hampers imaging. If the concentration of assemblies is too low, no assemblies might be present during imaging.
(ii) Take a grid with the Vitrobot tweezers, attach them to the Vitrobot and bring the ethane pot into the lifted plunge freezing position.
? TROUBLESHOOTING
(iii) After 2 min, shake the sample thoroughly, thereby breaking the gel, and pipette 5 µl of the reaction solution on the grid's hydrophilized carbon side.
? TROUBLESHOOTING
(B) **Fmoc-E-OH (1)**
(i) Add 1 µl of 0.5 M EDC to a 50 µl 10 mM Fmoc-E-OH (**1**) sample to yield a concentration of 10 mM of EDC.
(ii) Take a grid with the Vitrobot tweezers, attach them to the Vitrobot and bring the ethane pot into the lifted plunge freezing position.
? TROUBLESHOOTING
(iii) After 1 min, shake the sample gently and take 5 µl of the reaction solution and pipette it on the grid's hydrophilized carbon side.
? TROUBLESHOOTING
110 Blot the grid by starting the automated blotting procedure on the Vitrobot.
111 Transfer the copper grid in a grid holder, and store the holder in liquid nitrogen.
■ **PAUSE POINT** Samples can be stored in liquid nitrogen for up to 1 week.

Imaging of the samples ● **Timing 30 min**
112 Transfer the grid into a cryo-transfer-specimen holder precooled with liquid nitrogen to maintain the specimen temperature at −170 °C or below during the imaging process.
113 Insert the holder into the TEM.
114 Search for holes with assemblies and a proper ice thickness. A good hole can be recognized by a good contrast and visible borders.
115 Acquire bright-field images in low-dose mode at a magnification of 21,000×, and vary the exposure time between 1 and 2 s depending on the intensity.
▲ **CRITICAL STEP** Image at least three different holes in three different squares distributed over the grid to ensure that the images are representative for the sample.
? TROUBLESHOOTING
116 Save images in MRC format, and analyze them with Fiji-ImageJ.
117 Present the micrographs with scale bars (Figs. 3f and 4f).

Troubleshooting

Troubleshooting advice can be found in Table 2.

Table 2 | Troubleshooting table

Step	Problem	Possible reason	Solution
1A(vi)	Peptide synthesizer has stopped the synthesis because of an error	Full waste container; pressure drop due to leakage	Empty the waste container; check the reagent bottles and the reaction vessel for any leakage of gas or liquid; drain the reaction vessel, and wash the resin with 5 ml DMF; swell the resin for 10 min in DMF if the synthesis was stopped for >30 min; restart the synthesis from the step when it stopped
1B(xii)	No coloration	Unsuccessful deprotection	Repeat Step 1B(vii–xii)

Table continued

Table 2 (continued)

Step	Problem	Possible reason	Solution
1B(xvi)	Blue coloration	Incomplete coupling	Repeat Step 1B(xiii–xvi)
8	Peptide mass not found in mass spectrum; HPLC chromatogram shows many signals	Required peptide was not synthesized or at low purity; often encountered with old stock solutions of piperidine	Prepare a fresh piperidine stock solution
19	Low rate of lyophilization	Huge sample volume (low surface-to-volume ratio)	Split up the total volume into several smaller ones
31	How to check resulting volume	Volumetric flask is not available	The end volume can be tested by aspiration of the solution with pipettes: after aspiration, test the volume by turning the volume-adjusting knob
35	Saturation of the absorption signal	Too much probe was injected	Dilute the samples; decrease the injection volume; change to higher wavelengths
36	Calibration value has changed over time	The intensity of the light source and the sensitivity of the detector decrease over time	Repeat Steps 30–36, and determine new calibration values
37	Precursors do not dissolve	Solubility of Fmoc-protected precursors is low in aqueous buffer	Sonicate the samples; adjusting the pH to basic conditions increases the solubility of acid precursors
41	Assemblies do not dissolve	The acetonitrile content is not sufficient to dissolve the assemblies instantly	Increasing the acetonitrile content in the quenching solution increases the solubility of the assemblies when the quenching solution is added; the drawback is the decrease in EDC retention time when analyzing the samples by HPLC
	Homogeneous pipetting fails	Hydrogel precursors like **2** form stiff fibers	Vortex the HPLC vial for 5 s; use wide bore pipette tips
43	Insufficient pipetting time	The proposed method saves time as triplicate data are obtained within the time of one reaction cycle, but a routine in fast pipetting is required	Increase the time intervals between the triplicate samples; start only one reaction cycle
46	The EDC signal is not resolved from the injection peak	The EDC retention on C18 columns is low; the retention is further decreased when the injected probe contains acetonitrile; the added acetonitrile causes big injection signals	Start the pump gradient with low acetonitrile content (2%); prepare the quenching solution with a resulting acetonitrile concentration <5% in the quenched samples; lower the flow rate; use longer columns
	The signal areas have changed	The HPLC method created in Step 29 has been changed	Apply the same methods regarding the calibration and the kinetic measurement; changes in, e.g., the flow rate can affect the signal area[61]
75	Saturation of the UV-VIS signal	High probe concentration	Try cuvettes with different path lengths
82	Nonlinear material response	Deformation of $\gamma = 1\%$ already too high	Perform a torque-controlled measurement: the torque should be selected as small as possible ($M = 0.5$–1 mNm). The drawback is a slightly lower signal-to-noise ratio
109A/B (ii)	Not enough time to attach the tweezers between starting the reaction cycle and the sampling time point		Attach the tweezers and lift the ethane pot before starting the reaction cycle. This still needs to be done quite quickly; the longer the ethane pot remains in the lifted position, the more likely it is that the ethane freezes, which might reduce the quality of the blotted grid
109A/B (iii)	Liquid ethane freezes during the waiting time	The ethane pot is too long in the lifted waiting position, or the ethane pot is filled with too much liquid nitrogen	Reduce the amount of liquid nitrogen in the ethane pot to prevent spillage into the liquid ethane while it is in the lifted waiting position; try to minimize the time the ethane pot is in the lifted waiting position
115	Not possible to properly focus on the sample, because the ice on the grid is too thick	Often apparent for hydrogel-forming precursors like **2** at high anhydride concentrations	Reduce the concentration of assemblies formed in the sample by reducing the EDC concentration; freeze the samples at an earlier time point in the cycle

Timing

Step 1A, automated solid-phase peptide synthesis: 2.5 h
Step 1B, manual solid-phase peptide synthesis: 6 h
Steps 2–8, microcleavage as reaction control: 2 h
Steps 9–12, peptide deprotection and cleavage from the resin: 3 h
Steps 13–22, preparative HPLC purification: 6 h

Steps 23–28, Nile red assay: 2 h
Steps 29–36, calibration: 17 h
Steps 37–49, kinetic analysis by HPLC: 18 h
Steps 50–59, using a kinetic model in MATLAB: 2 h
Steps 60–70, time-lapse photography: 2 h
Steps 71–78, UV-VIS measurement: 3 h
Steps 79–90, rheological characterization: 1.5 h
Steps 91–102, analysis by confocal laser scanning fluorescence microscopy: 20 min
Steps 103–117, analysis by cryo-TEM: 2.5 h

Anticipated results

We have referred to analytical data and figures at the 'Procedure' steps where it is required in order to know whether to proceed to the next step.

The synthesis of **2** can be monitored by cleaving and analyzing small fractions from the solid support (Steps 2–8). Figure 9 compares results from two experiments that yielded different amounts of side products. An increased appearance of side products can be referred to the quality of the piperidine stock solution, which should be exchanged occasionally. Additionally, the composition of the crude product provides information on the subsequent purification steps regarding the pump gradient or injection volumes (see Steps 14–17).

The Nile red assay (Fig. 10) is used to determine the concentrations at which the precursors can be applied in the later fueling experiments. The concentration of the reaction cycles' products can be determined by HPLC using calibration curves prepared as described in Steps 29–36 (Fig. 11a,b). The concentration ranges will depend on which precursors are applied and which HPLC setup is used. A typical HPLC chromatogram that can be expected applying this protocol is shown in Fig. 11c,d. To correctly align the reaction cycle's components, all signals must be resolved. Therefore, often an adaption of the pump gradient described in Step 29 is helpful.

The webcam experiment provides valuable information about what further experiments can be conducted. Whereas transient turbid solutions indicate the presence of dynamic assemblies, a differentiation between, e.g., colloids and hydrogels can be made by inverting the vials (Step 67B). Samples with a transient turbidity should be further analyzed by UV-VIS measurements. For hydrogel-forming precursors, rheology is a suitable follow-up technique. In UV-VIS experiments, the physical properties of the assemblies dictate the choice of the sample container (Extended Data Fig. 3a,b). Before the screening of several EDC concentrations (Step 74), several containers should be tested. Figure 13e,f shows how incorrect sample preparation effects the assemblies' structures during confocal laser scanning fluorescence microscopy. Depending on the nature of the precursor, the guidelines provided in either Step 96A or 96B should be considered as a correct way of sample preparation.

Reporting Summary

Further information on research design is available in the Nature Research Reporting Summary linked to this article.

Data availability

The authors declare that all the data supporting the findings of this study are available within the article, the source data files and the Supplementary Information files. Source data are provided with this paper.

Software availability

The MATLAB code used in this protocol together with an exemplary dataset is provided at https://github.com/BoekhovenLab/Nature_protocols. Source data are provided with this paper.

References

1. Stupp, S. I. et al. Supramolecular materials: self-organized nanostructures. *Science* **276**, 384–389 (1997).
2. Amabilino, D. B., Smith, D. K. & Steed, J. W. Supramolecular materials. *Chem. Soc. Rev.* **46**, 2404–2420 (2017).
3. Zhou, J., Li, J., Du, X. & Xu, B. Supramolecular biofunctional materials. *Biomaterials* **129**, 1–27 (2017).
4. Kato, T., Uchida, J., Ichikawa, T. & Soberats, B. Functional liquid-crystalline polymers and supramolecular liquid crystals. *Polym. J.* **50**, 149–166 (2017).

5. Hegmann, T., Qi, H. & Marx, V. M. Nanoparticles in liquid crystals: synthesis, self-assembly, defect formation and potential applications. *J. Inorg. Organomet. Polym. Mater.* **17**, 483–508 (2007).
6. Greaves, T. L. & Drummond, C. J. Ionic liquids as amphiphile self-assembly media. *Chem. Soc. Rev.* **37**, 1709–1726 (2008).
7. de Greef, T. F. & Meijer, E. W. Materials science: supramolecular polymers. *Nature* **453**, 171–173 (2008).
8. Aida, T., Meijer, E. W. & Stupp, S. I. Functional supramolecular polymers. *Science* **335**, 813–817 (2012).
9. Weingarten, A. S. et al. Self-assembling hydrogel scaffolds for photocatalytic hydrogen production. *Nat. Chem.* **6**, 964–970 (2014).
10. Grimaldi, N. et al. Lipid-based nanovesicles for nanomedicine. *Chem. Soc. Rev.* **45**, 6520–6545 (2016).
11. Webber, M. J. & Langer, R. Drug delivery by supramolecular design. *Chem. Soc. Rev.* **46**, 6600–6620 (2017).
12. Kadler, K. E., Holmes, D. F., Trotter, J. A. & Chapman, J. A. Collagen fibril formation. *Biochem. J.* **316**, 1–11 (1996).
13. Zhu, J. & Kaufman, L. J. Collagen I self-assembly: revealing the developing structures that generate turbidity. *Biophys. J.* **106**, 1822–1831 (2014).
14. Prockop, D. J. & Kivirikko, K. I. Collagens: molecular biology, diseases, and potentials for therapy. *Annu. Rev. Biochem.* **64**, 403–434 (1995).
15. Zhao, B., Hu, H., Mandal, S. K. & Haddon, R. C. A bone mimic based on the self-assembly of hydroxyapatite on chemically functionalized single-walled carbon nanotubes. *Chem. Mater.* **17**, 3235–3241 (2005).
16. Amendola, V. & Meneghetti, M. Self-healing at the nanoscale. *Nanoscale* **1**, 74–88 (2009).
17. Tantakitti, F. et al. Energy landscapes and functions of supramolecular systems. *Nat. Mater.* **15**, 469–476 (2016).
18. Lancia, F., Ryabchun, A. & Katsonis, N. Life-like motion driven by artificial molecular machines. *Nat. Rev. Chem.* **3**, 536–551 (2019).
19. Needleman, D. & Dogic, Z. Active matter at the interface between materials science and cell biology. *Nat. Rev. Mater.* **2** (2017).
20. Korn, E., Carlier, M. & Pantaloni, D. Actin polymerization and ATP hydrolysis. *Science* **238**, 638–644 (1987).
21. Desai, A. & Mitchison, T. J. Microtubule polymerization dynamics. *Annu. Rev. Cell Dev. Biol.* **13**, 83–117 (1997).
22. Kohler, S., Schaller, V. & Bausch, A. R. Structure formation in active networks. *Nat. Mater.* **10**, 462–468 (2011).
23. Boekhoven, J. et al. Dissipative self-assembly of a molecular gelator by using a chemical fuel. *Angew. Chem. Int. Ed. Engl.* **49**, 4825–4828 (2010).
24. Boekhoven, J., Hendriksen, W. E., Koper, G. J., Eelkema, R. & van Esch, J. H. Transient assembly of active materials fueled by a chemical reaction. *Science* **349**, 1075–1079 (2015).
25. van Esch, J. H., Klajn, R. & Otto, S. Chemical systems out of equilibrium. *Chem. Soc. Rev.* **46**, 5474–5475 (2017).
26. Saha, B., Chatterjee, A., Reja, A. & Das, D. Condensates of short peptides and ATP for the temporal regulation of cytochrome c activity. *Chem. Commun.* **55**, 14194–14197 (2019).
27. Post, E. A. J. & Fletcher, S. P. Dissipative self-assembly, competition and inhibition in a self-reproducing protocell model. *Chem. Sci.* **11**, 9434–9442 (2020).
28. Deng, J. & Walther, A. Pathway complexity in fuel-driven DNA nanostructures with autonomous reconfiguration of multiple dynamic steady states. *J. Am. Chem. Soc.* **142**, 685–689 (2020).
29. Cardona, M. A. & Prins, L. J. ATP-fuelled self-assembly to regulate chemical reactivity in the time domain. *Chem. Sci.* **11**, 1518–1522 (2020).
30. Hossain, M. M., Atkinson, J. L. & Hartley, C. S. Dissipative assembly of macrocycles comprising multiple transient bonds. *Angew. Chem. Int. Ed. Engl.* **59**, 13807–13813 (2020).
31. Bal, S., Ghosh, C., Ghosh, T., Vijayaraghavan, R. K. & Das, D. Non-equilibrium polymerization of cross-beta amyloid peptides for temporal control of electronic properties. *Angew. Chem. Int. Ed. Engl.* **59**, 13506–13510 (2020).
32. Ragazzon, G. & Prins, L. J. Energy consumption in chemical fuel-driven self-assembly. *Nat. Nanotechnol.* **13**, 882–889 (2018).
33. Astumian, R. D. Kinetic asymmetry allows macromolecular catalysts to drive an information ratchet. *Nat. Commun.* **10**, 3837 (2019).
34. Maiti, S., Fortunati, I., Ferrante, C., Scrimin, P. & Prins, L. J. Dissipative self-assembly of vesicular nanoreactors. *Nat. Chem.* **8**, 725–731 (2016).
35. van Ravensteijn, B. G. P., Hendriksen, W. E., Eelkema, R., van Esch, J. H. & Kegel, W. K. Fuel-mediated transient clustering of colloidal building blocks. *J. Am. Chem. Soc.* **139**, 9763–9766 (2017).
36. Dambenieks, A. K., Vu, P. H. Q. & Fyles, T. M. Dissipative assembly of a membrane transport system. *Chem. Sci.* **5**, 3396–3403 (2014).
37. Ogden, W.A. & Guan, Z. Redox chemical-fueled dissipative self-assembly of active materials. *ChemSystemsChem* https://doi.org/10.1002/syst.201900030 (2019).
38. Leira-Iglesias, J., Sorrenti, A., Sato, A., Dunne, P. A. & Hermans, T. M. Supramolecular pathway selection of perylenediimides mediated by chemical fuels. *Chem. Commun.* **52**, 9009–9012 (2016).
39. Tena-Solsona, M. et al. Non-equilibrium dissipative supramolecular materials with a tunable lifetime. *Nat. Commun.* **8**, 15895 (2017).
40. Kariyawasam, L. S. & Hartley, C. S. Dissipative assembly of aqueous carboxylic acid anhydrides fueled by carbodiimides. *J. Am. Chem. Soc.* **139**, 11949–11955 (2017).

41. Dai, K. et al. Regulating chemically fueled peptide assemblies by molecular design. *J. Am. Chem. Soc.* **142**, 14142–14149 (2020).
42. Riess, B. et al. Dissipative assemblies that inhibit their deactivation. *Soft Matter* **14**, 4852–4859 (2018).
43. Grotsch, R. K. et al. Dissipative self-assembly of photoluminescent silicon nanocrystals. *Angew. Chem. Int. Ed. Engl.* **57**, 14608–14612 (2018).
44. Grotsch, R. K. et al. Pathway dependence in the fuel-driven dissipative self-assembly of nanoparticles. *J. Am. Chem. Soc.* **141**, 9872–9878 (2019).
45. Tena-Solsona, M., Wanzke, C., Riess, B., Bausch, A. R. & Boekhoven, J. Self-selection of dissipative assemblies driven by primitive chemical reaction networks. *Nat. Commun.* **9**, 2044 (2018).
46. Wanzke, C., Tena-Solsona, M., Rieß, B., Tebcharani, L. & Boekhoven, J. Active droplets in a hydrogel release drugs with a constant and tunable rate. *Mater. Horiz.* **7**, 1397–1403 (2020).
47. Donau, C. et al. Active coacervate droplets as a model for membraneless organelles and protocells. *Nat. Commun.* **11**, 5167 (2020).
48. Kriebisch, B. A. K. et al. Reciprocal coupling in chemically fueled assembly: a reaction cycle regulates self-assembly and vice versa. *J. Am. Chem. Soc.* **142**, 20837–20844 (2020).
49. Panja, S., Dietrich, B. & Adams, D. J. Chemically fuelled self-regulating gel-to-gel transition. *ChemSystemsChem* https://doi.org/10.1002/syst.201900038 (2019).
50. Bal, S., Das, K., Ahmed, S. & Das, D. Chemically fueled dissipative self-assembly that exploits cooperative catalysis. *Angew. Chem. Int. Ed. Engl.* **58**, 244–247 (2019).
51. Coin, I., Beyermann, M. & Bienert, M. Solid-phase peptide synthesis: from standard procedures to the synthesis of difficult sequences. *Nat. Protoc.* **2**, 3247–3256 (2007).
52. Chung, B. K. W., White, C. J. & Yudin, A. K. Solid-phase synthesis, cyclization, and site-specific functionalization of aziridine-containing tetrapeptides. *Nat. Protoc.* **12**, 1277–1287 (2017).
53. Murray, J. K. & Gellman, S. H. Parallel synthesis of peptide libraries using microwave irradiation. *Nat. Protoc.* **2**, 624–631 (2007).
54. Sackett, D. L. & Wolff, J. Nile red as a polarity-sensitive fluorescent probe of hydrophobic protein surfaces. *Anal. Biochem.* **167**, 228–234 (1987).
55. Stuart, M. C. A., van de Pas, J. C. & Engberts, J. B. F. N. The use of Nile Red to monitor the aggregation behavior in ternary surfactant-water-organic solvent systems. *J. Phys. Org. Chem.* **18**, 929–934 (2005).
56. Schnitter, F. & Boekhoven, J. A method to quench carbodiimide-fueled self-assembly. *ChemSystemsChem* https://doi.org/10.1002/syst.202000037 (2020).
57. Draper, E. R. & Adams, D. J. Low-molecular-weight gels: the state of the art. *Chem* **3**, 390–410 (2017).
58. Greenspan, P., Mayer, E. P. & Fowler, S. D. Nile red: a selective fluorescent stain for intracellular lipid droplets. *J. Cell Biol.* **100**, 965–973 (1985).
59. Nakajima, N. & Ikada, Y. Mechanism of amide formation by carbodiimide for bioconjugation in aqueous media. *Bioconjug. Chem.* **6**, 123–130 (1995).
60. Goodling, K., Johnson, K., Lefkowitz, L. & Williams, B. W. The modern student laboratory: luminescent characterization of sodium dodecyl sulfate micellar solution properties. *J. Chem. Educ.* **71**, A8 (1994).
61. Brown, P. R. Effect of flow rates and the slope of the linear concentration gradient on peak areas in high pressure liquid chromatography. *J. Chromatogr. A* **57**, 383–390 (1971).

Acknowledgements

This research was conducted within the Max Planck School Matter to Life supported by the German Federal Ministry of Education and Research (BMBF) in collaboration with the Max Planck Society. J.B., F.S., A.M.B., B.W. and O.L. acknowledge funding by the Deutsche Forschungsgemeinschaft (DFG, German Research Foundation) – SFB-863 – Project ID 111166240 (Project B11) and funding by the European Research Council (ERC starting grant 852187). J.R.F. acknowledges the Deutsche Forschungsgemeinschaft for project 411722921. Cryo-TEM measurements were performed using infrastructure contributed by the Dietz Lab and the TUM EM Core Facility. We acknowledge the technical support provided by F. Kohler.

Author contributions

F.S. and A.M.B. contributed equally to this protocol. They designed and performed the experiments and wrote the manuscript. B.W. and J.R.F. carried out the experiments. J.B. designed experiments, outlined and wrote the manuscript, and supervised the project. O.L. designed the experiments.

Competing interests

The authors declare no competing interests.

Additional information

Extended data is available for this paper at https://doi.org/10.1038/s41596-021-00563-9.

Supplementary information The online version contains supplementary material available at https://doi.org/10.1038/s41596-021-00563-9.

Correspondence and requests for materials should be addressed to J.B.

Peer review information *Nature Protocols* thanks Dibyendu Das and the other, anonymous reviewer(s) for their contribution to the peer review of this work.

Reprints and permissions information is available at www.nature.com/reprints.

Publisher's note Springer Nature remains neutral with regard to jurisdictional claims in published maps and institutional affiliations.

Received: 23 October 2020; Accepted: 26 April 2021;
Published online: 30 June 2021

Related links
Key references using this protocol
Tena-Solsona, M. et al. *Nat. Commun.* **8**, 15895 (2017): https://doi.org/10.1038/ncomms15895
Schnitter, F. & Boekhoven, J. *ChemSystemsChem* **3**, e2000037 (2021): https://doi.org/10.1002/syst.202000037
Donau, C. et al. *Nat. Commun.* **11**, 5157 (2020): https://doi.org/10.1038/s41467-020-18815-9
Dai, K. et al. *J. Am. Chem. Soc.* **142**, 33 (2020): https://doi.org/10.1021/jacs.0c04203
Kriebisch, B. A. K. et al. *J. Am. Chem. Soc.* **142**, 49 (2020): https://doi.org/10.1021/jacs.0c10486

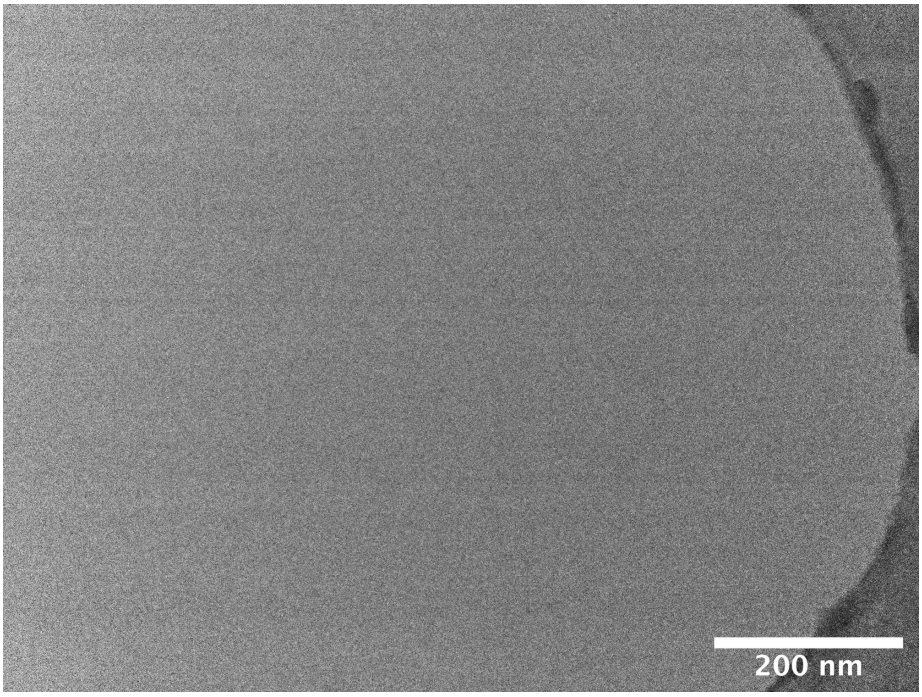

Extended Data Fig. 1 | Cryo-TEM microscope micrograph. The control micrograph of a 10 mM precursor **2** stock solution excludes preassembly of the inactivated precursor in the absence of EDC fuel.

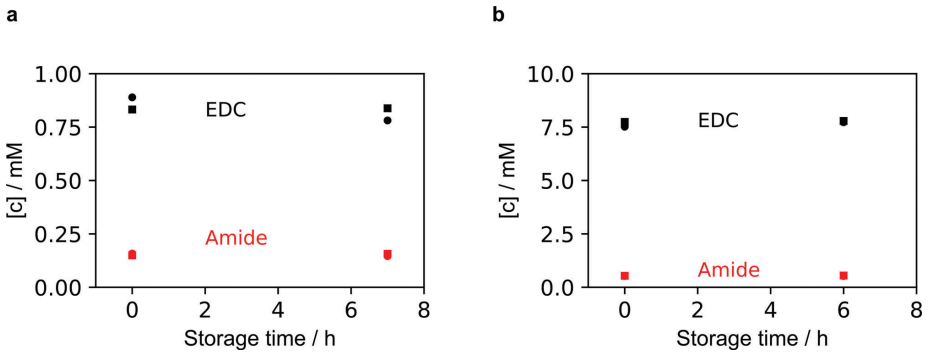

Extended Data Fig. 2 | EDC hydrolysis and Fmoc deprotection kinetics. a,**b**, The addition of the quenching solution freezes the reaction cycle of Fmoc-E-OH (**1**) (**a**) and Fmoc-AAD-OH (**2**) (**b**). In the timescale of the HPLC analysis, the degradation of EDC and Fmoc deprotection does not falsify the concentration determination.

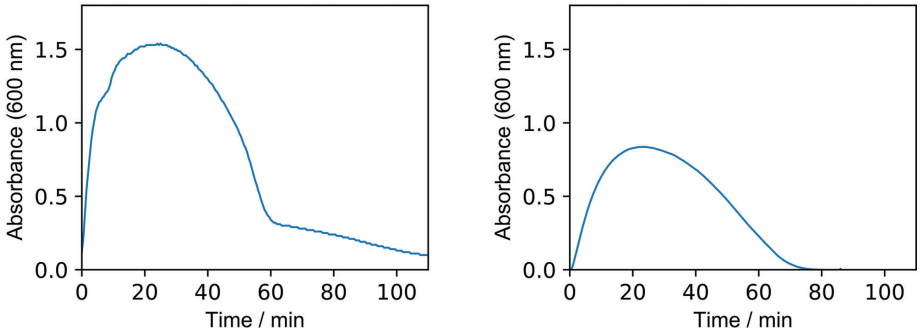

Extended Data Fig. 3 | The absorbance of light as a measure for turbidity. a, Usage of different sample containers affects the measurement quality as sedimentation in a 96-well plate wrongly extends the system's lifetime. **b**, Regarding colloids formed by **1**, a cuvette is a better choice as sample container.

nature research

Corresponding author(s): Job Boekhoven

Last updated by author(s): Mar 18, 2021

Reporting Summary

Nature Research wishes to improve the reproducibility of the work that we publish. This form provides structure for consistency and transparency in reporting. For further information on Nature Research policies, see our Editorial Policies and the Editorial Policy Checklist.

Statistics

For all statistical analyses, confirm that the following items are present in the figure legend, table legend, main text, or Methods section.

n/a	Confirmed	
☐	☒	The exact sample size (*n*) for each experimental group/condition, given as a discrete number and unit of measurement
☐	☒	A statement on whether measurements were taken from distinct samples or whether the same sample was measured repeatedly
☒	☐	The statistical test(s) used AND whether they are one- or two-sided *Only common tests should be described solely by name; describe more complex techniques in the Methods section.*
☒	☐	A description of all covariates tested
☒	☐	A description of any assumptions or corrections, such as tests of normality and adjustment for multiple comparisons
☒	☐	A full description of the statistical parameters including central tendency (e.g. means) or other basic estimates (e.g. regression coefficient) AND variation (e.g. standard deviation) or associated estimates of uncertainty (e.g. confidence intervals)
☒	☐	For null hypothesis testing, the test statistic (e.g. *F*, *t*, *r*) with confidence intervals, effect sizes, degrees of freedom and *P* value noted *Give P values as exact values whenever suitable.*
☒	☐	For Bayesian analysis, information on the choice of priors and Markov chain Monte Carlo settings
☒	☐	For hierarchical and complex designs, identification of the appropriate level for tests and full reporting of outcomes
☒	☐	Estimates of effect sizes (e.g. Cohen's *d*, Pearson's *r*), indicating how they were calculated

Our web collection on statistics for biologists contains articles on many of the points above.

Software and code

Policy information about availability of computer code

Data collection	Standard software was used to obtain the described results. The kinetic model is discussed in previous publications and is provided with GitHub.
Data analysis	Standard software was used to obtain the described results. The kinetic model is discussed in previous publications and is provided with GitHub.

For manuscripts utilizing custom algorithms or software that are central to the research but not yet described in published literature, software must be made available to editors and reviewers. We strongly encourage code deposition in a community repository (e.g. GitHub). See the Nature Research guidelines for submitting code & software for further information.

Data

Policy information about availability of data

All manuscripts must include a data availability statement. This statement should provide the following information, where applicable:

- Accession codes, unique identifiers, or web links for publicly available datasets
- A list of figures that have associated raw data
- A description of any restrictions on data availability

The authors declare that all the data supporting the findings of this study are available within the article, in the source data files and in the Supplementary Information files.

Field-specific reporting

Please select the one below that is the best fit for your research. If you are not sure, read the appropriate sections before making your selection.

☒ Life sciences ☐ Behavioural & social sciences ☐ Ecological, evolutionary & environmental sciences

For a reference copy of the document with all sections, see nature.com/documents/nr-reporting-summary-flat.pdf

Life sciences study design

All studies must disclose on these points even when the disclosure is negative.

Sample size	Experiments were performed at least in triplicates to ensure reproducability.
Data exclusions	Not applicable
Replication	Experiments were performed at least in triplicates to ensure reproducability.
Randomization	Not applicable
Blinding	Not applicable

Reporting for specific materials, systems and methods

We require information from authors about some types of materials, experimental systems and methods used in many studies. Here, indicate whether each material, system or method listed is relevant to your study. If you are not sure if a list item applies to your research, read the appropriate section before selecting a response.

Materials & experimental systems

n/a	Involved in the study
☒	☐ Antibodies
☒	☐ Eukaryotic cell lines
☒	☐ Palaeontology and archaeology
☒	☐ Animals and other organisms
☒	☐ Human research participants
☒	☐ Clinical data
☒	☐ Dual use research of concern

Methods

n/a	Involved in the study
☒	☐ ChIP-seq
☒	☐ Flow cytometry
☒	☐ MRI-based neuroimaging

7 Multiple steady states: Bistability

The experiments I have discussed in the previous chapters were performed in "batch mode". A finite amount (batch) of fuel was added to the precursor solution which drives the reaction cycle for a finite amount of time. As fuel has been consumed, the activation reaction's rate drops to zero and the deactivation reaction converts the remaining product into the precursor. By continuously adding fuel, a steady state arises in which activation equals deactivation and thus with constant product concentrations. It should be noted that this remains a non-equilibrium situation, i.e., a steady state should not be confused with an equilibrium. The population of activated product is stable, but constantly being maintained by the activation and deactivation. Only, upon the constant dissipation of energy, can that situation be sustained. The creation of cellular memory as described in the introduction of this thesis requires the existence of multiple stable steady states under one energy influx. If at least two stable states exist in a reaction cycle, for example an off-state and an on-state, the system is bistable and thus could exhibit memory. The question is now, how can one energy influx result in two stable states?

7.1 Transcriptional feedback circuits

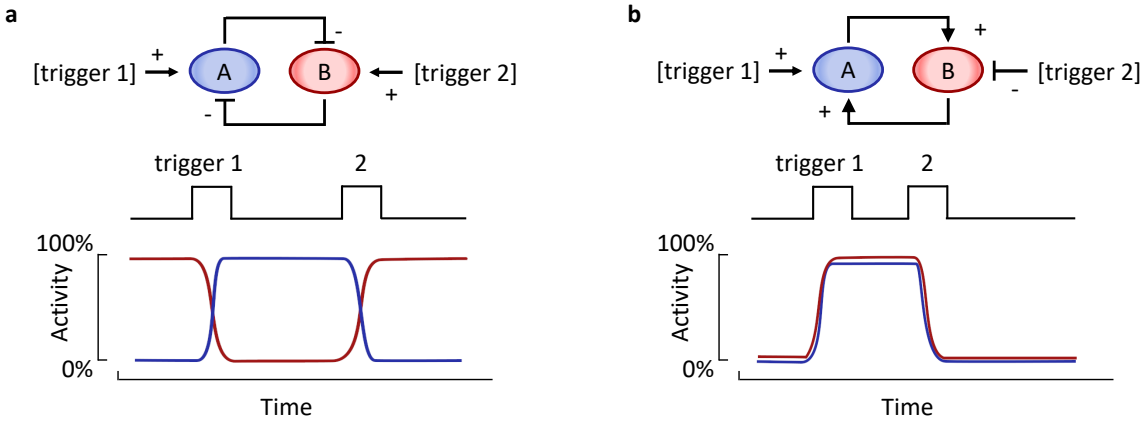

Figure 5: Transcriptional feedback loops. Schematic representation of how a sustained response is attained from transient signals.[66] **a** A double negative feedback loop can be switched between the two stable states, expressing either A or B. **b** A positive feedback loop in which gene expression of both A and B are either switched on or off. Adapted by permission from Elsevier, Copyright © 2002.

Bistability in a biological context was first shown by the coexistence of multiple stable steady states in a genetic regulatory network.[67] It was proposed that a distinct state can be preserved by feedback circuits as exhibited by, for example, double-negative feedback (Fig. 5 a). Suppose that there are two gene products, A and B, each of which inhibits the other's transcription. Such a system could have a stable state with A on and B off, or an alternative stable state with A off and B on. Once either state has been established, it could persist indefinitely, until some trigger forces the system to the other state. As an example, such a double-negative feedback mechanism controls the different virulent states of the already mentioned lambda phage.[68–70] Sustained gene expression could also be achieved through positive feedback (Fig. 5 b). In such case, the system would toggle between a state with both A and B off and a state with both A and B on.[71–73] Yet, the presence of some sort of feedback, positive feedback, double-negative feedback, or autocatalysis, is not sufficient to create a satisfactory bistable signaling circuit. Regarding the two states of the positive feedback circle, which is an off and an on-state, the off-state would become unstable

by small fluctuations of trigger 1 or if A has any initial activity. As a result, the system would continually shift towards the on-state and thus being monostable.

7.2 Making the off-state stable

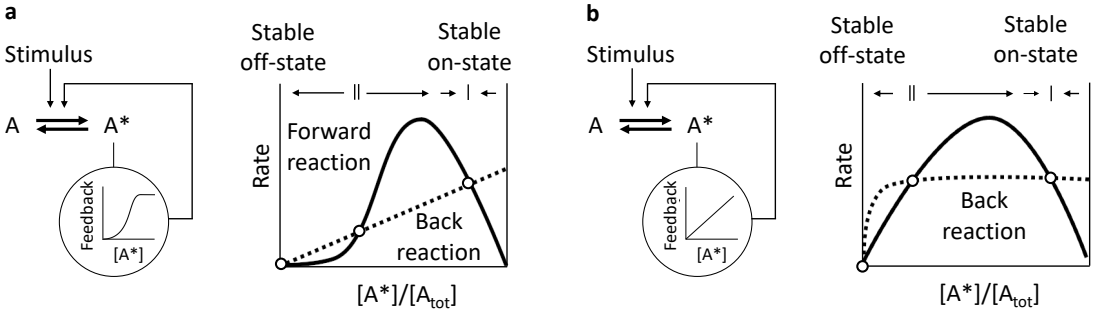

Figure 6: Schematic representation of how the concepts of ultrasensitivity and back reaction saturation conserve a stable off-state.[74] **a** Ultrasensitivity requires a sigmoid like feedback strength. For simplicity it is assumed that the influence of feedback is strong, and the basal reaction rate is zero. Therefore, the rate of forward reaction increases with an initial delay. After reaching a maximum, the rate decreases because of lowered substrate concentrations. The rate of the backward reaction rises with the amount of formed product A*. **b** Regarding the concept of back reaction saturation, a linear feedback strength is assumed, resulting in forward reaction rates in the form of an inverted parabola. The back reaction increases linearly and saturates at high product concentrations. Adapted by permission from AIP Publishing, Copyright © 2001.

The subsequent approach to describe the kinetics of bistable states is mainly derived from the work of J. E. Ferrell, et al.[74] There are two easy ways to modify the system to make both the on- and off-state stable. The first possibility would be a non-linear feedback response. Assuming a reaction network in which product A* is formed from A, catalyzed by a stimulus, and A* degrades to initial A via a second reaction pathway (Fig. 6 a). An exemplary reaction cycle could be the reversible phosphorylation catalyzed by kinases and phosphatases.[75–77] The reaction rate of the back reaction should follow classical Michaelis-Menten kinetics, that means low rates at the beginning and a linear increase towards high rates at high A* concentrations. The formation reaction should be autocatalytic, which means that product A* accelerates its own formation. To avoid transitions from off to on by small fluctuations, the strength of the feedback should increase with A* in a non-linear way. Feedback strength dependency in form of a sigmoid curve could be achieved by a mechanism called cooperativity.[78–81] In cooperative enzymes, reaction kinetics are sped up by increasing substrate affinity when an increased amount of substrate is bound to the enzyme. In the case of hemoglobin, a cooperative enzyme, the binding site's affinity towards oxygen is increased when one of the four binding sites is already occupied.[82] There are further mechanisms which invoke such feedback behavior which do not rely on cooperativity. As such, the product A* could both activate its forming enzyme and inhibit an inhibitor of the same enzyme.[83] Therefore, the more general term ultrasensitivity has been introduced.[84] Taken together, ultrasensitive responses generate rates which proceed slowly at the beginning and increase exponentially until saturation is reached. Combining the rates of forward and back reaction in so called rate balance plots, three steady state intersections become apparent. Two of those sections are stable as small perturbations in any direction would be pushed back towards equilibrium. Thereby, the off-state gets stable until a threshold at the middle intersection point is reached. That point is unstable as any perturbation would drive the system towards the stable states. A second mechanism to filter out noise would be saturating the back reaction as more and more A* is produced (Fig. 6 b). The rate balance plot

demonstrates such a scenario, in which the back reaction rate rises more steeply than the feedback but then levels off due to saturation. The linear feedback instead keeps rising and intersects the back reaction creating the unstable state. Again, three steady states can be found, two stable ones and one unstable in between.[85]

7.3 Switching between states and the hysteresis effect

So far, switching between the stable states could be achieved by perturbations beyond threshold concentrations. Another handle which has been neglected is the initial activity of the enzyme catalyzing the formation of A*. The initial rate of the forward reaction can be varied by adding an input stimulus. Incrementally increasing that feedback-independent stimulus lifts the forward reaction curve upwards until only one intersection with the back reaction curve remains (Fig. 7 a). Now, the off-state and the threshold no longer exist. The only possible steady state is the on-state which the system will turn to. The point where the system switches between three and one steady states is called bifurcation point.[86] When lowering the stimulus again, the off-state will reappear, but there will not be any driving force for the system to leave the current on-state. Thus, the resulting stimulus-response curve when increasing the stimulus differs from the curve decreasing the stimulus. The steady state in which the system resides depends on the history of the sample which is described by so called hysteresis curves (Fig. 7 b).[87] Irreversible switching as it is described is crucial for biochemical memory such as cell differentiation or the irreversible entry into the several stages of cell division.[88,89] To switch the system off again, a super-threshold perturbation would be needed or alternatively the feedback could be broken by auto-inactivating loops. Thereby a non-permanent response can be attained.

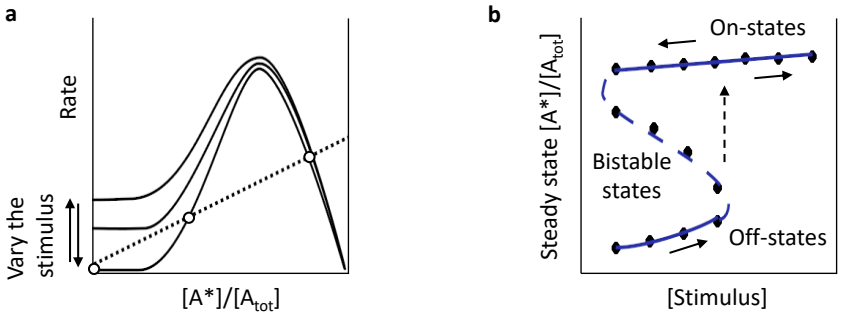

Figure 7: Schematic representation of switching between states without perturbation. **a** The forward reaction's rate curve shifts by changing the initial stimulus. At a high stimulus, only one intersection with the back reaction exists. **b** The resulting intersections from a plotted against the feedback strength. A bistable regime exists for forward reaction curves intersecting the back reaction three times. At a high initial stimulus, only one stable on-state can be found.

7.4 Oscillations

In an oscillation system, a reaction network switches between states in a defined rhythm. Oscillations can be realized by coupling bistable switches to relatively slow, time-delayed negative feedback loops.[90] Given the many feedback processes taking place in regulating cell processes, oscillations are tightly associated with life. Originally, rhythmicity was linked to the temporal recurring of a property. Timescales range from seconds over days to years.[67,91] The fastest periods are observed in electrically excitable cells such as neurons, or cardiac and other muscle cells. For example, the flight muscles of insect wings can oscillate as fast as 1000 beats per second.[92] The mechanism involves positive feedback loops in voltage-dependent membranes. To make the

on-state transitory, an auto-inactivating mechanism is encoded which breaks the feedback and resets the system to its initial off-state. The circadian rhythm by comparison has a periodicity of one day and regulates the wake-sleep cycle.[93,94] It allows organisms to adapt to day night cycles and downregulates cellular processes when resources are scarce. Period cycles of years have been observed in the recurrence of infections like influenza or animal reproduction.[91] Compared to the time resolution of functionality, oscillations can also occur spatially. Inhomogeneities driven by reaction diffusion mechanisms can create complex patterns as observed in the skin of animals.[95]

8 Synthetic feedback mechanisms

In line with "What I cannot create, I do not understand" as stated by Richard Feynman,[96] effort has been made to create synthetic counterparts of feedback processes. Interesting systems have been built making use of autocatalytic enzymes such as trypsin[90,97] or using gene regulatory networks.[98,99] In the following, selected examples are reviewed which showed bistable behavior without the help of evolved cellular machinery.

8.1 Autocatalysis by up-concentration

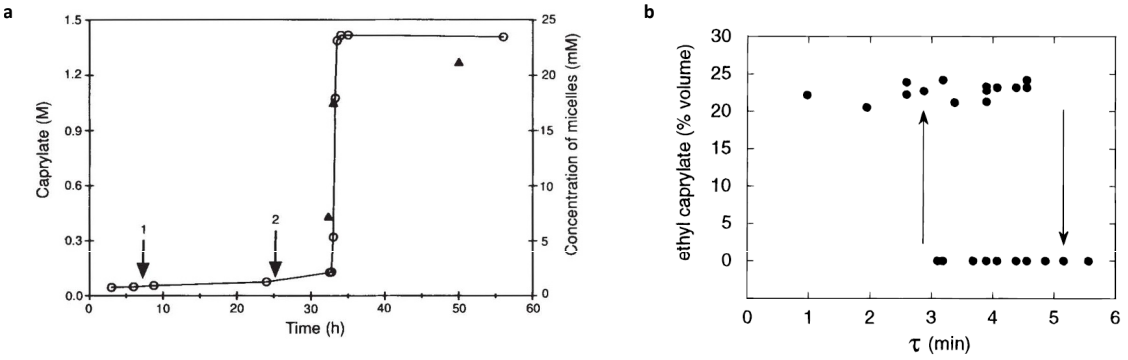

Figure 8: Self-replicating micelles in- and out-of-equilibrium. **a** The concentration of formed caprylate over time. The autocatalytic reaction shows a typical sigmoid curve shape.[100] **b** The concentration of the reactant ethyl caprylate as a function of the applied residence time τ. A bistable regime exists in which the ethyl caprylate concentration depends on past ethyl caprylate concentrations.[101] Reprinted by permission of Springer Nature and American Chemical Society, Copyright © 1992 and 1997.

One of the first self-generating model system was reported by Luisi and coworkers.[100] In their studies, the precursor molecule ethylcaprylate was gently stirred in an aqueous NaOH solution. Being immiscible, slow ethylcaprylate hydrolysis to the amphiphile caprylate takes place at the water-oil interface. The product caprylate concentration remained at low levels until a critical concentration is reached at around 100 mM (Fig. 8 a). At that threshold concentration, the emergence of micelles was observed which solubilized the ethylcaprylate and as a result the supernatant phase disappeared. By titration the authors quantified the precursor concentration inside the micelles. On average, each micelle incorporated five ethylcaprylate molecules. That physical up concentration increased the reaction rate and an exponential increase in caprylate concentrations was observed. As such, the product exerted positive feedback upon its own formation. After a while, the hydrolysis reaction reaches equilibrium, which is expressed by a single phase at high caprylate concentrations. By continuously adding and removing material, systems can be prevented from reaching equilibrium conditions. In other words, equilibrium systems can be adopted to far from

equilibrium conditions. Micheau and co-workers pushed the above-described self-replicating micelles out of equilibrium.[101] They continuously fed a reactor with ethylcaprylate and NaOH and simultaneously removed parts of the reaction mixture. By variation of the flowrates, the time reactants stay inside the reaction chamber can be controlled. That time is expressed by the so-called residence time τ. At low residence times, a two-phase system with high ethylcaprylate educt concentrations was observed (Fig. 8 b). When the reactants stayed in the chamber for longer times by decreasing flow rates, a single phase appeared. The autocatalytic reaction takes over and leads to micelle formation, solubilizing ethyl caprylate and speeding up the reaction rate. Interestingly, for intermediate residence times, either situation may be attained. Both, a single phase or two phases were obtained depending on the initial conditions in the reactor. Another possibility to drive such an autocatalytic reaction away from equilibrium was explored by Fletcher and co-workers.[102] In addition to the autocatalytic micelle formation, a second catabolic reaction was introduced which degraded the micellar building block. By regenerating one part of the building block, the authors showed persistent steady states as long as chemical fuel was present.

8.2 Autocatalysis by a reaction network

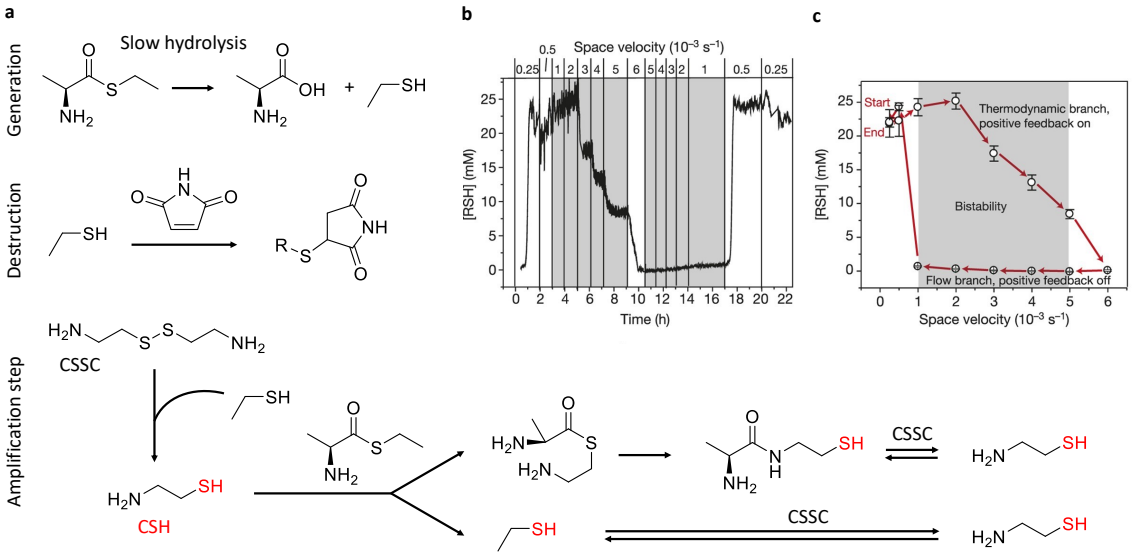

Figure 9: Bistability and hysteresis in an autocatalytic reaction network.[103] **a** The reaction network can be split up in three main processes. In the generation reaction, an ethanethiol trigger molecule is formed from a hydrolysis reaction. Destruction of the autocatalytic reaction network takes place by removing free thiols by maleimide. The amplification step yields two CSH molecules from one molecule CSH. **b** The concentration of formed thiols over time when stepwise increasing and decreasing space velocities. **c** The concentration of free thiols as a function of the applied space velocity. In a bistable regime, the free thiol concentration depends on the history of the sample. Adapted with permission from Springer Nature, Copyright © 2016.

The autocatalytic system described in the following relies on a reaction network that displays bistability in the concentrations of organic thiols and amides.[103] Starting components of the network are L-alanine ethyl thioester (AlaSEt) and cystamine (CSSC) (Fig. 9 a). The former slowly hydrolyses and thereby generates ethanethiol. Ethanethiol then reacts with CSSC, yielding the thiol CSH which is amplified by the following steps. In the first step thiolate-thioester exchange takes place of CSH with L-alanine ethyl thioester, releasing an ethanethiol molecule. The formed thioester rearranges intramolecularly, generating a free thiol group. Both thiols then react in a second step with CSSC, yielding two molecules of CSH. Because one molecule CSH generates two

molecules of CSH, the thiol formation proceeds autocatalytically. Fist, the reactions were tested in a batch reactor. The autocatalytic network was proven by monitoring the concentrations of the network's compounds over time by NMR. Both, the concentration profiles of the amide and thiol compounds showed sigmoid shaped curves. Those curves are typical for autocatalytic reactions, which start slowly at the beginning but speed up as more product is formed. The second design element is the introduction of a reaction, which delays the start of the autocatalytic network. In this destruction reaction, maleimide rapidly removes free thiols. This reaction is extremely fast compared to all other rates and thereby postpones the autocatalytic network reaction until it has been completely consumed. The authors tested the system in a continuously stirred tank reactor and controlled the residence time of the compounds inside the reaction chamber by variating the flow rates. Low flowrates result in high residence times or low space velocities. Space velocity is defined as the amount of material replaced in a given time interval. The reactor was fed with AlaSEt, CSSC and the deactivator maleimide. A hysteresis curve emerged when first ramping up to high flow rates and then returning to low flow rates (Fig. 9 b, c). At low space velocities, a high thiol concentration was measured indicating the predominance of the autocatalytic reaction network. At high space velocities, which means high flow rates, low thiol concentrations were measured. The high influx of the deactivator maleimide prevented autocatalysis from taking place. In a bistable regime, two possible states were found. In that regime, the thiol concentration was dependent on whether the system started from low or high thiol concentrations.

8.3 Templation and negative feedback

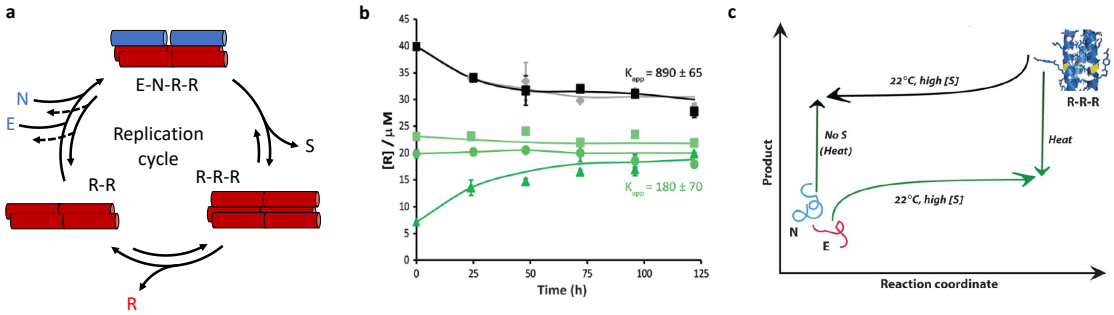

Figure 10: Bistability in product distribution driven by templation and negative feedback.[104] **a** The chemical reaction cycle. Peptide R is formed from precursors E and N by thiol-thioester exchange reactions. **b** Bistable states are observed in the resting concentrations of peptide R. **c** Schematic outline of switching between high and low stable states. Adapted with permission from John Wiley and Sons, Copyright © 2015.

The dynamic system described in this section relies on the reversible formation of a thioester peptide (Fig. 10 a).[104,105] The thioester peptide (R) forms from a shorter thioester (E) and a thiol-terminated peptide (N). Upon that thiol-thioester exchange reaction, a small thiol molecule (S) is released. Peptide R self-assembles into trimeric coiled-coil structures and serves as a template for the ligation of E and N. Furthermore, the folded structure increases its stability against the attack of thiols (S), thereby slowing down decomposition rates. Bistability is expressed in two stable resting states (Fig. 10 b). Depending on initial peptide R concentrations, two distinct steady state concentration distributions are obtained. The distributions are calculated from the equilibrium constant of the reversible reaction network. Starting from equal total material concentrations (E + R = 40 µM), the system rests in a high steady state when starting with high R concentrations (K_{app} = 890). A low steady state (K_{app} = 180) is reached starting from low R concentrations.

Additionally, the authors outlined the possibility of switching the system between the two states by external energy supply (Fig. 10 c). Experiments have shown that equilibration at higher temperatures (37 °C) leads to lower steady states in product distribution. Thereby a high-to-low steady state switch could be created. A reaction mixture with initial high R concentration was reacted for 40 h at 37 °C. Afterwards, the system was re-equilibrated at room temperature. In comparison to the previous experiments, the system now ended up in a low steady state although starting with high R concentrations. The low-to-high switch was chemically achieved. Precursor molecules E and N were reacted at low starting concentrations of R in the absence of the small thiol molecule S. As a result, high steady state concentration distributions were reached, even after equilibrating the resulting mixture with excess of S.

8.4 Oscillations from a perylene diimide reaction network

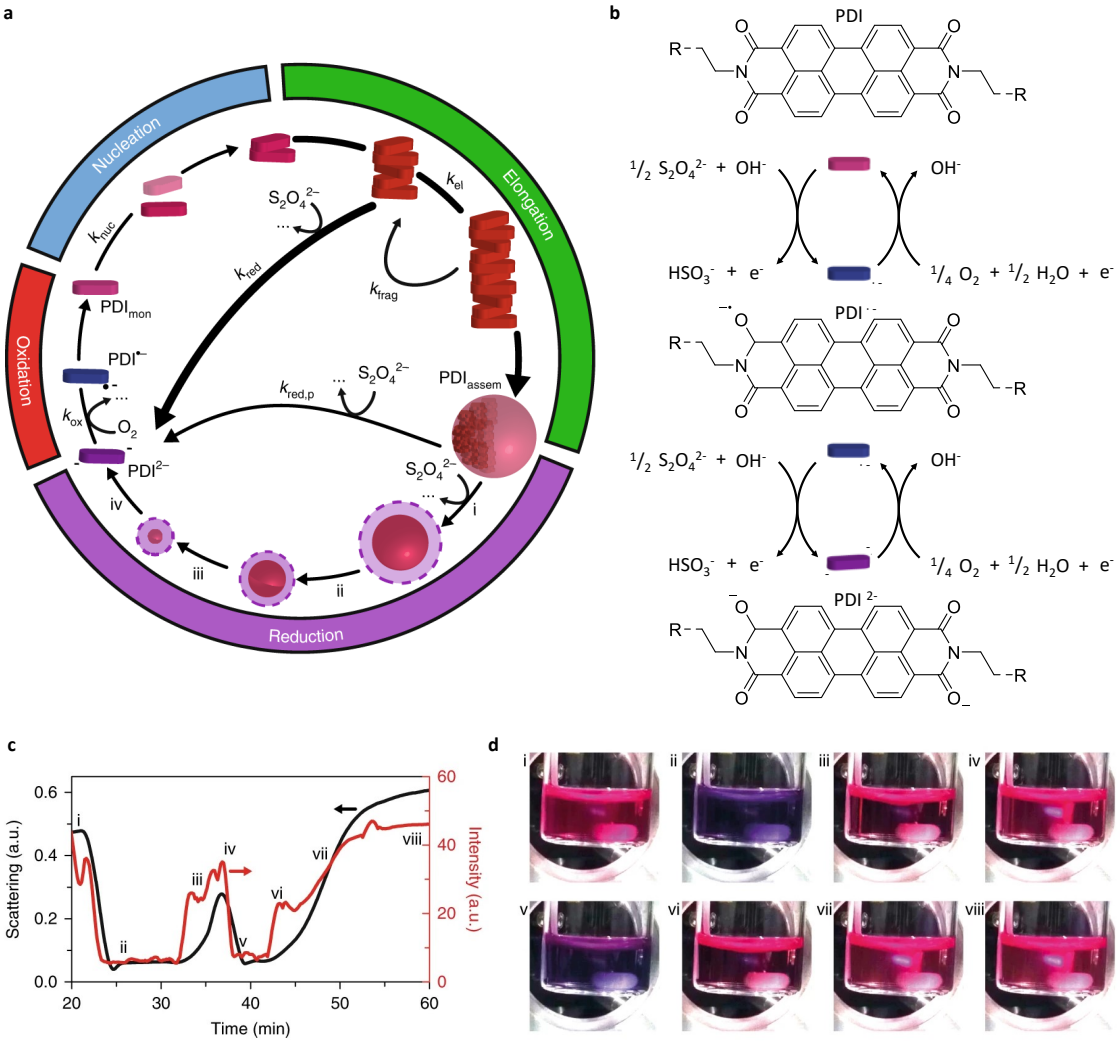

Figure 11: The chemical reaction cycle of periodically reducing and oxidizing perylene diimide.[106] **a** In the oxidized form, the building blocks nucleate and grow larger structures. A reduction reaction reverts the original building block and induces disassembly. **b** The molecular structures of the stepwise reduction and oxidation of perylene diimide. **c** The oscillations of PDI assembly and disassembly resulted in periodic changes in scattering and absorption intensity. **d** Time-lapse photographs show the periodic color change of the reaction solution. Adapted with permission from Springer Nature, Copyright © 2018.

Many oscillating systems have been published by linking self-assembly to known oscillators like the Belousov-Zhabotinsky catalyst or pushing autocatalytic reactions out of equilibrium by continuously stirred tank reactors. In contrast, the species described in this work is capable to self-assemble and also provides non-linearities regarding activation and deactivation.[106] As such, oscillations arise from the reversible oxidation and reduction of perylene diimide (PDI, Fig. 11 a, b). The reduced form of perylene diimide (PDI^{2-}) is mostly monomeric, given the repulsion of negatively charged molecules. Oxidation by air oxygen stepwise removes the negative charges, yielding neutral PDI. The uncharged PDI then undergoes supramolecular polymerization, forming colloidal assemblies. Those assemblies exert positive feedback via a nucleation-elongation-fragmentation mechanism. The positive feedback was proven by showing sigmoidal increase in product formation when conducting seeding experiments or applying different stirring rates. The latter experiment showed fastest growth rates at highest stirring rates. The PDI could be reduced back to PDI^{2-} by addition of $Na_2S_2O_4$. A time delay was observed in that reduction reaction. This delay could be attributed to negative feedback exerted by the assembled structures. In a two-step process, the PDI^{2-} concentration raises exponentially as $Na_2S_2O_4$ reacts with the outer shell of the assemblies. Afterwards a slower, sigmoidal increase was measured as surface erosion of the colloids takes place. The resulting oscillations could be tracked by both turbidity measurements and by following the red channel of a CCD-camera (Figure 11 c). Starting from assembled PDI, which appears as a pink colored solution, the intensity of scattered light decreases when reduction and disassembly takes place. The pink color transfers to a violet one (Fig. 11 d). Upon oxidation and self-assembly, light scattering increases and the pink color is reverted. Addition of the reductant $Na_2S_2O_4$ in semi-batch mode resulted in damped oscillations over the time course of around 250 minutes.

8.5 Synthetic memory through the Belousov-Zhabotinsky reaction

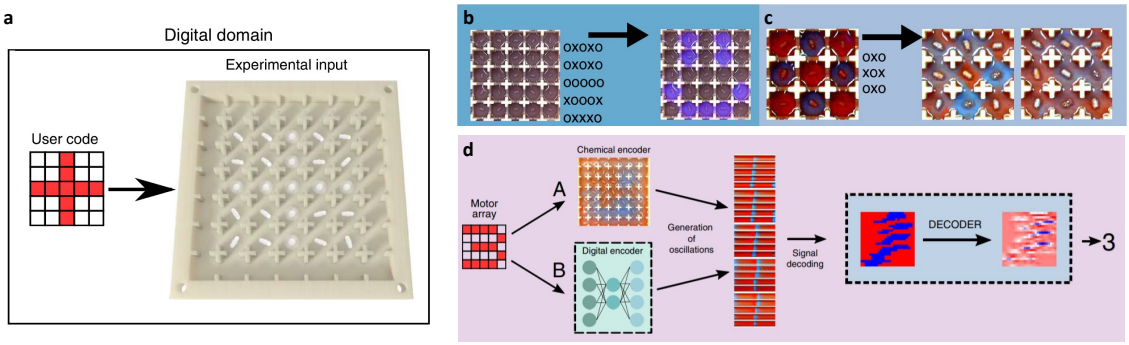

Figure 12: Memory storage through the BZ-reaction.[107] **a** 3D printing an array of reaction chambers. **b** Each chamber can be referred to a pixel in a pixel display and thereby patterns could be drawn. **c** The time evolution of a global oscillating pattern as chambers communicate with each other. **d** Schematic representation of encoding and decoding a global oscillation pattern. Adapted with permission from Springer Nature, Copyright © 2020.

The excitability and bistability of oscillations can be used to set up chemical computers. Cronin and co-workers designed an automated platform in which the Belousov-Zhabotinsky (BZ) reaction performed different processing tasks, such as volatile memory and pattern recognition.[107] The BZ reaction consisted of sulfuric acid, malonic acid, potassium bromate and the indicator ferroin. Oscillations stem from ferroin being reversibly oxidized and reduced. When stirring, oscillations can be excited and a frequent color change from red (reduced form) to blue (oxidized form) is observed. These oscillations get chaotic and fade out when stirring is stopped. As a result, the

color of the reaction mixture remains red. By constructing a grid of stirred chambers, the authors created programmable, volatile memory (Fig. 12 a). Each chamber could be addressed by stirring or not stirring and the platform behaved like a display screen (Fig. 12 b). By fully opening the connections between the chambers, oscillations propagate and form a globally oscillating pattern (Fig. 12 c). The authors trained a neural network to link such a global oscillation pattern to the given inputs and could thereby decode the visible patterns in 90% accuracy (Fig. 12 d).

9 Outlook - Synthetic feedback mechanisms

To encode bistable behavior in supramolecular assemblies which lack feedback mechanisms, the self-assembling species can be coupled to chemical oscillators.[108–115] A drawback of this design strategy is that these oscillators contain many reactants which are often incompatible with additional species like the self-assembling building blocks. The Belousov-Zhabotinsky reaction e.g., involves at least five reactants and the reactions taking place are very complex. Its reaction cascade is thought to involve around 18 different steps.[116,117] In comparison, feedback effects from the supramolecular structures are predominantly of positive nature like physical up-concentration. These, often autocatalytic reactions, end up at thermodynamic equilibrium. Therefore, further tools are needed to decrease product concentrations such as continuous removal of the reaction mixture or additional destruction reactions. Although negative feedback mechanisms would already provide non-linear reaction kinetics plus a destruction pathway, only few examples have been reported yet. Nevertheless, such a reduced and simplified mechanism to create non-linearities would provide a concept of how information could have been stored and processed in a prebiotic world. Furthermore, negative feedback mechanisms could in principle remove the obstacles of flow reactors, which are often fundamental to bistable behavior. Bistable functionality could now be transferred from the macroscopic reaction chamber to the much smaller single supramolecular structure level.

10 Memory, switches, and an OR-port through bistability in chemically fueled crystals

Abstract.

Chemical memory can be stored by at least two distinct states expressed in bistable systems. Storage and switching between the states are crucial to regulate dynamic, life-like processes. The underlying principle of bistability, which is the creation of some sort of feedback, has mainly been demonstrated by positive feedback mechanisms. Reported negative feedback mechanisms are rare. In this work, volatile memory is created by the self-assembly of crystals. The self-assembly is regulated by a carbodiimide driven reaction cycle and the formed crystals exert negative feedback upon the reaction kinetics. By drastically slowing down the deactivation reaction, the crystalline state is maintained. This negative feedback, together with a phase diagram of the crystallization process, is the basis for bistability in this work. The memory is stored in binary on- and off-states, which are equivalent to crystals being present or not. It is demonstrated that the two states can be stored indefinitely long in a flow reactor. At certain setup parameters, both monostable and bistable states could be obtained. Within a bistable window, either a stable on- or a stable off-state emerged, depending on the history of the sample. Varying temperatures or flowrates changed the bistable window's shape of the hysteresis curve. Interestingly, bistability was also observed in semi-batch mode, a condition at zero outflow rate, which would even make flow reactors obsolete. Various triggers have been used to toggle the bistable state. By applying threshold perturbations, the system could be reversibly switched on and off. The switching was used to repeatedly turn on and off several reactors, which were arranged in a 3x3 array. Thereby, patterns could be drawn and stored like in pixel displays. Finally, the ability to process information was demonstrated by creating a Boolean OR-port. The outflow of two reactors served as input of a third output reactor. Similar to the interplay of reaction networks separated by space as observed in biology, a downstream state could be affected by the states of two upstream states.

This work has been published:

Title:	Memory, switches, and an OR-port through bistability in chemically fueled crystals
Authors:	Fabian Schnitter, Benedikt Rieß, Christian Jandl, Job Boekhoven
First published:	20. May 2022
Journal:	Nat Commun
Publisher:	Nature Publishing Group
DOI:	https://doi.org/10.1038/s41467-022-30424-2

This section states the individual work of each author in the publication below. F. Schnitter designed and conducted all experiments. B. Rieß assembled the turbidity device and wrote the associated script. C. Jandl conducted the single crystal x-ray diffraction experiment and evaluated the crystal structural data. J. Boekhoven and F. Schnitter outlined and wrote the manuscript. The work was performed under the supervision and guidance of J. Boekhoven.

nature COMMUNICATIONS

ARTICLE

https://doi.org/10.1038/s41467-022-30424-2 OPEN

Memory, switches, and an OR-port through bistability in chemically fueled crystals

Fabian Schnitter[1], Benedikt Rieß[1], Christian Jandl[2] & Job Boekhoven[1,3]✉

The ability to store information in chemical reaction networks is essential for the complex behavior we associate with life. In biology, cellular memory is regulated through transcriptional states that are bistable, i.e., a state that can either be on or off and can be flipped from one to another through a transient signal. Such memory circuits have been realized synthetically through the rewiring of genetic systems in vivo or through the rational design of reaction networks based on DNA and highly evolved enzymes in vitro. Completely bottom-up analogs based on small molecules are rare and hard to design and thus represent a challenge for systems chemistry. In this work, we show that bistability can be designed from a simple non-equilibrium reaction cycle that is coupled to crystallization. The crystals exert the necessary feedback on the reaction cycle required for the bistability resulting in an on-state with assemblies and an off-state without. Each state represents volatile memory that can be stored in continuously stirred tank reactors indefinitely even though molecules are turned over on a minute-timescale. We showcase the system's abilities by creating a matrix display that can store images and by creating an OR-gate by coupling several switches together.

[1] Department of Chemistry, Technical University of Munich, Lichtenbergstrasse 4, 85748 Garching, Germany. [2] Catalysis Research Centre, Technical University of Munich, Lichtenbergstrasse 4, 85748 Garching, Germany. [3] Institute for Advanced Study, Technical University of Munich, Lichtenbergstrasse 2a, 85748 Garching, Germany. ✉email: job.boekhoven@tum.de

An outstanding goal for the field of systems chemistry is the ability to record information of events that occurred in the past in chemical reaction networks, i.e., networks that can store memory[1–5]. In biology, such volatile memory is stored in transcriptional states that are bistable, i.e., a gene is either expressed or not and can be switched from one to another through a transient signal[6,7]. Because most molecules in the cell are constantly degraded and resynthesized (i.e., turned over), this form of memory is dynamic, i.e., the molecules involved are continuously sustained in a steady state[6]. Synthetic counterparts of cellular memory have been realized through the rewiring of genetic systems in vivo or through the rational design of reaction networks based on DNA and highly evolved enzymes in vitro[8–13]. These networks rely on autocatalytic chemical reaction systems, i.e., reactions in which the product accelerates its own production. These autocatalytic reactions in biological systems rely on highly evolved enzymes. Non-enzymatic reaction networks that display bistability also exist but rely on autocatalytic reactions, which are rare and hard to design[14–24]. Thus, designing more generalizable methods of creating bistability would be a milestone towards autonomous, evolving systems that can store memory of past events.

Here, we show such a minimal design of memory based on bistability in a chemical reaction cycle without autocatalysis. The chemically fueled reaction cycle activates and deactivates molecules for self-assembly giving rise to chemically fueled crystals. Through a previously observed mechanism[25,26], these crystals exert feedback on their reaction cycle which affects steady state levels. The result is that two possible, stable states can emerge in a continuously fueled reactor, i.e., one with and one without crystals. Even though in such a reactor, all components are turned over on a minute-timescale, each state is indefinitely stable. Moreover, the states can be rapidly switched by transient signals. We combined nine reactors to create a nine-pixel display. Moreover, we connected reactors to use them as switches in an OR-gate. Miniaturization and multiple reaction cycles should give rise to evolvable, complex behavior in future work.

Results

The design of the bistability is based on a combination of two mechanisms, i.e., chemically fueled crystals that exert feedback on their reaction cycle (Fig. 1a, b) and a phase diagram of those crystals that contains a metastable zone, i.e., a zone where crystals can be present or not, depending on the history of the sample (Fig. 1c)[27]. The chemically fueled crystals are formed by a reaction cycle that has been explored by our group and others[28–33]. N-Boc-protected aspartic acid (precursor **1**) is activated by reacting with fuel (1-ethyl-3-(3-dimethylaminopropyl) carbodiimide, EDC) to form its corresponding anhydride (product, Fig. 1a, Supplementary Fig. 1). The anhydride product is transient with a half-life of roughly 35 seconds at 24 °C before it spontaneously hydrolyzes to the precursor (Supplementary Fig. 2a, b), i.e., the deactivation reaction. When fuel and precursor are supplied continuously, a steady state emerges in which the product is activated and deactivated at equal rates (vide infra).

We first determined that phase diagram of the crystallization by using a solution of 100 mM precursor in 200 mM MES buffer at pH 3.5. We added fuel to initiate product formation, and we found that the anhydride product can nucleate to form crystals (crystal structure data is listed in the Supplementary Information) above a supersaturation concentration of 16 mM at 24 °C, i.e., $S_{sat} = 16.0$ mM (Fig. 1c). Vice versa, the crystals dissolve when the concentration product falls below a 7.9 mM ($S_{out} = 7.9$ mM). The concentration range between the S_{out} and S_{sat} is referred to as the metastable zone in the Ostwald-Miers diagram for a solute/solvent system[34]. A solution with a concentration of product in this metastable zone can contain crystals or not depending on whether the concentration of the sample was at some point in the recent history above S_{sat}. For example, when 20 mM of EDC is added to 100 mM precursor, a maximum of 12 mM product emerges at the expense of fuel and then decays as fuel is running low (Supplementary Fig. 3). Thus, the system does not reach the S_{sat} and no crystals are observed. Instead, when 60 mM EDC is added, 44 mM product is activated, and crystals are present. When the concentration falls below S_{out} because the system runs low on fuel, the crystals dissolve (Supplementary Fig. 3). A solution that can be sustained within the metastable window, for example, by continuously fueling, could either have crystals or not. However, neither state would be stable indefinitely, as minor fluctuations could result in crystal growth or dissolution.

Thus, a second important feature of the bistability we found is that crystals exert feedback on their reaction cycle. The anhydride in the crystals is protected from hydrolysis because no water can reach the anhydride within the crystal (Fig. 1b). Only the anhydride that remains in the solution can be hydrolyzed, which is equal to the anhydride's solubility (S_{out}). Therefore, the presence of crystals severely slows down the overall deactivation rate, resulting in the accumulation of product, and it raises the product concentration outside of the metastable window. The product's self-protection mechanism is effectively a feedback mechanism. Excitingly, the feedback relies on a phase separation mechanism and is, due to its rudimentary nature, frequently observed in

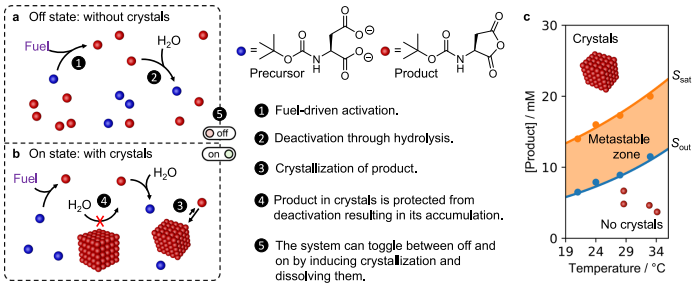

Fig. 1 Mechanisms for bistability in chemically fueled crystals. Two possible states can emerge in one experiment either an (**a**), off-state without crystals or (**b**), an on-state with crystals. The crystals protect the anhydride from deactivation which serves as the feedback mechanism. **c** The phase diagram of crystallization of the product. In the metastable window, a solution with or without crystals can exist. Solubility and supersaturation concentrations at various temperatures were experimentally determined (see Supplementary Methods section and Supplementary Fig. 18).

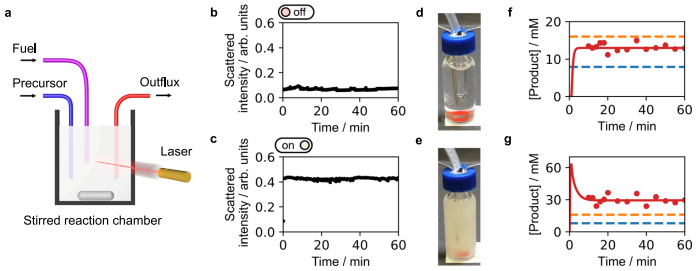

Fig. 2 Chemically fueled assemblies that exert feedback result in bistability. a A schematic representation of our experimental setup to keep the product in a steady state concentration. Precursor and fuel are added continuously to a stirred reaction chamber and all the reaction cycle's components are removed by an outflux. **b**, **d** and **f** The off-state was created when a 1.5 ml reactor was supplied with 25 mM.min^{-1} EDC and 30 mM.min^{-1} precursor with a space velocity of 0.4 min^{-1}. We confirmed the absence of crystals by (**b**), turbidity and (**d**), a photograph and we measured the steady state concentration by (**f**), HPLC. **c**, **e** and **g** The same experiment as above, but now an 80 mM EDC spike was added in the beginning. The markers in the concentration plot correspond to HPLC data, whereas the red line shows a prediction by our kinetic model. The blue and orange lines are the S_{out} and S_{sat}, respectively.

chemically fueled assemblies[35–37]. The metastable zone in the phase diagram combined with the feedback of the crystals are the core mechanism of the bistability in this work. A state without crystals in the metastable zone can be stable. If crystallization is induced, it switches on a feedback mechanism which raises the product concentration outside of the metastable window which is also stable.

We used microsyringe pumps that continuously supplied a 1.5 ml solution in a vial with 0.3 ml.min^{-1} of a 125 mM EDC solution and 0.3 ml.min^{-1} of a 150 mM precursor solution. In other words, the reactor was supplied with 25 mM EDC.min^{-1} and 30 mM precursor.min^{-1}. To stop the reactor from overflowing a pump extracted 0.6 ml.min^{-1}, thus creating a steady state (i.e., a continuously stirred tank reactor, Fig. 2a, Supplementary Fig. 4). In the setup, every minute, 40% of the reactor volume was replaced, i.e., the space velocity is 0.4 min^{-1}. The sample was placed in a device that constantly monitored its turbidity (Supplementary Fig. 5)[38]. At intervals, the concentration of reactants was measured by HPLC (high-pressure liquid chromatography). The solution remained clear for over an hour (Fig. 2b, d) and HPLC confirmed that the system evolved towards a steady state of 13.0 mM product, i.e., in the metastable zone without crystals (Fig. 2f). If we performed the same experiment but spiked the reactor with 80 mM of EDC just before starting the pumps, the solution became turbid due to the presence of the crystals and evolved to a stable steady state at 29.4 mM, i.e., far above S_{sat} (Fig. 2c, e, g). We determined all rate constants in the chemical reaction cycle (Supplementary Table 1) and combined them in a previously reported kinetic model[26,29,39]. The model takes into account the self-protection mechanism and the metastable window resulting in an accurate prediction of the evolution of the concentration in our experiments (Fig. 2f, g).

The kinetic model was used to predict the steady state anhydride concentration for a range of fuel fluxes to create a so-called hysteresis curve (Fig. 3a). In this curve, the fuel flux is first increased from 0 to 50 mM.min^{-1} and then decreased from 50 to 0 mM.min^{-1} and the corresponding steady state concentrations are calculated. The influx of precursor and the space velocity were kept constant at 30 mM.min^{-1} and 0.4 min^{-1}, respectively. From the curve, three regimes emerge. At low energy fluxes, one steady state concentration without crystals is observed independent of whether the system came from a high or low fuel flux. Similarly, at high fuel fluxes, one steady state is found but now with crystals. In between, two possible steady states are found, i.e., a high steady state concentration with crystals, and a low one without. Experimentally, we validated several points on the hysteresis curve by HPLC (Fig. 3a, Supplementary Fig. 6). To do so, we changed the concentration of the fuel in the solution that feeds the reactor, thus, effectively, changing the influx of fuel with a constant space velocity. After 10 min, the steady state concentration was determined every 2 min. From five datapoints, the mean and deviation in the steady state concentration was calculated. Finally, the turbidity of these samples was also measured to confirm the presence or absence of crystals (Supplementary Fig. 7). We performed similar experiments at various temperatures to qualitatively understand the temperature dependence of the bistable behavior (Fig. 3b, Supplementary Fig. 8–13). We also determined the temperature dependence of the rate constants, S_{out}, and S_{sat} (Supplementary Fig. 2, Supplementary Table 1, and Supplementary Fig. 18, respectively), giving us quantitative understanding and allowing us to expand our kinetic model for several temperatures (Fig. 3c). From these curves, it became clear that the bistable window increases with temperature. The reason for the increase was a faster increase of the S_{sat} with temperature compared to S_{out}. Effectively, at higher temperatures the metastable zone was larger. Furthermore, deactivation rates are higher at higher temperatures which lowers steady state concentrations. As a result, a higher range of fuel fluxes can be applied with the steady state concentrations within the metastable zone. We found that increasing the space velocity, and thus decreasing the time the reactants remained in the reactor, widened the bistable window as well but required higher energy fluxes for its onset (Fig. 3d, Supplementary Fig. 14–17). In our setup, the loss of product is governed by hydrolysis and by outflow from the reactor. Especially at high space velocities, the outflow of the reactor is dominating. Thus, the effect of the self-protection diminishes, and the steady state concentrations approach each other until no more bistability was observed in the system. Simply put; at high space velocities, the crystals spend too little time in the reactor to store the memory required to sustain the on state. We found that when we decreased the space velocity to 0.0 min^{-1} in our model, i.e., there is only fuel flowing into the reactor, but there is no outflow of precursor, product, or waste, we also observed bistability. These observations are significant because they imply that the bistable signature is inherent to the chemical reaction cycle and not a result of the outflow of product and crystals by pumps. Thus, miniaturization of the system is possible because pumps carrying in precursor and removing the product are not required. For example, the system could be miniaturized by using liposomes that are constantly supplied with fuel through

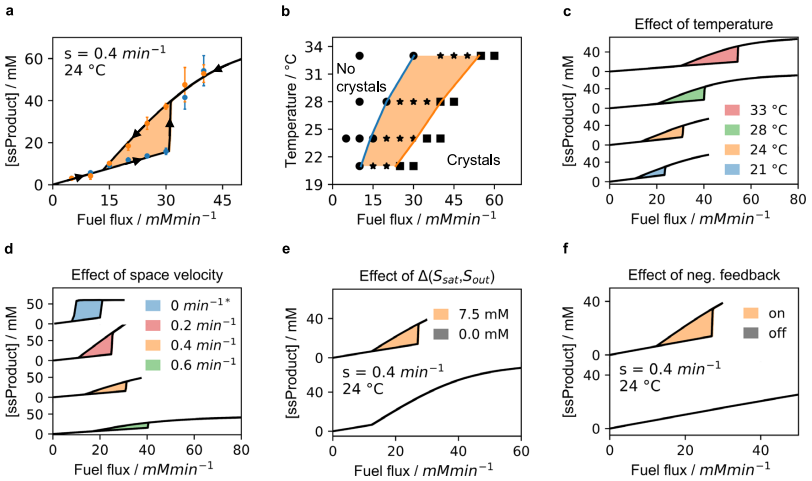

Fig. 3 The bistable window can be tuned by a range of parameters. a The steady state concentration determined by the kinetic model (line) and HPLC (markers) at different fuel fluxes yields a hysteresis curve. The precursor influx was kept at 30 mM.min^{-1} and the space velocity was 0.4 min^{-1}. The markers represent the measured mean steady state concentration and their standard deviation ($n = 5$). **b** The bistability window at various temperatures as determined by turbidity measurements. The conditions are the same as for a except for the temperature. The stars mark the energy flux at which two stable steady states were found. **c** The effect of temperature on the hysteresis curve as determined by the kinetic model. The conditions are the same as for b. The intersection of the high- and low energy branch is drawn in b as blue and orange line. **d** The effect of the space velocity on the bistability window as calculated by the kinetic model at 24 °C. The conditions are the same as for a. (*) For a space velocity of 0.0 min^{-1}, 60 mM precursor starting concentration was used. **e** The influence of the metastable zone and (**f**), negative feedback on the bistability behavior.

nanopores[40]. Finally, the kinetic model confirmed the two physicochemical mechanisms that were critical for the bistability to function, i.e., the metastable window for crystallization, and the crystal's self-protection mechanism. We calculated the hysteresis curve when S_{out} was equal to the S_{sat} (metastable window = 0.0 mM) and compared it to a hysteresis curve with the measured metastable window of 7.5 mM (Fig. 3e). In the curve without a metastable window, the steady state concentration rises with increased EDC flux until the solubility limit is reached. Then, the further increase in EDC flux results in a sudden increase in steady state concentration because crystals are formed that protect the anhydride from hydrolysis, but no hysteresis is found. The importance of the metastable window could be verified experimentally using chemically fueled droplets, which also protect their anhydride through phase separation[26]. However, unlike the crystals, they do not have a measurable metastable window, i.e., their S_{sat} equals S_{out} at 3.5 mM for 2-hexen-1-yl-succinic acid (precursor **2**)[41]. Our kinetic model verified that no hysteresis was found for the droplet-based system, which was experimentally confirmed (Supplementary Figs. 19 and 21). Next, we tested the importance of the self-protection mechanism for the bistability, i.e., we switched off the mechanism in the kinetic model such that the deactivation could occur on both the anhydride in solution and on the anhydride in the crystals with equal rate constants. Without feedback, no bistable zone was found (Fig. 3f).

With the fundamental understanding of the bistability, we tested the response of another precursor (N-Boc-protected glutamic acid, precursor **3**) to various fuel fluxes. This precursor is similar in structure but differs in its reaction rates (Supplementary Fig. 2d and Supplementary Table 1). Given its high solubility, 2 M of NaCl was added to reduce the amount of fuel needed to overcome the supersaturation concentration and initiate crystal formation. A similar hysteresis curve was found compared to precursor **1** (Supplementary Figs. 20 and 21).

Next, we tested the bistable system to serve as volatile memory, i.e., its ability to convert a transient input to a sustained response. First, we sought transient inputs. An off-state was created at 21 °C by feeding a solution 20 mM EDC.min^{-1} and 30 mM precursor.min^{-1} at a space velocity of 0.4 min^{-1}. We used a batch of EDC as input and, with 20 mM EDC or more, the surge in EDC induced crystal formation and switched the system to the on state (Supplementary Fig. 22a). We monitored by turbidity the time it took to switch on the system (Fig. 4a). Unsurprisingly, the more fuel is added the faster the system is switched on. Noteworthy, the steady state level in EDC restored within 2 min while the anhydride steady state level sustained (Supplementary Fig. 22b). We tested several other transient inputs and found the addition of product itself was the most efficient (Fig. 4a, Supplementary Fig. 22c). As little as 0.1 mM of product **1** was required to switch on the system with a half-life time of roughly seven minutes. The addition of high concentration of salts could also serve as input, likely because it transiently decreased S_{Sat} of the system, i.e., it effectively salted out the product (Supplementary Fig. 22d–f). That was further confirmed by the fact that the half-life time followed Hofmeister's series of salting out proteins[42]. Similarly, we sought inputs that could transiently perturb the steady state such that it remained in an off state. We tested several primary amines as input because they react with the product to form their more soluble amide (Fig. 4b and Supplementary Fig. 23). All amines we tested were able to switch off the bistable state, albeit with varying effectiveness. Benzylamine, being the most of them all, allowed us to turn the system off within few seconds. To demonstrate the reversibility of the system, we toggled between on and off several times using 40 mM EDC and 300 mM

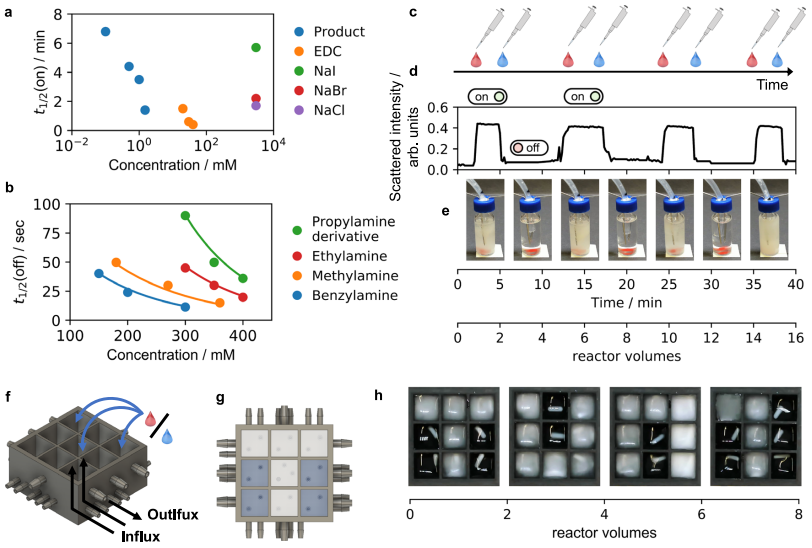

Fig. 4 Toggling between on and off can create pixel displays. The half-life of switching from (**a**), off to on and (**b**), on to off when different triggers are added to the reactor vial. The experimental conditions are 30 mM precursor.min^{-1} and 20 mM EDC.min^{-1} flux at 21 °C and a space velocity of 0.4 min^{-1}. **c** The system is switched between states several times using EDC (red drop) and benzylamine (blue drop) as triggers. **d** The system's turbidity over time as measured by scattered light. **e** Time-lapse photographs of the bistable system. **f** A 3D printed 3 × 3 array in which each reactor can be switched individually and (**g**), the top view picturing a pixel display. **h** By switching particular reactors, TUM is printed.

benzylamine as inputs (Fig. 4c–e and Supplementary Movie 1). Excited about the system's visible ability to store memory, we extended the concept to a matrix display. We developed a matrix of 3 by 3 continuously stirred tank reactors (Fig. 4f, g and Supplementary Fig. 24). Each was continuously fueled with the same conditions as described above. Switching on the pumps gave clear solutions in all pixels. Next, individual reactors were spiked with fuel to print characters (Fig. 4h). Indeed, crystals appeared and sustained which made the pixel switched from off (black) to on (white) resulting in the letter T. Next, we converted the letter T into the U by switching off pixels by addition of benzylamine and switching on others by spiking with fuel. Each reactor could be addressed individually allowing us to print and erase 9-pixel-based patterns or digits (Supplementary Movie 2).

Finally, we explored the idea of connecting switches to create a logic gate[43,44]. In such devices, the output of the gate is dependent on the state of multiple inputs. We opted here for a simple logic gate, i.e., the OR-port (Fig. 5a, b). It must be noted that the OR-port is the most straightforward gate using our design. The design of communicating reactors can, in principle, be further expanded to an AND-port but not to other logic gates in which a positive input should lead to a negative output (like a NOT or NOR-port). In our OR-port, the state of a readout reactor which we call output, is dependent on the state of multiple input reactors. The relation between input and output can be read in a truth table (Fig. 5c). For example, in an OR-port, the output is positive if one input or both inputs are positive. The output is negative only when both inputs are negative. We 3D-printed a design that contains three reactors that can individually be supplied with fuel and precursor (Fig. 5d). The outer two reactors are the input reactors and act as switches, i.e., various triggers (e.g., salt, EDC, or amines) can switch them on or off. The middle reactor is our readout reactor and can compute based on the state of the input reactors. We connected the input reactors to the output reactor through a small hole in the walls (Fig. 5e). Moreover, each of the input reactors had a lower outflow (0.4 ml.min^{-1}) compared to inflow (0.6 ml.min^{-1}). Vice versa, the middle output reactor had a lower inflow (0.2 ml.min^{-1}) compared to outflow (0.6 ml.min^{-1}). Consequently, 0.2 ml.min^{-1} of the liquid from each input reactor was forced through the output reactor (Supplementary Fig. 25). Taken together, the input reactors were regular bistable switches and served as input for the output reactor. Using time-lapse photography and image analysis software, we monitored the outflow of each reactor to quantify the response of different input combinations. When we switched on the system, input A and input B were both off, and the middle output reactor remained clear, too (Fig. 5f, Supplementary Movie 3). Upon switching input A on by adding 40 mM EDC, the output switched from off to on, which was confirmed by a rise in the calculated mean grey value. Input B was not affected by this conversion and stayed off. After 10 min, reactor A was switched off by the addition of 300 mM benzylamine. The output also switched off, albeit somewhat slower (Supplementary Fig. 25). Next, we activated input B by the addition of 3 M NaCl. Again, the change in the input signal B, switched on the output. By assigning a digital 1 to states above a mean grey value threshold of 30 arbitrary units and a digital 0 to states below, we met the conditions required for a logic OR-port[45]. These final experiments demonstrate that it is possible to create an OR-port using our crystal-based bistable reaction network.

Discussion

We showed that bistability can emerge from a fuel-driven reaction cycle that forms crystals. The simplicity means we can now

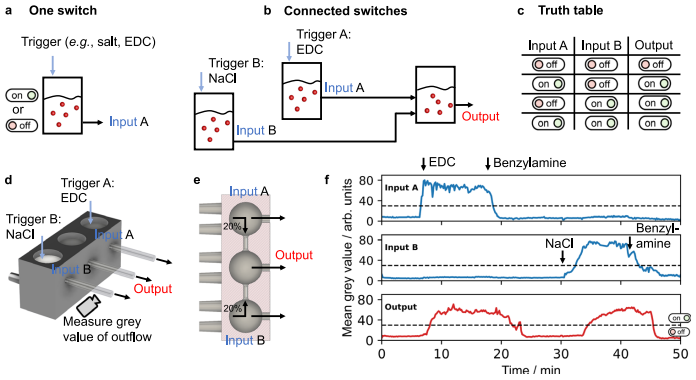

Fig. 5 An OR-gate through the combination of bistable switches. a A schematic representation of a switch. The outflow of the reactor is envisioned as the input for a logic gate. **b** A schematic representation of a logic gate. Two switches affect the state of a readout reactor. **c** The truth table of an OR-port. **d** The 3D printed setup of three connected reaction chambers. **e** Top view section analysis of the printed setup. Part of the input reactors flow into the output reactor. **f** The measured grey value over time detected from the outflux tubing of the three reaction chambers. The experimental conditions are 30 mM precursor.min^{-1} and 20 mM EDC.min^{-1} at 21 °C and a space velocity of 0.4 min^{-1}.

produce memory in systems chemistry without the need for autocatalytic networks or enzymes. The bistable state can be toggled from on and off by small-molecule inputs allowing us to engineer a pixel-based device which can be printed and erased. Like in biological signaling cascades, we coupled reactors such that multiple inputs are used to compute an output. We seek to miniaturize the behavior, for example, in microfluidic droplets or vesicles. We envision coupling each state to a physical response of the compartment by making use of the crystallization. For example, the crystallization could induce deformation or even self-division of the compartment, such that, when several conditions are met, the compartment can make the decision, through Boolean logic, to self-divide.

Methods

Materials. 1-ethyl-3-(3-dimethylaminopropyl)carbodiimide (EDC), NaCl, NaBr, NaI, benzylamine, 33 wt% methylamine in absolute ethanol, 66.0–72.0% ethylamine in H_2O, 3-(Dimethylamino)-1-propylamine, latex beads (polystyrene, 0.1 µm mean particle size), 4-morpholineethanesulfonic acid (MES) buffer were all purchased from Sigma–Aldrich. The precursor N-Boc-L-aspartic acid **1** and N-Boc-L-glutamic acid **3** were purchased from Alfa Aesar and TCI, respectively. All chemicals were used without any further purification. The precursor 2-hexen-1-yl-succinic acid **2** was synthesized by treating the corresponding anhydride with two (mass)-equivalents of MQ water, stirred overnight at room temperature, and then lyophilized[41]. The product was stored at −20 °C until further use. The anhydride of N-Boc-L-aspartic acid was synthesized according to a previously published procedure, treating the diacid with the carbodiimide coupling agent DCC and recrystallization from an acetone/hexane mixture[30]. HPLC grade acetonitrile was purchased from VWR. Milli-Q water was used provided from a Millipore water purifier system.

General sample preparation. We prepared stock solutions of the precursors by dissolving them in 0.2 M MES buffer, after which we adjusted the pH to 3.5 and 6.0 for precursor **1**, **3** (additional 2 M NaCl) and **2**, respectively. Stock solutions of EDC and benzylamine were prepared freshly by dissolution in MQ water.

Batch-fueled experiments. A 100 mM stock solution of precursor **1** or **3** was put in a 1.5 ml HPLC vial equipped with a micro-stir bar. To this solution, various amounts of EDC were added from a 2 M stock solution. The dilution of the precursor solution was kept below 5%. The temperature was adjusted by the Mini Inkubator from Labnet International. The reaction cycle's concentrations were monitored over time by HPLC as described below. These experiments were performed at various temperatures. From these concentrations, we determined the rate constants of deactivation. The remaining rate constants of the reaction cycle were fitted with the kinetic model (vide infra).

HPLC to determine the concentration in the reaction cycle. We applied analytical HPLC (HPLC, Dionex/Thermo Fisher Scientific Ultimate 3000, Hypersil Gold, reversed phase C_{18} column, particle size: 5 µm, length: 250 mm, ID: 20 mm). At several timepoints 30 µl aliquots of the reaction mixture were taken and quenched by 30 µL of a 200 mM benzylamine in water solution[46]. Samples (2 µl injections) were eluted by a linear gradient of acetonitrile in water (Supplementary Fig. 26). Calculation of concentrations was done applying standard curves[46].

Turbidity measurements. The evolutions of the turbidity during the reaction cycle are measured with a home-made setup[38]. The Arduino controlled setup measured transmittance by the detection of scattered laser light. A detailed description of the setup is given in the Supporting Information.

Kinetic model. Calculation of the reaction cycle's concentrations in batch fueled and continuously fueled experiments was done by a kinetic model described in previous work[29,39,46]. Briefly, a set of five differential equations determines the reaction rates of the direct hydration of EDC to yield EDU (r_0), the reaction of precursor with EDC to yield O-acylisourea (r_1), the hydrolysis of the O-acylisourea to yield precursor and EDU (r_3), the conversion of the O-acylisourea to yield anhydride and EDU (r_2), and the hydrolysis of anhydride to yield the precursor (r_4). From these rates, the concentration of EDC, precursor, O-acylisourea, EDU, and anhydride is calculated every second. All reactions are drawn out in Supplementary Fig. 1. To implement the self-protection mechanism, we added to the kinetic model a statement that determines whether crystals are present or not. Crystals are present if the concentration exceeded the supersaturation concentration (S_{sat}). The crystals dissolve when the concentration falls below the solubility (S_{out}). When crystals are absent, the rate of hydrolysis is equal to the rate constant * [anhydride] (1st order). When crystals are present, the rate of hydrolysis if equal to the rate constant * S_{out} (0th order), because the crystals protect all anhydride except for the anhydride that remains in solution (S_{out}). Thus, the model switches from first order to zero order deactivation rates and vice versa, when crystals start to form and dissolve, respectively. The models are provided at: https://github.com/fabianschnitter/Bistability-in-a-chemical-reaction-network.git.

Steady state experiments. We used a continuously stirred tank reactor to create steady state concentrations. In brief, two syringe pumps continuously supplied an HPLC vial with fuel and precursor. A third pump withdrew liquid from the reactor to prevent overflowing. The contents of the vial were stirred by a micro-stirrer. A detailed explanation of the experimental method is given in the Supporting Information.

Determining the temperature dependence of S_{out} and S_{sat}. The phase diagram was drawn by determining S_{out} and S_{sat} in steady state experiments. Regarding S_{out} the system was spiked, and an EDC flux was chosen unable to sustain the on state. The anhydride concentration at the timepoint of crystal dissolution determined by scattered light was chosen as S_{out}. The supersaturation concentration S_{sat} was estimated by steadily increasing the EDC flux until sustained crystal formation was

detected. A detailed explanation of the setup is given in the Supporting Information.

Toggling the switch experiments. The switch was turned to on from a steady state concentration inside the metastable zone by addition of several triggers. The reactor was switched off by addition of primary amines. A detailed description of the experimental method is given in the Supporting Information.

Pixel display experiment. The 3 × 3 pixel display reactor was 3D printed. Each of the nine reactors was filled with 0.6 ml of 100 mM precursor **1**. Then, the flowrate in was set to 0.12 ml.min^{-1} (150 mM acid stock, 100 mM EDC stock) and the flowrate out to 0.24 ml.min^{-1}. Activation of the pixels was done by the addition of 12 µl of a 2 M EDC stock, whereas deactivation was done by replacing 36 µl of the reaction solution with 36 µl 5 M benzylamine solution. A detailed description of the experimental method is given in the Supporting Information.

OR-port experiment. A 1 × 3 array was 3D printed. The flow from the input to the output reactor takes place via a 2 mm diameter hole. The reactor's turbidity is monitored by time lapsed photographs of the outflow tubings in 10 s intervals. Each reactor was filled with 1.5 ml water. Then, each reactor received an influx of 20 mM.min^{-1} EDC and 30 mM.min^{-1} precursor. A detailed description of the experimental method is given in the Supporting Information.

Data availability

The authors declare that all the data supporting the findings of this study are available within the article, the source data files and the Supplementary Information files. Source data are provided with this paper.

Code availability

The Matlab code used to calculate the reaction cycles' concentrations and the script controlling the turbidity device are provided through repositories at github and zenodo. The respective links and references are provided with this paper.

Received: 17 January 2022; Accepted: 29 April 2022;
Published online: 20 May 2022

References

1. Parrilla-Gutierrez, J. M. et al. A programmable chemical computer with memory and pattern recognition. *Nat. Commun.* **11**, 1442 (2020).
2. Gizynski, K. & Gorecki, J. Chemical memory with states coded in light controlled oscillations of interacting Belousov-Zhabotinsky droplets. *Phys. Chem. Chem. Phys.* **19**, 6519–6531 (2017).
3. MacVittie, K., Halamek, J., Privman, V. & Katz, E. A bioinspired associative memory system based on enzymatic cascades. *Chem. Commun. (Camb.)* **49**, 6962–6964 (2013).
4. Ashkenasy, G., Hermans, T. M., Otto, S. & Taylor, A. F. Systems chemistry. *Chem. Soc. Rev.* **46**, 2543–2554 (2017).
5. Kaminaga, A., Vanag, V. K. & Epstein, I. R. A reaction-diffusion memory device. *Angew. Chem. Int. Ed. Engl.* **45**, 3087–3089 (2006).
6. Burrill, D. R. & Silver, P. A. Making cellular memories. *Cell* **140**, 13–18 (2010).
7. Dubnau, D. & Losick, R. Bistability in bacteria. *Mol. Microbiol.* **61**, 564–572 (2006).
8. Padirac, A., Fujii, T. & Rondelez, Y. Bottom-up construction of in vitro switchable memories. *Proc. Natl Acad. Sci. USA* **109**, E3212–E3220 (2012).
9. Inniss, M. C. & Silver, P. A. Building synthetic memory. *Curr. Biol.* **23**, R812–R816 (2013).
10. Stojanovic, M. N. & Stefanovic, D. A deoxyribozyme-based molecular automaton. *Nat. Biotechnol.* **21**, 1069–1074 (2003).
11. Postma, S. G. J., te Brinke, D., Vialshin, I. N., Wong, A. S. Y. & Huck, W. T. S. A trypsin-based bistable switch. *Tetrahedron* **73**, 4896–4900 (2017).
12. Yelleswarapu, M. et al. Sigma factor-mediated tuning of bacterial cell-free synthetic genetic oscillators. *ACS Synth. Biol.* **7**, 2879–2887 (2018).
13. Montagne, K., Gines, G., Fujii, T. & Rondelez, Y. Boosting functionality of synthetic DNA circuits with tailored deactivation. *Nat. Commun.* **7**, 13474 (2016).
14. Semenov, S. N. et al. Autocatalytic, bistable, oscillatory networks of biologically relevant organic reactions. *Nature* **537**, 656–660 (2016).
15. Maity, I. et al. A chemically fueled non-enzymatic bistable network. *Nat. Commun.* **10**, 4636 (2019).
16. Maity, I., Dev, D., Basu, K., Wagner, N. & Ashkenasy, G. Signaling in systems Chemistry: programing gold nanoparticles formation and assembly using a Dynamic Bistable Network. *Angew. Chem. Int Ed. Engl.* **60**, 4512–4517 (2021).
17. Colomer, I., Morrow, S. M. & Fletcher, S. P. A transient self-assembling self-replicator. *Nat. Commun.* **9**, 2239 (2018).
18. Bachmann, P. A., Luisi, P. L. & Lang, J. Autocatalytic self-replicating micelles as models for prebiotic structures. *Nature* **357**, 57–59 (1992).
19. Buhse, T., Pimienta, V., Lavabre, D. & Micheau, J.-C. Experimental evidence of kinetic bistability in a biphasic surfactant system. *J. Phys. Chem. A* **101**, 5215–5217 (1997).
20. Leira-Iglesias, J., Tassoni, A., Adachi, T., Stich, M. & Hermans, T. M. Oscillations, travelling fronts and patterns in a supramolecular system. *Nat. Nanotechnol.* **13**, 1021–1027 (2018).
21. Cafferty, B. J. et al. Robustness, entrainment, and hybridization in dissipative molecular networks, and the origin of life. *J. Am. Chem. Soc.* **141**, 8289–8295 (2019).
22. Novichkov, A. I. et al. Autocatalytic and oscillatory reaction networks that form guanidines and products of their cyclization. *Nat. Commun.* **12**, 2994 (2021).
23. Grzybowski, B. A. & Huck, W. T. The nanotechnology of life-inspired systems. *Nat. Nanotechnol.* **11**, 585–592 (2016).
24. Altay, Y., Tezcan, M. & Otto, S. Emergence of a new self-replicator from a dynamic combinatorial library requires a specific pre-existing replicator. *J. Am. Chem. Soc.* **139**, 13612–13615 (2017).
25. Tena-Solsona, M., Wanzke, C., Riess, B., Bausch, A. R. & Boekhoven, J. Self-selection of dissipative assemblies driven by primitive chemical reaction networks. *Nat. Commun.* **9**, 2044 (2018).
26. Riess, B. et al. Dissipative assemblies that inhibit their deactivation. *Soft Matter* **14**, 4852–4859 (2018).
27. Kulkarni, S. A., Kadam, S. S., Meekes, H., Stankiewicz, A. I. & ter Horst, J. H. Crystal nucleation kinetics from induction times and metastable zone widths. *Cryst. Growth Des.* **13**, 2435–2440 (2013).
28. Kariyawasam, L. S. & Hartley, C. S. Dissipative assembly of Aqueous Carboxylic Acid Anhydrides fueled by Carbodiimides. *J. Am. Chem. Soc.* **139**, 11949–11955 (2017).
29. Tena-Solsona, M. et al. Non-equilibrium dissipative supramolecular materials with a tunable lifetime. *Nat. Commun.* **8**, 15895 (2017).
30. Schnitter, F. & Boekhoven, J. A Method to Quench Carbodiimide-Fueled Self-Assembly. *ChemSystemsChem* **3** (2020).
31. Hossain, M. M., Atkinson, J. L. & Hartley, C. S. Dissipative assembly of macrocycles comprising multiple transient bonds. *Angew. Chem. Int Ed. Engl.* **59**, 13807–13813 (2020).
32. Panja, S., Dietrich, B. & Adams, D. J. Chemically Fuelled Self-Regulating Gel-to-Gel Transition. *ChemSystemsChem* **2** (2019).
33. Bal, S., Das, K., Ahmed, S. & Das, D. Chemically fueled dissipative self-assembly that exploits cooperative catalysis. *Angew. Chem. Int. Ed. Engl.* **58**, 244–247 (2019).
34. Billot, P., Couty, M. & Hosek, P. Application of ATR-UV spectroscopy for monitoring the crystallisation of UV absorbing and nonabsorbing molecules. *Org. Process Res. Dev.* **14**, 511–523 (2010).
35. Das, K., Gabrielli, L. & Prins, L. J. Chemically fueled self-assembly in Biology and Chemistry. *Angew Chem Int Ed Engl* (2021).
36. Singh, N., Formon, G. J. M., De Piccoli, S. & Hermans, T. M. Devising synthetic reaction cycles for dissipative nonequilibrium self-assembly. *Adv. Mater.* **32**, e1906834 (2020).
37. Giuri, D. et al. Exploiting and controlling gel-to-crystal transitions in multicomponent supramolecular gels. *Chem. Sci.* **12**, 9720–9725 (2021).
38. Rieß, B., Schnitter, F. & Boekhoven, J. fabianschnitter/Script-turbidity-device: Script-turbidity-device (v1.0). *Code on Zenodo* https://doi.org/10.5281/zenodo.6451325 (2022).
39. Schnitter, F. & Boekhoven, J. fabianschnitter/Bistability-in-a-chemical-reaction-network: Matlab code to model carbodiimide-driven reaction cycles (v1.0). *Code on Zenodo* https://doi.org/10.5281/zenodo.6451339 (2022).
40. Krishnan, S. et al. Molecular transport through large-diameter DNA nanopores. *Nat. Commun.* **7**, 12787 (2016).
41. Wanzke, C., Tena-Solsona, M., Rieß, B., Tebcharani, L. & Boekhoven, J. Active droplets in a hydrogel release drugs with a constant and tunable rate. *Mater. Horiz.* **7**, 1397–1403 (2020).
42. Zhang, Y. & Cremer, P. S. Interactions between macromolecules and ions: The Hofmeister series. *Curr. Opin. Chem. Biol.* **10**, 658–663 (2006).
43. Fan, X. & Walther, A. pH feedback lifecycles programmed by enzymatic logic gates using common foods as fuels. *Angew. Chem. Int Ed. Engl.* **60**, 11398–11405 (2021).
44. Chatterjee, A., Mahato, C. & Das, D. Complex cascade reaction networks via cross beta amyloid nanotubes. *Angew. Chem. Int Ed. Engl.* **60**, 202–207 (2021).
45. Katz, E. Enzyme-based logic gates and networks with output signals analyzed by various methods. *Chemphyschem* **18**, 1688–1713 (2017).

46. Schnitter, F. et al. Synthesis and characterization of chemically fueled supramolecular materials driven by carbodiimide-based fuels. *Nat. Protoc.* **16**, 3901–3932 (2021).

Acknowledgements
The BoekhovenLab is grateful for support by the TUM Innovation Network - RISE funded through the Excellence Strategy. This research was conducted within the Max Planck School Matter to Life supported by the German Federal Ministry of Education and Research (BMBF) in collaboration with the Max Planck Society. F.S. and B.R. acknowledge funding by the Deutsche Forschungsgemeinschaft (DFG, German Research Foundation) – SFB-863 – Project ID 111166240 (Project B11).

Author contributions
F.S. designed and performed the experiments and wrote the manuscript. B.R. built and wrote the code for the turbidity device. C.J. performed the single crystal X-ray diffraction experiment and evaluated the crystal structure data. J.B. designed experiments, outlined, and wrote the manuscript, and supervised the project. All authors discussed the experimental results.

Funding
Open Access funding enabled and organized by Projekt DEAL.

Competing interests
The authors declare no competing interests.

Additional information
Supplementary information The online version contains supplementary material available at https://doi.org/10.1038/s41467-022-30424-2.

Correspondence and requests for materials should be addressed to Job Boekhoven.

Peer review information *Nature Communications* thanks the anonymous reviewer(s) for their contribution to the peer review of this work. Peer reviewer reports are available.

Reprints and permission information is available at http://www.nature.com/reprints

Publisher's note Springer Nature remains neutral with regard to jurisdictional claims in published maps and institutional affiliations.

Supplementary Information

Memory, switches, and an OR-port through bistability in chemically fueled crystals

Fabian Schnitter[1], Benedikt Rieß[1], Christian Jandl[2], Job Boekhoven[1,3,*]

1 Department of Chemistry, Technical University of Munich, Lichtenbergstrasse 4, 85748 Garching, Germany.

2 Catalysis Research Centre, Technical University of Munich, Lichtenbergstrasse 4, 85748 Garching, Germany

3 Institute for Advanced Study, Technical University of Munich, Lichtenbergstrasse 2a, 85748 Garching, Germany.

*Correspondence to: job.boekhoven@tum.de

Supplementary methods

Turbidity measurements.

The evolution of the turbidity during the reaction cycle is measured with an Arduino controlled setup (Supplementary Figure 5). The setup measures the scattering of 660 nm laser light under a 90° angle. The main advantage of such a setup compared to a commercial setup is the possibility to continuously stir the sample and connect it to inflow and outflow tubing. The scattering rate is measured at 10-second intervals. By using a smaller stirring plate, the setup can be put into an incubation chamber to control the temperature during the reaction cycle. The Arduino script is provided at: https://github.com/fabianschnitter/Script-turbidity-device.git.

Steady state experiments.

We used a continuously stirred tank reactor to create steady state concentrations. The reactor setup was made up of a 1.5 ml HPLC vial equipped with a micro stir bar put on a stir plate (600 rpm). The reactor was continuously supplied by a 0.3 $ml.min^{-1}$ inflow from a 150 mM precursor **1** or **3** stock solution (0.12 $ml.min^{-1}$ from a 37.5 mM precursor **2** stock solution). The inflow rate of EDC was equal to the inflow rate of precursor, but the stock concentration varied to apply different molar fluxes. The outflow rate was 0.6 $ml.min^{-1}$ (0.24 $ml.min^{-1}$ for precursor **2**). Aladdin AL-1000 syringe pumps from WPI were used equipped with 20 ml Braun Injekt syringes (ID = 20.10 mm). We used silicone tubing (OD = 1.8 mm, ID = 1.0 mm) and Braun Sterican needles (ID = 0.8 x 120 mm) for injection. For the outflow, a tygon tubing (OD = 3.2 mm, ID = 1.6 mm) was directly placed through a pre sliced septum of the HPLC vial in the reactor. A tubing diameter of 1.6 mm appeared to be best to homogeneously remove the solution with the crystals. At lower diameters, the tubing tended to clog, whereas larger diameters reduce the velocity which is necessary to remove the crystals. We tested the quality of constantly removing the crystal state anhydride by measuring the sum of concentration acid and anhydride inside the reaction vessel over time to exclude up concentration of the precursor (Supplementary Figure 4). For longer experiments larger 50 ml Braun Omnifix syringes (ID = 27.90 mm) were used. To measure the turbidity of the sample, the HPLC vial was placed in the home-made turbidity device. The temperature was controlled by placing the entire setup in an incubator. Measuring the reaction mixture's temperature was done by the In-outdoor Traceable thermometer purchased from VWR. The reaction vessel was supplied by the syringe pumps placed outside the incubator at controlled 21 °C ambient temperature. We prevented the reaction mixture to cool down by placing roughly 20 cm of tubing inside the incubator to allow the influx solution to approach the set incubator's temperature (Supplementary Figure 4). As a starting reaction mixture, 100 mM precursor **1**, 10 mM precursor **2,** or 150 mM precursor **3** was used. Thereby, addition of the 80 mM EDC spike (50 mM regarding **2**) before pumping

resulted in initial crystal or droplet formation. To measure the reaction cycle's concentrations, 30 µl aliquots were taken over time and quenched with a 200 mM benzylamine solution (1:1 dilution).

Determining the temperature dependence of S_{out} and S_{sat}.

The S_{out} and S_{sat} for several temperatures was determined in steady state experiments (Supplementary Fig. 18 and Fig. 1c). The S_{out} was determined by spiking the system beforehand applying a 10 mM.min^{-1} EDC and 30 mM.min^{-1} precursor **1** flux. This EDC flux did not sustain the crystalline on state which was shown by a decrease in scattering. We assumed a complete dissolution of the crystals at the timepoint reaching 0.15 scattering units. The anhydride concentration calculated by the kinetic model at this timepoint was taken as the S_{out}. The supersaturation concentration S_{sat} could not be measured directly as common methods like cooling down a solution of a known concentration is not possible. During the reaction cycle, anhydride is constantly produced and consumed and a change in temperature affects the steady state concentration. Furthermore, the induction time must be considered when directly measuring S_{sat}, which is the time between reaching a supersaturated solution and the onset of detectable nucleation[1]. Instead, we approached the supersaturation concentration by increasing the EDC flux and measuring the scattering of the system in steady state. For instance, at 21 °C, an EDC flux between 20 and 25 mM.min^{-1} evoked a crystal steady state detected by an increase in scattering. The corresponding anhydride steady state concentration was calculated by the kinetic model and taken as S_{sat} in the phase diagram.

Toggling the switch experiments.

The reactor was loaded with 1.5 ml water. The syringes were operated for 5 min to establish steady state concentrations (21 °C, 150 mM acid **1** stock, 100 mM EDC stock, inflow 0.3 ml.min^{-1}, respectively). For the activation, different amounts of EDC were added from a 2 M stock solution (30.0 µl, 22.5 µl, 15.0 µl, 7.50 µl), whereas the crystalline anhydride of **1** and the salts (NaCl: 438 mg, 263 mg, 88.0 mg; NaBr: 464 mg; NaI: 675 mg) were added as solids. As the crystalline anhydride was added in small amounts (1.6 mg, 1.1 mg, 0.54 mg, 0.11 mg), the reactor's volume was increased to 5 ml (150 mM acid stock, 100 mM EDC stock, inflow 1.0 ml.min^{-1}, respectively). Polystyrene (1.5 mg) was added as a control to ensure that the change in volume did not induce crystallization.

For the deactivation, 1.5 ml of 100 mM precursor **1** solution was initially activated with 40 mM EDC. After stabilizing the reactor for 5 min by pumping (21 °C, 150 mM acid **1** stock, 100 mM EDC stock, inflow 0.3 ml.min^{-1}, respectively), deactivation was done by adding various amounts of high concentrated stock solutions (5 M benzylamine: 90 µl, 60 µl, 45 µl; 33 wt% methylamine: 100 µl, 75 µl, 50 µl; 70 wt% ethylamine: 69 µl, 61 µl, 52 µl; 5 M 3-(dimethylamino)-

1-propylamine: 120 µl, 105 µl, 90 µl) to the reaction vial. The dilution was kept well below 10%. When switching the system several times, a fraction of the reaction solution was replaced by the deactivation stock to prevent volume expansion.

Pixel-display experiment.

The 3x3 pixel display reactor was 3D printed using the Form 2 from Formlabs applying a black photopolymer resin. After the print, the 3x3 pixel display was treated 20 min with isopropanol and cured for 5 min at 55 °C. Each of the nine reactors was filled 0.6 ml of 100 mM precursor **1**. Then, the flowrate in was set to 0.12 ml.min^{-1} (150 mM acid stock, 100 mM EDC stock) and the flowrate out to 0.24 ml.min^{-1}. To control 27 syringes simultaneously, two Aladdin AL-1600 and five Aladdin AL-1000 were used with 3D printed extensions to hold three syringes instead of one (Supplementary Fig. 24). The 3x3 pixel display was placed on a stir plate. Activation of the pixels was done by the addition of 12 µl of a 2 M EDC stock, whereas deactivation was done by replacing 36 µl of the reaction solution with 36 µl 5 M benzylamine solution. Timelapsed photographs in 10 seconds intervals were recorded by a Logitech BRIO webcam. Processing the photographs was done by imageJ extended by a fiji distribution. The 3D model 3x3 pixel display as well as the extension of the pumps can be found at: https://www.thingiverse.com/thing:4960191 and https://www.thingiverse.com/thing:4971601.

OR-port experiment.

A 1x3 reactor array was 3D printed as described above. Luer lock connectors were designed to easily connect the reactors with the inflow tubing. The outflow tubing is connected via a hole at the back of the reactors. At the bottom, cuvette micro stirrers from 2MAG are placed right beyond the reaction reactors. The flow from the input to the output reactor takes place via a 2 mm diameter hole. The reactor's turbidity is monitored by time lapsed photographs of the outflow tubings in 10 seconds intervals. Each reactor was filled with 1.5 ml water. Then, each reactor received an influx of 20 mM.min^{-1} EDC and 30 mM.min^{-1} precursor **1**. Specifically, the input reactors received 0.3 ml.min^{-1} of a 150 mM acid **1** stock and 0.3 ml.min^{-1} of a 100 mM EDC stock. From the input reactors, 0.4 ml.min^{-1} was withdrawn, and 0.2 ml.min^{-1} flowed into the output reactor. The output reactor received 0.1 ml.min^{-1} of a 450 mM precursor **1** stock and 0.1 ml.min^{-1} of a 300 mM EDC stock. A more detailed overview is given in Supplementary Figure 25. Moreover, the output reactor also received 0.2 ml.min^{-1} from each input reactor. Activation of the input reactors was done by the addition of 30 µL from a 2 M EDC stock or 263 mg NaCl. Deactivation was done by replacing 90 µl of the reaction solution with 90 µL 5 M benzylamine solution. The 3D model can be found at: https://www.thingiverse.com/thing:4971613.

Supplementary Figures

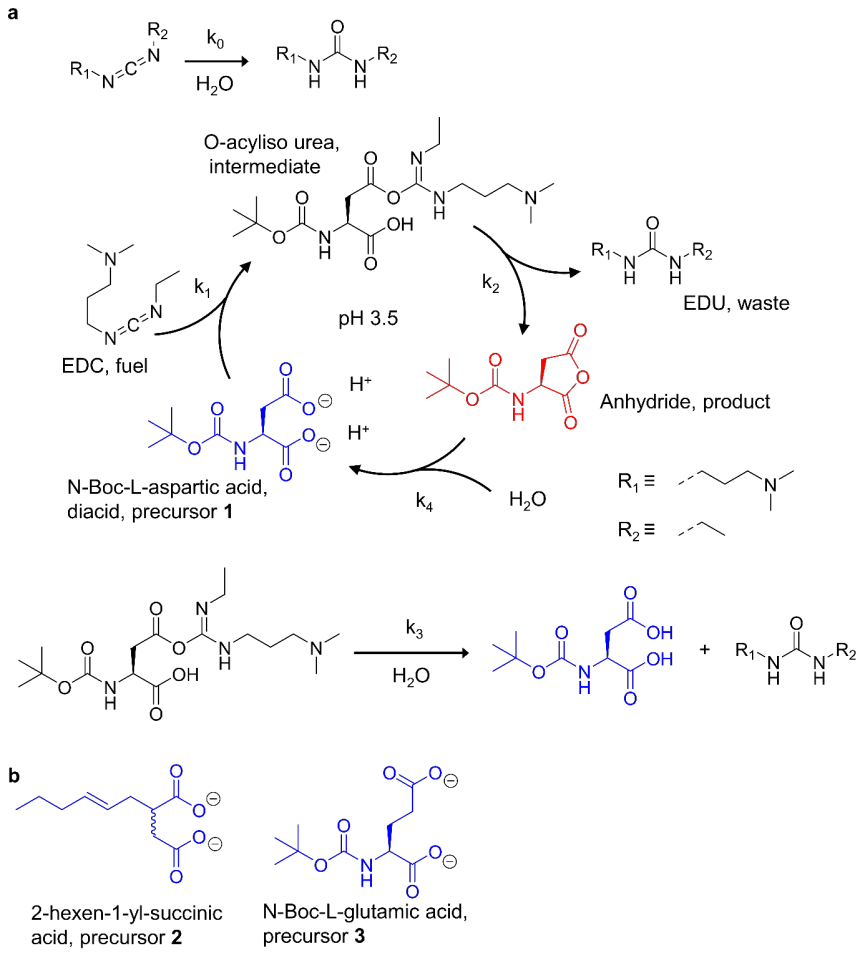

Supplementary Figure 1: The reactions involved in the chemical reaction cycle. a All reactions shown are simultaneously taking place at various rates. The direct hydration of the EDC fuel (k_0) was examined in previous work[2]. The start of the reaction cycle is the addition of one EDC molecule to the diacid precursor, forming a high energy intermediate (k_1). On releasing the waste product EDU, the intermediate further reacts to the active anhydride product (k_2). Furthermore, the intermediate decomposes in a side reaction at low rates to the precursor by direct hydrolysis (k_3). The deactivation reaction comprises the degeneration of the precursor driven by the anhydride hydrolysis (k_4). **b** Further diacids used as precursors.

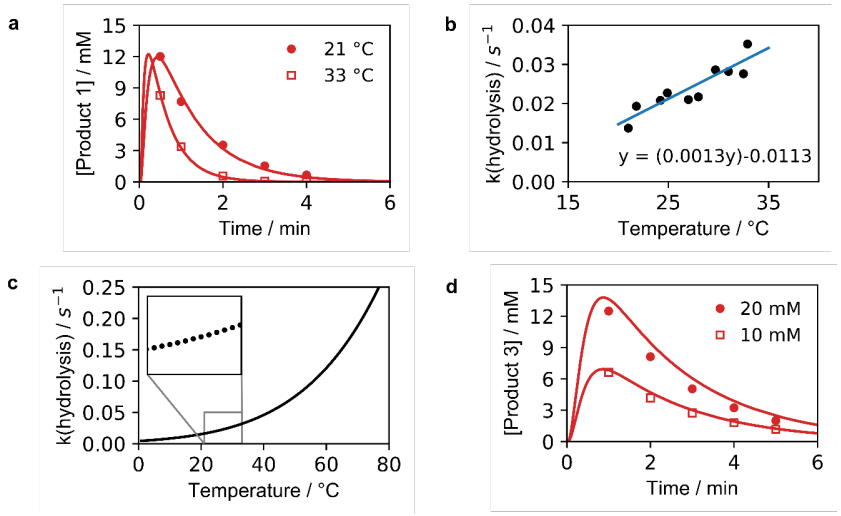

Supplementary Figure 2: Batch fueled experiments to extract deactivation rate constants. a The first order decay profile of anhydride product **1** hydrolysis over time at various temperatures. A 100 mM precursor solution was fueled with 20 mM EDC. The profiles at 21 °C and 33 °C are taken as exemplary curves for all temperatures measured. **b** The deactivation rate constants of **1** determined for different temperatures. **c** The effect of temperature on k_4 of **1** as calculated by the Arrhenius correlation. **d** The first order decay profile of 100 mM of precursor **3** when fueling with different amounts of EDC.

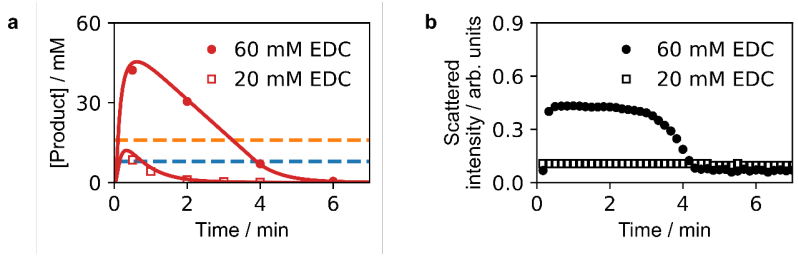

Supplementary Figure 3: The reaction cycle's response at 24 °C when adding different amounts of EDC fuel to 100 mM precursor 1[4]. a When adding 20 mM of EDC, the anhydride yield is below S_{sat} (orange line), whereas when increasing the EDC amount to 60 mM the anhydride concentration exceeds S_{sat}. **b** The measured scattering shows the presence of crystals when 60 mM fuel is added, whereas no increase in scattering was measured for 20 mM EDC addition.

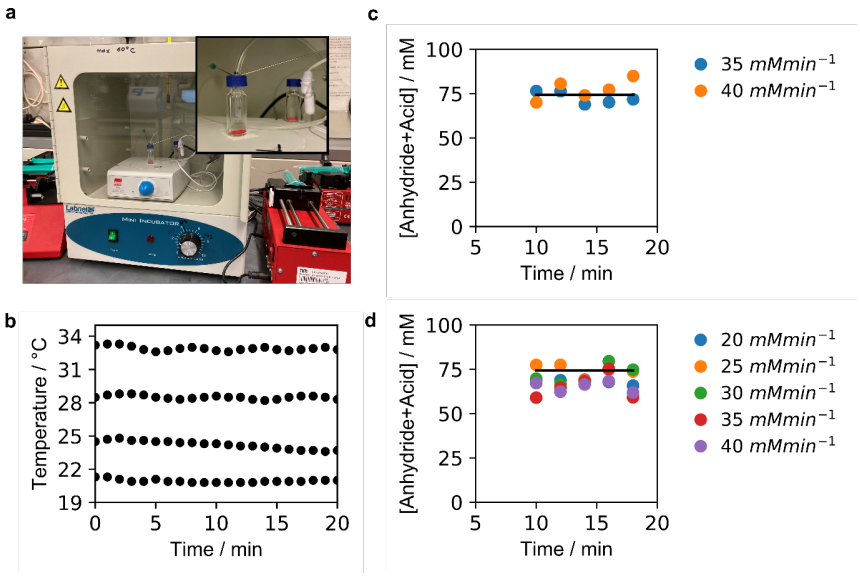

Supplementary Figure 4: Experimental setup of steady state experiments. a Photograph of the experimental setup. **b** Monitoring the temperature stability of the steady state experiments. **c**, **d** The sum of the concentration precursor **1** and the corresponding product over time. The concentration should be roughly constant and ensures that the crystals are not clogging the tubing or accumulate in the reactor. In the data in **c**, no spike was added. In contrast, an 80 mM EDC spike was added at **d**. The markers represent HPLC data, and the line represents the concentration predicted by the kinetic model.

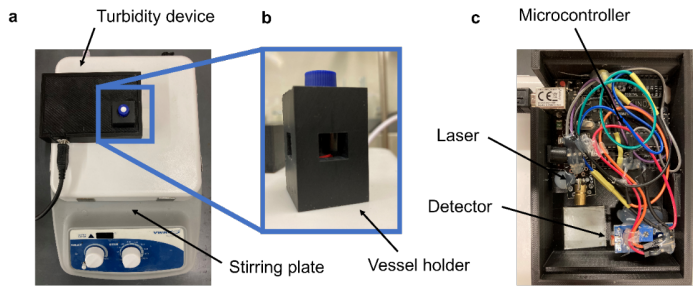

Supplementary Figure 5: The setup used to measure the reaction cycle's turbidity. a The device is placed on a stirring plate to homogeneously mix the crystals formed by the anhydride. **b** An HPLC vial was used as sample container, which is placed inside a 3D printed vessel holder. **c** The scattered light is measured under a 90° angle. The laser and detector are controlled by an Arduino microcontroller. The electronic components are covered by a 3D printed case, small enough to put into an incubator on top of a small stir plate.

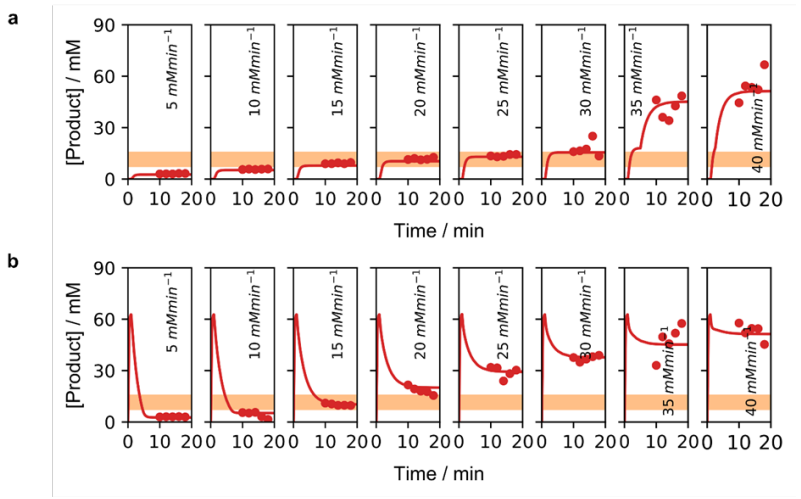

Supplementary Figure 6: The steady state concentration of the anhydride product of 1 at 24 °C and a space velocity of 0.4 min^{-1}. The markers indicate concentrations measured by HPLC and the solid line represents modelled data. **a** When fueling at least with 35 mM.min^{-1} EDC, the steady state concentration surpasses the metastable zone (marked orange) and crystal formation starts resulting in much higher steady state levels. **b** When adding an 80 mM EDC spike before starting the constant influx of EDC and precursor, crystal formation already starts at lower fuel influxes, i.e., at 20 mM.min^{-1} EDC.

8

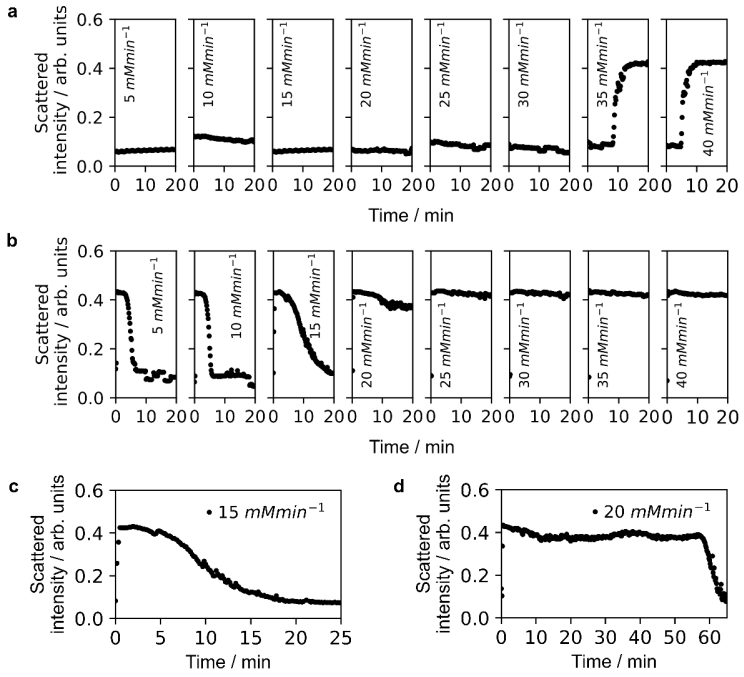

Supplementary Figure 7: The scattering of reaction cycle 1 as a measure for turbidity at 24 °C and a space velocity of 0.4 min^{-1}. a When applying at least a 35 mM.min^{-1} EDC flux, crystallization starts to occur which is shown by an increase in the scattering at 10 min. **b** The addition of an 80 mM EDC spike before starting the influx of EDC and precursor results in initial crystal formation. Low EDC fluxes are not sufficient to sustain the crystals. At least a 20 mM.min^{-1} EDC flux was required, resulting in a steady state in sustained turbidty reached at around 10 min. The continuous turbidity indicates the persistent presence of crystals. **c**, **d** The curves from b measured for longer times.

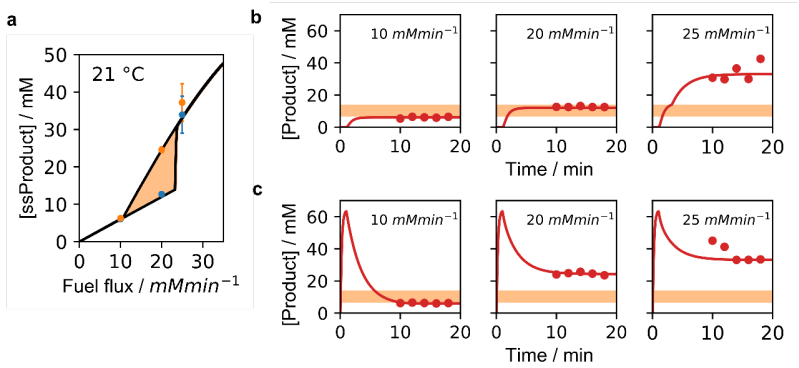

Supplementary Figure 8: The steady state concentration of the anhydride product of 1 at 21 °C and a space velocity of 0.4 min^{-1}. a The hysteresis curve was calculated with the kinetic model by incrementally increasing and decreasing the EDC fuel flux. Several points were experimentally validated by calculating the mean and standard deviation of five steady state datapoints measured by HPLC. The bistable window is marked in orange. **b** The steady state concentrations at different fuel fluxes. The markers indicate concentrations measured by HPLC and the solid line represents modelled data when no EDC and **c**, an 80 mM EDC spike was added before starting the constant influx of EDC and precursor. The orange zone represents the metastable zone.

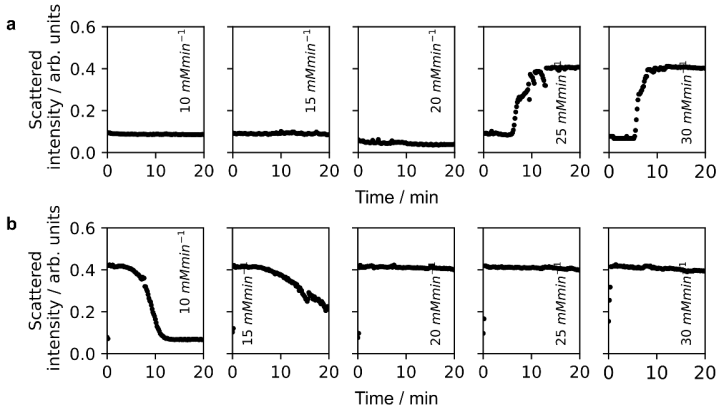

Supplementary Figure 9: The scattering of reaction cycle 1 as a measure for turbidity at 21 °C and a space velocity of 0.4 min^{-1}. a No EDC and **b**, an 80 mM EDC spike was added before starting the pumps.

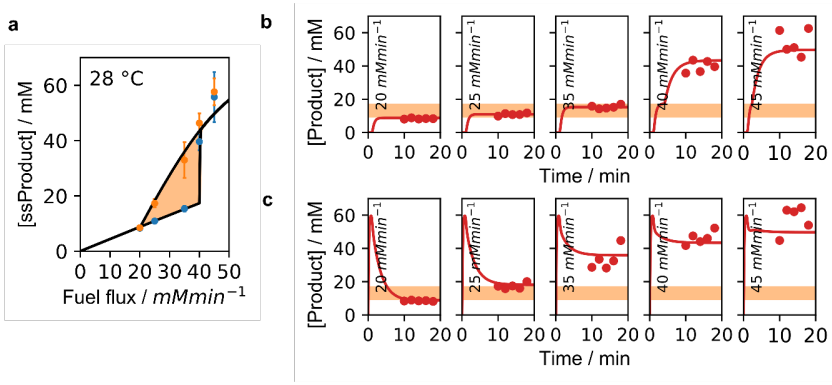

Supplementary Figure 10: The steady state concentration of the anhydride product of 1 at 28 °C and a space velocity of 0.4 min^{-1}. a The hysteresis curve was calculated with the kinetic model by incrementally increasing and decreasing the EDC fuel flux. Several points were experimentally validated by calculating the mean and standard deviation of five steady state datapoints measured by HPLC. The bistable window is marked in orange. **b** The steady state concentrations at different fuel fluxes. The markers indicate concentrations measured by HPLC and the solid line represents modelled data when no EDC and **c** an 80 mM EDC spike was added before starting the constant influx of EDC and precursor. The orange zone represents the metastable zone.

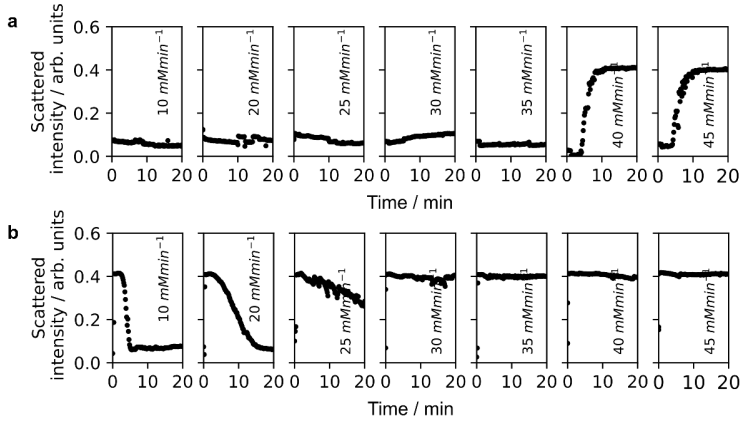

Supplementary Figure 11: The scattering of reaction cycle 1 as a measure for turbidity at 28 °C and a space velocity of 0.4 min^{-1}. a No EDC and **b** an 80 mM EDC spike was added before starting the pumps.

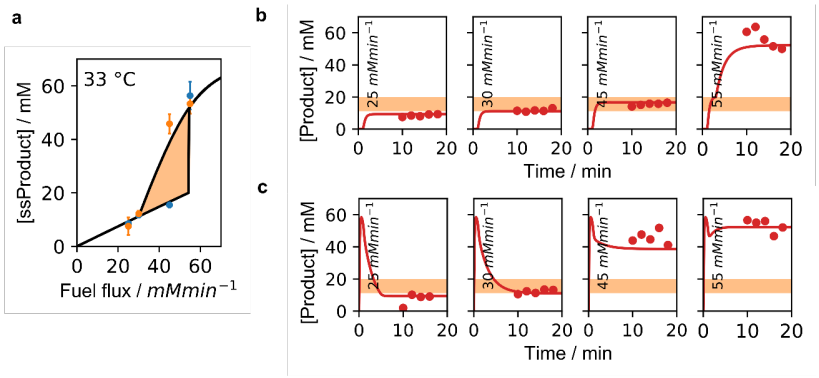

Supplementary Fig. 12: The steady state concentration of the anhydride product of 1 at 33 °C and a space velocity of 0.4 min^{-1}. a, The hysteresis curve was calculated with the kinetic model by incrementally increasing and decreasing the EDC fuel flux. Several points were experimentally validated by calculating the mean and standard deviation of five steady state datapoints measured by HPLC. The bistable window is marked in orange. **b**, The steady state concentrations at different fuel fluxes. The markers indicate concentrations measured by HPLC and the solid line represents modelled data when no EDC and **c**, an 80 mM EDC spike was added before starting the constant influx of EDC and precursor. The orange zone represents the metastable zone.

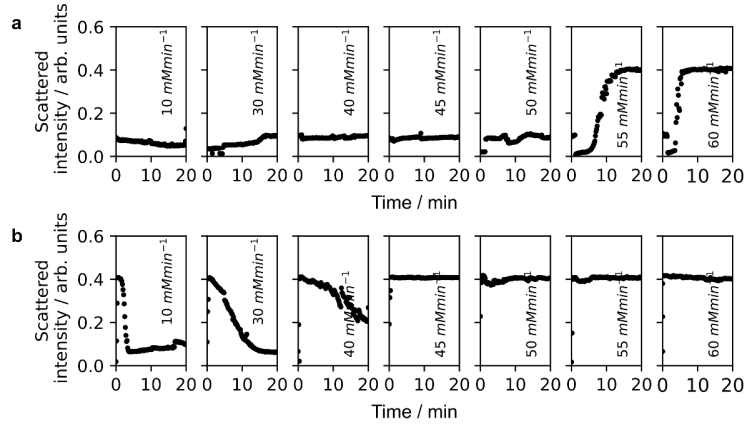

Supplementary Figure 13: The scattering of reaction cycle 1 as a measure for turbidity at 33 °C and a space velocity of 0.4 min^{-1}. a No EDC and **b**, an 80 mM EDC spike was added before starting the pumps.

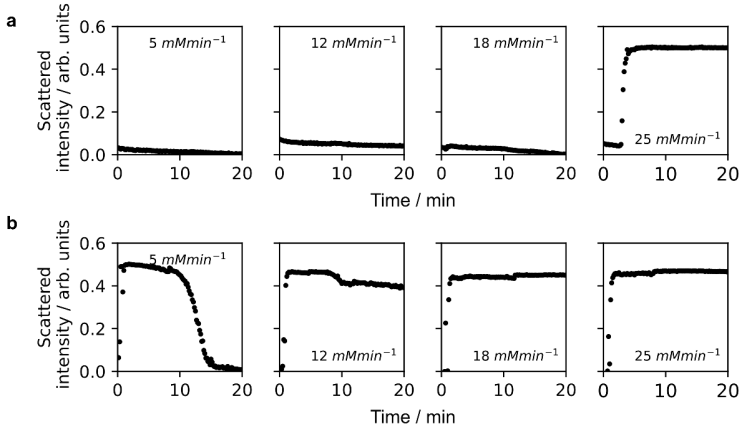

Supplementary Figure 14: The scattering of reaction cycle 1 as a measure for turbidity at 24 °C and a space velocity of 0.0 min^{-1}. A 2 ml reaction vial containing 60 mM precursor **1** was influxed with different amounts of EDC. The flowrate was set to 15 µl.min^{-1}. **a** No EDC and **b**, an 80 mM EDC spike was added before starting the pumps.

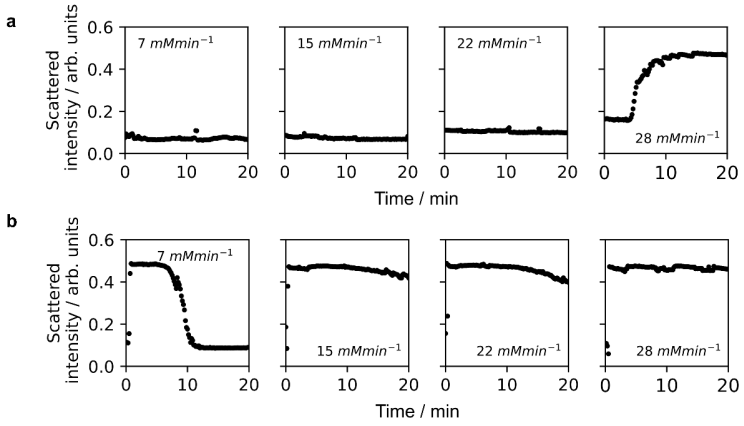

Supplementary Figure 15: The scattering of reaction cycle 1 as a measure for turbidity at 24 °C and a space velocity of 0.2 min^{-1}. The flowrate in was set to 0.15 ml.min^{-1} and the flowrate out of the reactor was set to 0.30 ml.min^{-1}. **a** No EDC and **b**, an 80 mM EDC spike was added before starting the pumps.

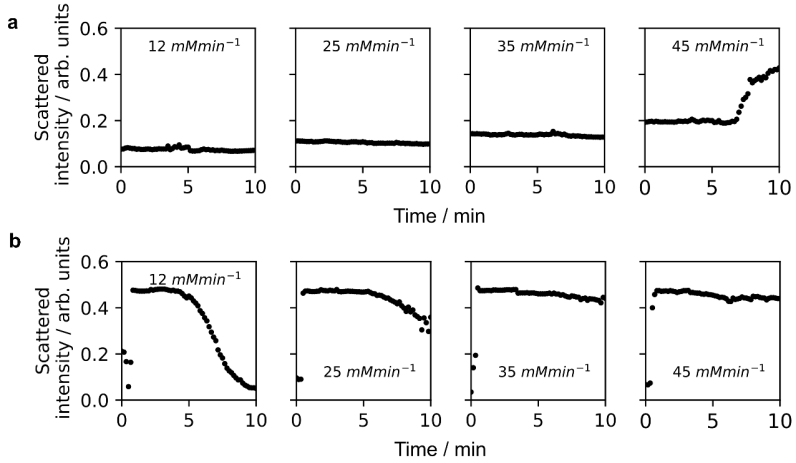

Supplementary Figure 16: The scattering of reaction cycle 1 as a measure for turbidity at 24 °C and a space velocity of 0.6 min^{-1}. The flowrate in was set to 0.45 ml.min^{-1} and the flowrate out of the reactor was set to 0.90 ml.min^{-1}. **a** No EDC and **b**, an 80 mM EDC spike was added before starting the pumps.

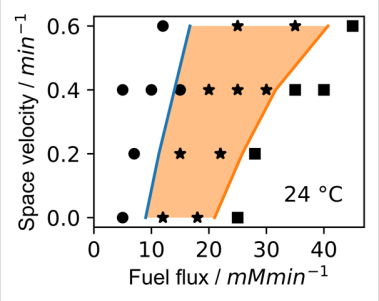

Supplementary Figure 17: The bistability window at 24 °C at various space velocities as determined by turbidity measurements. The stars mark the energy flux at which two stable steady-states were found. The blue and orange line are intersections of the low and high steady state concentrations determined by the kinetic model (Fig. 3d).

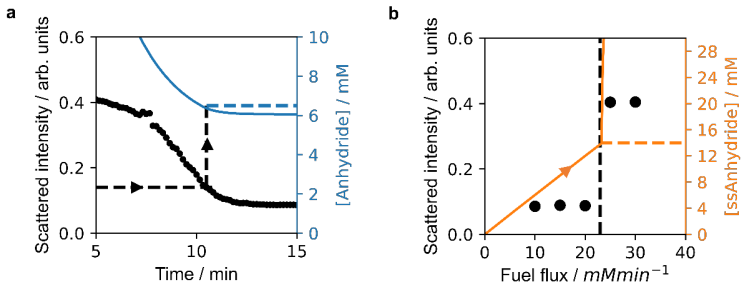

Supplementary Figure 18: Determining the temperature dependence of S_{out} and S_{sat}. The method is exemplary shown at 21 °C for all temperatures in the phase diagram (Fig. 1 c). **a** The scattering over time when a 10 mM.min^{-1} EDC flux was applied to the reaction vessel after adding an 80 mM EDC spike at 21 °C. The blue line represents the anhydride evolution over time calculated by the kinetic model and yields S_{out}. **b** The steady state scattering measured when different EDC fluxes are applied at 21 °C. The orange line represents the appearing steady state concentration in anhydride calculated by the model and yields S_{sat}.

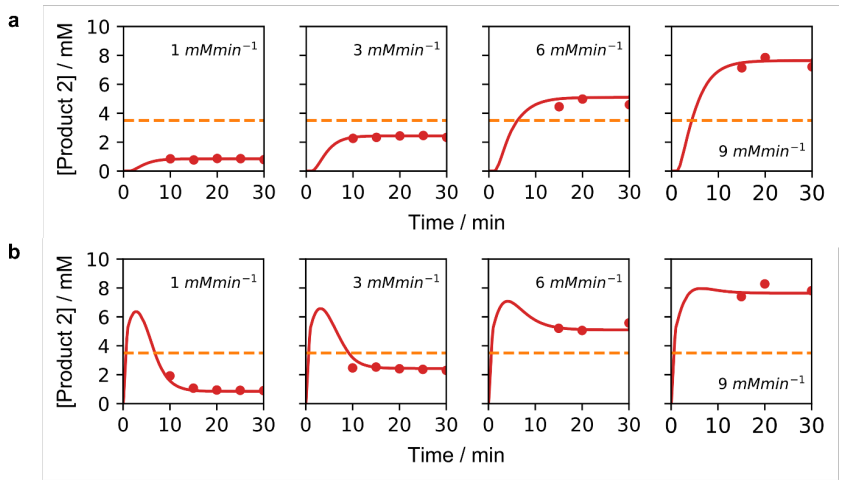

Supplementary Figure 19: The steady state concentration of the anhydride product of 2 at 25 °C, pH 6.0 and a space velocity of 0.32 min^{-1}. The markers indicate concentrations measured by HPLC and the solid line represents modelled data. Whilst the precursor influx was kept constant at 6 mM.min^{-1}, several EDC fluxes were applied when **a**, no EDC and **b**, a 50 mM EDC spike was added at the beginning.

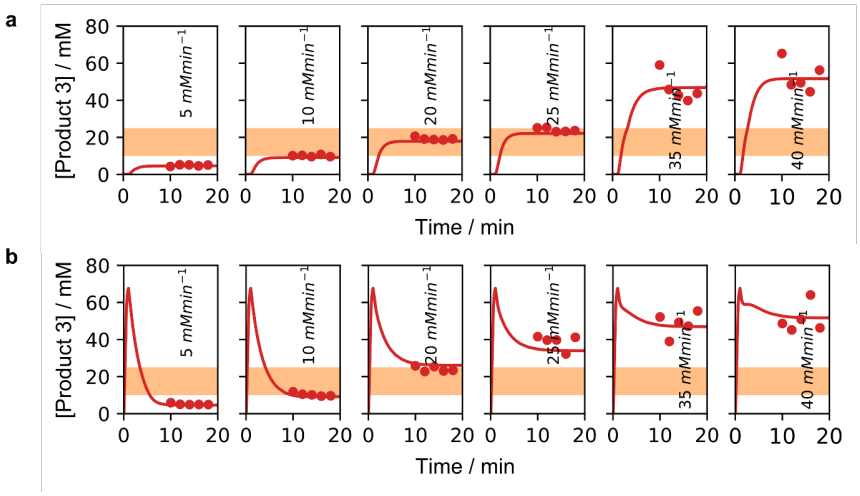

Supplementary Figure 20: The steady state concentration of the anhydride product of 3 at 24 °C, pH 3.5 and a space velocity of 0.4 min^{-1}. The markers indicate concentrations measured by HPLC and the solid line represents modelled data. The precursor was influxed continuously at a rate of 30 mM.min^{-1}. Increasing the EDC flux increases the steady state concentration and **a**, crystals start to form at an EDC flux of at least 35 mM.min^{-1}. **b** When adding an 80 mM EDC spike before starting the pumps, an EDC flux of 20 mM.min^{-1} is sufficient to form sustained crystals and results in higher anhydride steady state concentrations.

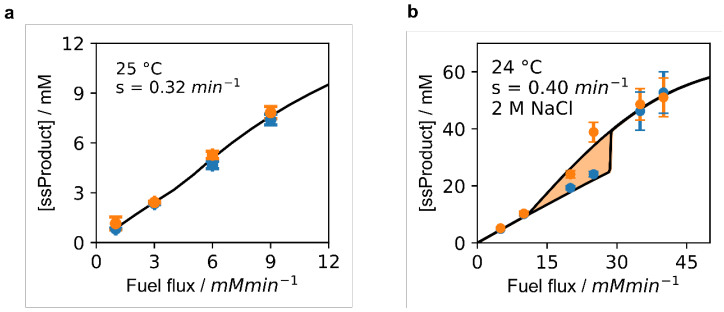

Supplementary Figure 21: Hysteresis curves of further precursors. The markers represent the measured mean steady state concentration of **a**, precursor **2** and **b**, precursor **3** and their standard deviation (*n*=5). The line is calculated by the kinetic model.

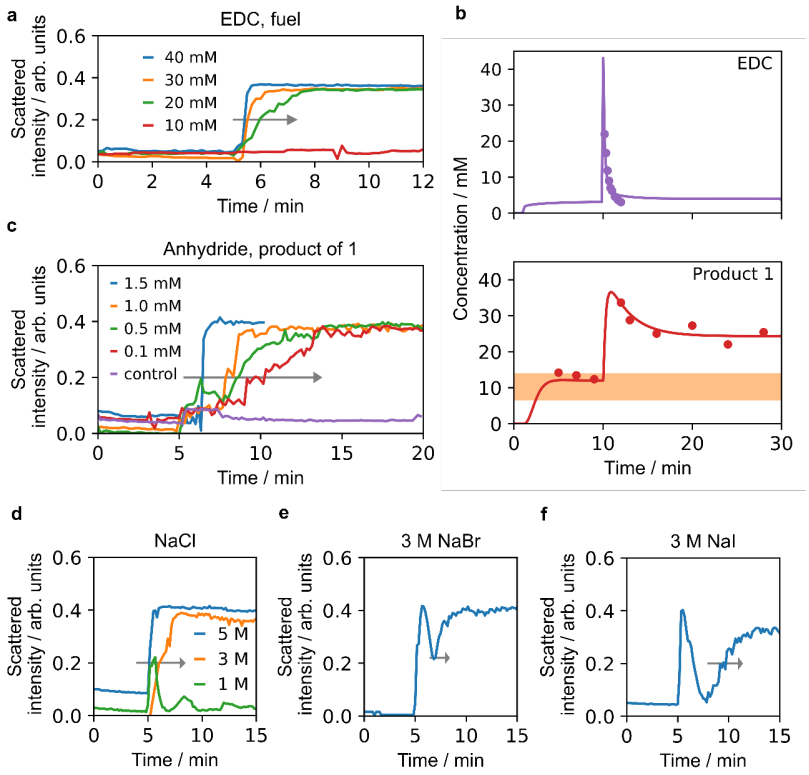

Supplementary Figure 22: Toggling the switch experiment – Activation: Various triggers were applied to switch the system on at 5 min when influxing 20 mM.min^{-1} EDC and 30 mM.min^{-1} precursor **1** at 21 °C. **a** The scattering over time taken as a measure for turbidity when adding various EDC fuel concentrations. **b** The steady state concentrations of EDC and anhydride over time as measured by HPLC and confirmed by the kinetic model. The transient addition of 40 mM EDC switches a steady state concentration inside the metastable zone to a higher steady state concentration with sustained crystal formation. **c** The scattering over time when seeding with crystalline anhydride. As negative control, polystyrene beads were added to test the effect of additional nucleation sites. **d** The effect of adding high concentration crystalline NaCl, **e**, NaBr and **f**, NaI.

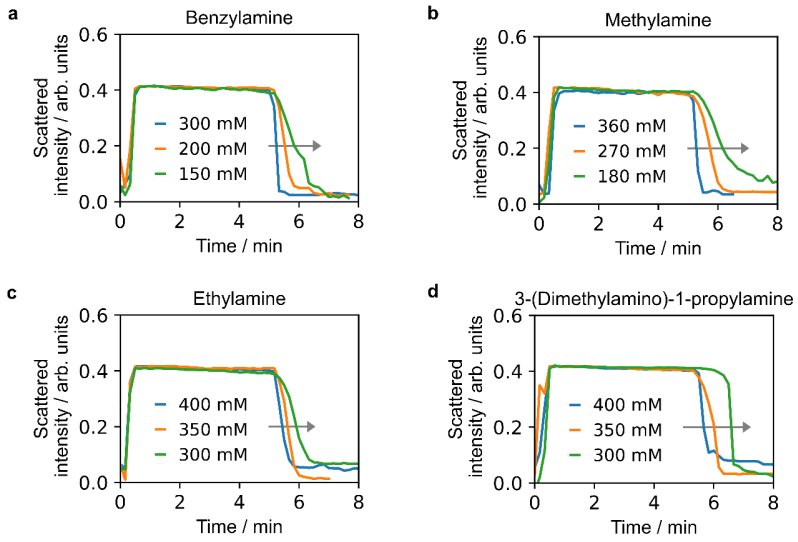

Supplementary Figure 23: Toggling the switch experiment - Deactivation. The system was influxed with 20 mM.min^{-1} EDC and 30 mM.min^{-1} precursor **1**. Spiking with 40 mM EDC before starting the pumps led to a sustained on state. At 5 min **a**, benzylamine, **b**, methylamine, **c**, ethylamine and **d,** a propylamine derivative was added as an off trigger. The decrease in scattering was measured over time to estimate the effectivness of deactivation.

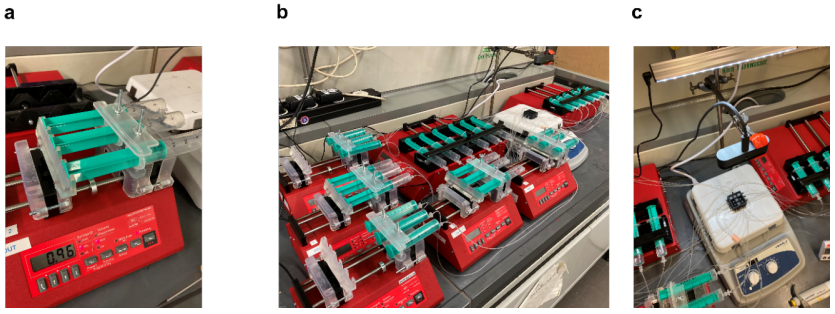

Supplementary Figure 24: The experimental setup of writing pixel-based patterns. a The 3D printed extension allows to control three syringes with one syringe pump. **b** To influx and outflux one reactor, three syringes are needed giving a total number of 27 syringes for a 9-digit pixel display. **c**, The 3x3 array was placed on a stir plate and timelapse photographs were taken by a webcam.

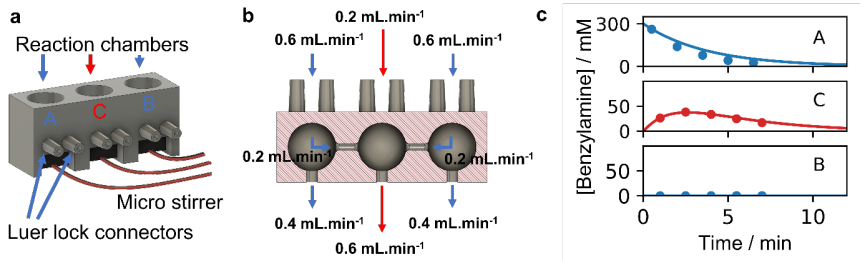

Supplementary Figure 25: A 3D printed setup to combine three switches to an OR-port. **a** The reactors A and B correspond to the input reactor and the middle reactor C serves as a readout. Each reactor is individually fueled with precursor **1** and EDC under a constant outflux. **b** A connection between the reactors allows an influx from the outer reactors into the middle reactor. **c** The influx of reactor A to C is tested by adding 300 mM of benzylamine to reactor A and monitoring the concentration over time by HPLC (marker). The line is predicted by the Matlab model.

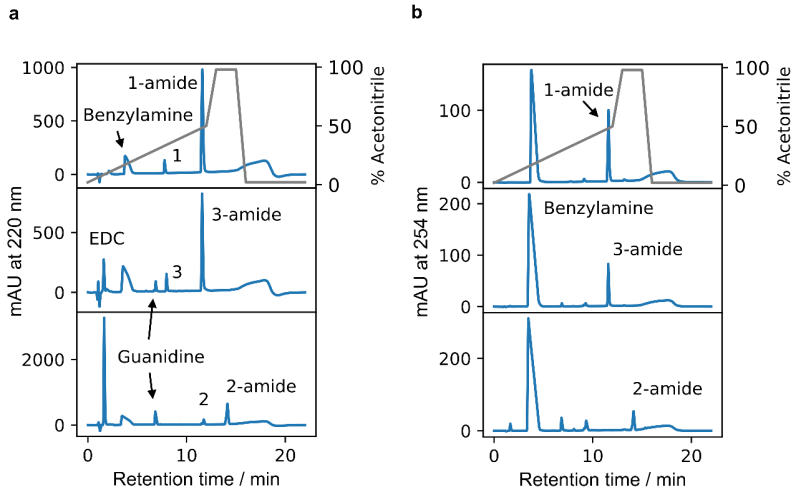

Supplementary Figure 26: The HPLC chromatograms of the quenched reaction cycle. Retention times and pump gradient of cycle **1**, **3** and **2** as recorded at **a**, 220 nm and **b**, 254 nm.

Supplementary Tables

	precursor **1**				precursor **2**[3]	precursor **3**
	21 °C	24 °C	28 °C	33 °C	25 °C	24 °C
k_1 ($M^{-1}s^{-1}$)	0.500				0.200	0.450
k_2 (s^{-1})	0.600*k_1	1.14*k_1	1.20*k_1	1.60*k_1	1.00*k_1	0.150*k_1
k_3 (s^{-1})	0.0500*k_1				0.250*k_1	0.0100*k_1
k_4 (s^{-1})	(0.00130*Temperature) – 0.0113				0.00350	0.00740

Supplementary Table 1: The rate constants used in the kinetic model. The deactivation rate constant k_4 of precursor **1** and **2** was extracted from batch experiments (SI 2). The rate constant for the activation (k_1) at 25 °C of precursor **1** was experimentally determined in previous work by monitoring the EDC decay profile with HPLC[4]. Its temperature dependence was estimated by fitting the previously mentioned batch experiments. The rate constants for k_2 and k_3 are not experimentally accessible. Their values were determined by fitting the experimental data and listed as a multiple of k_1.

X-ray Crystallographic Details

Single crystals were grown by dissolving synthesized and purified[4] anhydride of precursor **1** in minimum amount of acetone. Thereafter, the solution was filtered through a PTFE syringe filter. Crystals were obtained by diffusion of pentane into the acetone solution.

Data were collected on a single crystal x-ray diffractometer equipped with a CMOS detector (Bruker Photon-100), a TXS rotating anode with MoKα radiation (λ = 0.71073 Å) and a Helios optic using the APEX3 software package[5]. The measurements were performed on single crystals coated with perfluorinated ether. The crystals were fixed on top of a kapton micro sampler and frozen under a stream of cold nitrogen. A matrix scan was used to determine the initial lattice parameters. Reflections were corrected for Lorentz and polarisation effects, scan speed, and background using SAINT[6]. Absorption correction, including odd and even ordered spherical harmonics was performed using SADABS[6]. Space group assignment was based upon systematic absences, E statistics, and successful refinement of the structure. The structures were solved using SHELXT with the aid of successive difference Fourier maps, and were refined against all data using SHELXL in conjunction with SHELXLE[7,8,9]. Hydrogen atoms

(except on heteroatoms) were calculated in ideal positions as follows: Methyl hydrogen atoms were refined as part of rigid rotating groups, with a C–H distance of 0.98 Å and Uiso(H) = 1.5·Ueq(C). Non-methyl H atoms were placed in calculated positions and refined using a riding model with methylene, aromatic, and other C–H distances of 0.99 Å, 0.95 Å, and 1.00 Å, respectively, and Uiso(H) = 1.2·Ueq(C). Non-hydrogen atoms were refined with anisotropic displacement parameters. Full-matrix least-squares refinements were carried out by minimizing Σw(Fo2 Fc2)2 with the SHELXL weighting scheme.3 Neutral atom scattering factors for all atoms and anomalous dispersion corrections for the non-hydrogen atoms were taken from International Tables for Crystallography[10]. Images of the crystal structure were generated with PLATON[11]. Deposition Number 2127541 contains the supplementary crystallographic data for this paper. These data are provided free of charge by the joint Cambridge Crystallographic Data Centre and Fachinformationszentrum Karlsruhe Access Structures service www.ccdc.cam.ac.uk/structures.

Anhydride product 1 (CCDC 2127541)

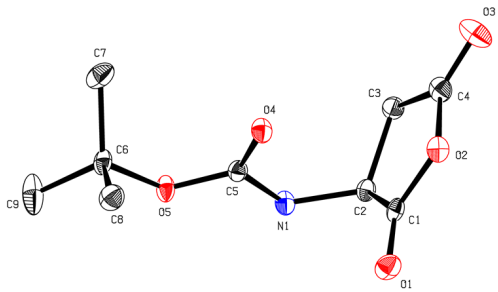

Diffractometer operator C. Jandl
scanspeed 1-5 s per frame
dx 50 mm
2311 frames measured in 8 data sets
phi-scans with delta_phi = 0.5
omega-scans with delta_omega = 0.5
shutterless mode

Crystal data

$C_9H_{13}NO_5$	
M_r = 215.20	D_x = 1.384 Mg m^{-3}
Orthorhombic, $P2_12_12_1$	Melting point: ? K
Hall symbol: P 2ac 2ab	Mo $K\alpha$ radiation, λ = 0.71073 Å

21

a = 5.1839 (6) Å	Cell parameters from 9496 reflections
b = 17.5000 (19) Å	θ = 2.5–26.4°
c = 22.773 (3) Å	μ = 0.11 mm^{-1}
V = 2065.9 (4) $Å^3$	*T* = 100 K
Z = 8	Fragment, colourless
F(000) = 912	0.33 × 0.16 × 0.08 mm

Data collection

Bruker Photon CMOS diffractometer	4252 independent reflections
Radiation source: TXS rotating anode	4104 reflections with $I > 2\sigma(I)$
Helios optic monochromator	R_{int} = 0.032
Detector resolution: 16 pixels mm^{-1}	θ_{max} = 26.4°, θ_{min} = 2.1°
phi– and ω–rotation scans	*h* = −6 6
Absorption correction: multi-scan *SADABS* 2016/2, Bruker	*k* = −21 21
T_{min} = 0.705, T_{max} = 0.745	*l* = −28 28
55658 measured reflections	

Refinement

Refinement on F^2	Hydrogen site location: mixed
Least-squares matrix: full	H atoms treated by a mixture of independent and constrained refinement
$R[F^2 > 2\sigma(F^2)]$ = 0.026	$W = 1/[\Sigma^2(FO^2) + (0.0342P)^2 + 0.4152P]$ WHERE $P = (FO^2 + 2FC^2)/3$
$wR(F^2)$ = 0.065	$(\Delta/\sigma)_{max} < 0.001$
S = 1.11	$\Delta\rho_{max}$ = 0.18 e $Å^{-3}$
4252 reflections	$\Delta\rho_{min}$ = −0.21 e $Å^{-3}$
285 parameters	Extinction correction: none
0 restraints	Extinction coefficient: -
0 constraints	Absolute structure: Flack, Parsons[8]
Primary atom site location: iterative	Absolute structure parameter: −0.14 (15)
Secondary atom site location: difference Fourier map	

Supplementary References

1. Kulkarni, S.A., Kadam, S.S., Meekes, H., Stankiewicz, A.I. & ter Horst, J.H. Crystal Nucleation Kinetics from Induction Times and Metastable Zone Widths. *Crystal Growth & Design* **13**, 2435-2440 (2013).
2. Tena-Solsona, M. et al. Non-equilibrium dissipative supramolecular materials with a tunable lifetime. *Nat Commun* **8**, 15895 (2017).
3. Wanzke, C., Tena-Solsona, M., Rieß, B., Tebcharani, L. & Boekhoven, J. Active droplets in a hydrogel release drugs with a constant and tunable rate. *Materials Horizons* **7**, 1397-1403 (2020).
4. Schnitter, F. & Boekhoven, J. A Method to Quench Carbodiimide-Fueled Self-Assembly. *ChemSystemsChem* **3** (2020).
5. *APEX suite of crystallographic software*, APEX 3, Version 2019-1.0, Bruker AXS Inc., Madison, Wisconsin, USA, 2019.
6. *SAINT*, Version 8.40A and *SADABS*, Version 2016/2, Bruker AXS Inc., Madison, Wisconsin, USA, 2016/2019.
7. G. M. Sheldrick, *Acta Crystallogr. Sect. A* **2015**, *71*, 3-8.
8. G. M. Sheldrick, *Acta Crystallogr. Sect. C* **2015**, *71*, 3-8.
9. C. B. Hübschle, G. M. Sheldrick, B. Ditrrich, *J. Appl. Cryst.* **2011**, *44*, 1281-1284
10. *International Tables for Crystallography*, *Vol. C* (Ed.: A. J. Wilson), Kluwer Academic Publishers, Dordrecht, The Netherlands, **1992**, Tables 6.1.1.4 (pp. 500-502), 4.2.6.8 (pp. 219-222), and 4.2.4.2 (pp. 193-199).
11. A. L. Spek, *Acta Crystallogr. Sect. D* **2009**, *65*, 148-155.

11 Summary and outlook

This thesis contributes a tangible method how to store memory inside volatile molecules. Similar to nature which cellular memory is regulated by reaction networks, I used a reaction cycle in which molecules are constantly turned over. In the carbodiimide-driven reaction cycle, precursor building blocks are activated by the conversion into transient anhydrides. The continuous activation and deactivation by the expense of fuel is coupled to the self-assembly into functional macroscopic structures. I explained the benefits of such dynamic structures and the obstacles when analyzing its kinetic parameters. The thesis showcases a method how to overcome this problem. I introduced a chemistry which stops all reactions taking place in the carbodiimide driven reaction cycle. Given its simplicity and convenience it is now applied in several research projects within different research groups.[50,65,118–120] The quenching chemistry opens the door to automatize the kinetic analysis. In future, several conditions could be screened in high throughput approaches. So far, the individual components are analyzed by HPLC. By modification of the quenching molecule into a so-called turn on probe, which spectroscopic properties change upon binding, the analysis could be further simplified and speeded up. Now, the reaction cycle's concentrations could be read out by simple microplate reader experiments.

Thereafter, I presented a protocol how to design and explore dynamic materials based upon the carbodiimide driven reaction cycle. I showed materials which supramolecular structures were encoded in the precursor design and which properties were switched on for a distinct time. A detailed workflow is presented to clarify each step in the experimental process. Thus, the protocol could help others to quickly get started working with carbodiimide-driven reaction cycles.

Finally, the thesis explains how molecular memory can be created from different stable steady states. I described the theory of bistable states and how they can be established from balancing the rates between forward and backward reaction. I showed that bistability can arise from simple organic building blocks in a continuously stirred tank reactor. I found that two features were preliminary for the system. The precursor used forms dynamic crystals which exert negative feedback upon its deactivation. That provides an amplification mechanism which keeps anhydride concentrations at a high level. Furthermore, the phase diagram of crystallization contains a so-called metastable zone in which both phases can be present regarding the history of the sample. I showed the existence of monostable states at low and high anhydride concentrations as well as bistable states which could be switched in between. In future such mechanisms could be considered for the design of synthetic cells. Recently, interesting strategies are being developed in creating boundary structures for compartmentalization. The described bistable system could be implemented into those confined structures to store information of past events inside other supramolecular structures than crystals.

12 Further Publications

Besides the three publications reprinted in sections 5, 6 and 10 I contributed to two more publications of the group from Prof. Job Boekhoven. The following section is a full list of the achievements during my PhD.

Publications

1 M. Tena Solona, J. Janssen, C. Wanzke, F. Schnitter, H. Park, B. Rieß, J. M. Gibbs, C. A. Weber, J. Boekhoven, Accelerated Ripening in Chemically Fueled Emulsions, *ChemSystemsChem* **2021**, 3, e2000034.

2 C. Donau, F. Späth, M. Sosson, B. Kriebisch, F. Schnitter, M. Tena-Solsona H. Kang, E. Salibi, M. Sattler, H. Mutschler, J. Boekhoven, Active coacervate droplets as a model for membraneless organelles and protocells, *Nat Commun* **2020**, 11, 5167.

3 F. Schnitter, J. Boekhoven, A Method to Quench Carbodiimide-Fueled Self-Assembly, *ChemSystemsChem* **2021**, 3, e2000037.

4 F. Schnitter, A. M. Bergmann, B. Winkeljann, J. Rodon Fores, O. Lieleg, J. Boekhoven, Synthesis and characterization of molecular assemblies driven by carbodiimide-based fuels, *Nat Protoc* **2021**, 16, 3901–3932.

5 F. Schnitter, B. Rieß, C. Jandl, J. Boekhoven, Memory, switches, and an OR-port through bistability in chemically fueled crystals, *Nat Commun* **2022**, 13, 2816.

13 Acknowledgements

Firstly, I would like to express my appreciation and thanks to Prof. Job Boekhoven for giving me the great opportunity to do my Ph.D. in his group and for his guidance and support in the course of my scientific research. Thank you for your multiple research ideas and your time discussing data, successfully working on manuscript outlines (despite conflicting OS) and finally for the careful correction of my thesis. Apart from working together, I enjoyed your open mind at our several group retreats and the conversations when cycling together to work.

I would also like to express my gratitude to Prof. Cathleen Zeymer for agreeing to be chairman of the examination committee, as well as Prof. Thomas Hermans and Prof. Alexander Pöthig for their interest shown in this manuscript and accepting to be members of my defense committee.

Furthermore, I would like to express my gratitude towards the "first" generation of the Boekhoven lab, Marta, Raphael, Caren and Benno, for the warm welcome when I started working in the group. Thank you for your open ears and teaching me how to use the several laboratory equipment.

Special thanks to all past and present members I have met in the Boekhoven group for their kindness, their help and for creating a wonderful ambience inside and outside the lab. Especially I want to mention Kun and Xiaoyao for organizing traditional Chinese hot pod dinners. Thank you, Patrick, for sharing the duty of maintaining functional HPLC instruments and, Michi, for sharing your delicious food with me. Carsten, Alex, Benno, Caren, Raphael and Patrick, I enjoyed learning and eventually playing Schafkopf during lunch. Thank you, Laura, Fabi and Judit, for organizing fancy after work events and keeping me up to date about the news in our group. I thank you, Jennifer, for taking care of ordering new starting material when I suddenly run low of precursor. Furthermore, I would like to thank Christine, Brigitte, Michele and Oleksii for their valuable scientific discussions and finally Monika and Simone for sharing the office with me. I would like to thank you Benno again, for helping me out whenever I had scientific or technical problems and being equally enthusiastic about riding bicycles.

I would like to thank my parents, Anneliese and Siegfried, for their love, patience and belief in me, throughout my studies and my Ph.D.

Finally, I thank Doro for her love. Thank you for being by my side and supporting me in every respect. I look forward to our exciting future together.

14 References

[1] Mara C. Inniss and Pamela A. Silver. Building synthetic memory. *Current biology : CB*, 23(17):R812–R816, 2013.

[2] S. G. Guan and A. S. Qi. Contributions of memory b cells to secondary immune response. *Bull Math Biol*, 57(5):713–31, 1995.

[3] Samantha B. Larsen, Christopher J. Cowley, Sairaj M. Sajjath, Douglas Barrows, Yihao Yang, Thomas S. Carroll, and Elaine Fuchs. Establishment, maintenance, and recall of inflammatory memory. *Cell Stem Cell*, 28(10):1758–1774.e8, 2021.

[4] Konrad Kleszczynski and Tobias W. Fischer. Melatonin and human skin aging. *Dermato-endocrinology*, 4(3):245–252, 2012.

[5] S. Gaddameedhi, C. P. Selby, M. G. Kemp, R. Ye, and A. Sancar. The circadian clock controls sunburn apoptosis and erythema in mouse skin. *J Invest Dermatol*, 135(4):1119–1127, 2015.

[6] Claudia Mueller, Mairon Trujillo-Miranda, Michael Maier, Daniel E. Heath, Andrea J. O'Connor, and Sahar Salehi. Effects of external stimulators on engineered skeletal muscle tissue maturation. *Advanced Materials Interfaces*, 8(1):2001167, 2021.

[7] J. C. Bruusgaard, I. B. Johansen, I. M. Egner, Z. A. Rana, and K. Gundersen. Myonuclei acquired by overload exercise precede hypertrophy and are not lost on detraining. *Proceedings of the National Academy of Sciences of the United States of America*, 107(34):15111–15116, 2010.

[8] Francis Crick. Neurobiology: Memory and molecular turnover. *Nature*, 312(5990):101–101, 1984.

[9] Devin R. Burrill and Pamela A. Silver. Making cellular memories. *Cell*, 140(1):13–18, 2010.

[10] Steven Henikoff and John M. Greally. Epigenetics, cellular memory and gene regulation. *Current Biology*, 26(14):R644–R648, 2016.

[11] Amber Willbanks, Meghan Leary, Molly Greenshields, Camila Tyminski, Sarah Heerboth, Karolina Lapinska, Kathryn Haskins, and Sibaji Sarkar. The evolution of epigenetics: From prokaryotes to humans and its biological consequences. *Genetics and epigenetics*, 8:25–36, 2016.

[12] Harsh Vashistha, Maryam Kohram, and Hanna Salman. Non-genetic inheritance restraint of cell-to-cell variation. *eLife*, 10:e64779, 2021.

[13] Moisés Santillán and Michael C. Mackey. Quantitative approaches to the study of bistability in the lac operon of escherichia coli. *Journal of the Royal Society, Interface*, 5 Suppl 1(Suppl 1):S29–S39, 2008.

[14] Mark Ptashne. A genetic switch: Gene control and phage. lambda. *Journal of Medical Genetics*, 1986.

[15] Guo-Ling Zhou, Li Xin, De-Pei Liu, and Chih-Chuan Liang. Remembering the cell fate during cellular differentiation. *Journal of Cellular Biochemistry*, 96(5):962–970, 2005.

[16] Ian B. Dodd, Mille A. Micheelsen, Kim Sneppen, and Geneviève Thon. Theoretical analysis of epigenetic cell memory by nucleosome modification. *Cell*, 129(4):813–822, 2007.

[17] R. M. Barrett and M. A. Wood. Beyond transcription factors: the role of chromatin modifying enzymes in regulating transcription required for memory. *Learn Mem*, 15(7):460–7, 2008.

[18] Daniel P. Stefanko, Ruth M. Barrett, Alexandra R. Ly, Gustavo K. Reolon, and Marcelo A. Wood. Modulation of long-term memory for object recognition via hdac inhibition. *Proceedings of the National Academy of Sciences*, 106(23):9447, 2009.

[19] Danielle Vermaak, Kami Ahmad, and Steven Henikoff. Maintenance of chromatin states: an open-and-shut case. *Current Opinion in Cell Biology*, 15(3):266–274, 2003.

[20] Jonathan Levenson and J. Sweatt. Epigenetic mechanisms in memory formation. nat rev neurosci. *Nature reviews. Neuroscience*, 6:108–118, 2005.

[21] Peter Cheung and Priscilla Lau. Epigenetic regulation by histone methylation and histone variants. *Molecular Endocrinology*, 19(3):563–573, 2005.

[22] Michael Morris and Lisa Monteggia. Role of dna methylation and the dna methyltransferases in learning and memory. *Dialogues in clinical neuroscience*, 16:359–71, 2014.

[23] C. A. Miller and J. D. Sweatt. Covalent modification of dna regulates memory formation. *Neuron*, 53(6):857–69, 2007.

[24] Oliver R. Maguire and Wilhelm T.S. Huck. On the importance of reaction networks for synthetic living systems. *Emerging Topics in Life Sciences*, 3(5):517–527, 2019.

[25] K. Das, L. Gabrielli, and L. J. Prins. Chemically fueled self-assembly in biology and chemistry. *Angew Chem Int Ed Engl*, 60(37):20120–20143, 2021.

[26] M. Whitesides George and Bartosz Grzybowski. Self-assembly at all scales. *Science*, 295(5564):2418–2421, 2002.

[27] Jean-Marie Lehn. Toward complex matter: Supramolecular chemistry and self-organization. *Proceedings of the National Academy of Sciences*, 99(8):4763, 2002.

[28] D. J. Kushner. Self-assembly of biological structures. *Bacteriological reviews*, 33(2):302–345, 1969.

[29] Jeremy L. England. Dissipative adaptation in driven self-assembly. *Nature Nanotechnology*, 10(11):919–923, 2015.

[30] F. H. Westheimer. Why nature chose phosphates. *Science*, 235(4793):1173–1178, 1987.

[31] C. T. Walsh, B. P. Tu, and Y. Tang. Eight kinetically stable but thermodynamically activated molecules that power cell metabolism. *Chem Rev*, 118(4):1460–1494, 2018.

[32] H. Hess and Jennifer L. Ross. Non-equilibrium assembly of microtubules: from molecules to autonomous chemical robots. *Chemical Society Reviews*, 46(18):5570–5587, 2017.

[33] J. Boekhoven, W. E. Hendriksen, G. J. Koper, R. Eelkema, and J. H. van Esch. Transient assembly of active materials fueled by a chemical reaction. *Science*, 349(6252):1075–9, 2015.

[34] Gonen Ashkenasy, Thomas M. Hermans, Sijbren Otto, and Annette F. Taylor. Systems chemistry. *Chemical Society Reviews*, 46(9):2543–2554, 2017.

[35] Rémi Merindol and Andreas Walther. Materials learning from life: concepts for active, adaptive and autonomous molecular systems. *Chemical Society Reviews*, 46(18):5588–5619, 2017.

[36] N. Singh, G. J. M. Formon, S. De Piccoli, and T. M. Hermans. Devising synthetic reaction cycles for dissipative nonequilibrium self-assembly. *Adv Mater*, 32(20):e1906834, 2020.

[37] Subhabrata Maiti, Ilaria Fortunati, Camilla Ferrante, Paolo Scrimin, and Leonard J. Prins. Dissipative self-assembly of vesicular nanoreactors. *Nature Chemistry*, 8(7):725–731, 2016.

[38] S. Maeda, Y. Hara, T. Sakai, R. Yoshida, and S. Hashimoto. Self-walking gel. *Advanced Materials*, 19(21):3480–3484, 2007.

[39] Jacqui M. A. Carnall, Christopher A. Waudby, Ana M. Belenguer, Marc C. A. Stuart, Jerome J.-P. Peyralans, and Sijbren Otto. Mechanosensitive self-replication driven by self-organization. *Science*, 327(5972):1502–1506, 2010.

[40] Giulio Ragazzon and Leonard J. Prins. Energy consumption in chemical fuel-driven self-assembly. *Nature Nanotechnology*, 13(10):882–889, 2018.

[41] Jan H. van Esch, Rafal Klajn, and Sijbren Otto. Chemical systems out of equilibrium. *Chemical Society Reviews*, 46(18):5474–5475, 2017.

[42] Alessandro Sorrenti, Jorge Leira-Iglesias, Albert J. Markvoort, Tom F. A. de Greef, and Thomas M. Hermans. Non-equilibrium supramolecular polymerization. *Chemical Society Reviews*, 46(18):5476–5490, 2017.

[43] Job Boekhoven, Aurelie M. Brizard, Krishna N. K. Kowlgi, Ger. J. M. Koper, Rienk Eelkema, and Jan H. van Esch. Dissipative self-assembly of a molecular gelator by using a chemical fuel. *Angewandte Chemie International Edition*, 49(28):4825–4828, 2010.

[44] L. S. Kariyawasam and C. S. Hartley. Dissipative assembly of aqueous carboxylic acid anhydrides fueled by carbodiimides. *J Am Chem Soc*, 139(34):11949–11955, 2017.

[45] M. Tena-Solsona, B. Riess, R. K. Grotsch, F. C. Lohrer, C. Wanzke, B. Kasdorf, A. R. Bausch, P. Muller-Buschbaum, O. Lieleg, and J. Boekhoven. Non-equilibrium dissipative supramolecular materials with a tunable lifetime. *Nat Commun*, 8:15895, 2017.

[46] Lasith S. Kariyawasam, Julie C. Kron, Run Jiang, André J. Sommer, and C. Scott Hartley. Structure–property effects in the generation of transient aqueous benzoic acid anhydrides by carbodiimide fuels. *The Journal of Organic Chemistry*, 85(2):682–690, 2020.

[47] C. A. Bunton, N. A. Fuller, S. G. Perry, and V. J. Shiner. The hydrolysis of carboxylic anhydrides. part iii. reactions in initially neutral solution. *Journal of the Chemical Society (Resumed)*, 0(0):2918–2926, 1963.

[48] Lennart Eberson, Martin Nilsson, Janice Elvidge, James S. Burton, and Roger Stevens. Studies on cyclic anhydrides. i. rate constants and activation parameters for the solvolysis of alkylsubstituted cyclic anhydrides in aqueous solution by the ph-stat method. *Acta Chemica Scandinavica*, 18:534–542, 1964.

[49] James S. Nowick and Shabana Insaf. The propensities of amino acids to form parallel beta-sheets. *Journal of the American Chemical Society*, 119(45):10903–10908, 1997.

[50] C. Donau, F. Spath, M. Sosson, B. A. K. Kriebisch, F. Schnitter, M. Tena-Solsona, H. S. Kang, E. Salibi, M. Sattler, H. Mutschler, and J. Boekhoven. Active coacervate droplets as a model for membraneless organelles and protocells. *Nat Commun*, 11(1):5167, 2020.

[51] Philippe Matile. Biochemistry and function of vacuoles. *Annual Review of Plant Physiology*, 29(1):193–213, 1978.

[52] Caren Wanzke, Marta Tena-Solsona, Benedikt Rieß, Laura Tebcharani, and Job Boekhoven. Active droplets in a hydrogel release drugs with a constant and tunable rate. *Materials Horizons*, 7(5):1397–1403, 2020.

[53] L. Tebcharani, C. Wanzke, T. M. Lutz, J. Rodon-Fores, O. Lieleg, and J. Boekhoven. Emulsions of hydrolyzable oils for the zero-order release of hydrophobic drugs. *J Control Release*, 339:498–505, 2021.

[54] P. S. Schwarz, L. Tebcharani, J. E. Heger, P. Muller-Buschbaum, and J. Boekhoven. Chemically fueled materials with a self-immolative mechanism: transient materials with a fast on/off response. *Chem Sci*, 12(29):9969–9976, 2021.

[55] Fabian Schnitter and Job Boekhoven. A method to quench carbodiimide-fueled self-assembly. *ChemSystemsChem*, 3(1), 2020.

[56] B. Riess, C. Wanzke, M. Tena-Solsona, R. K. Grotsch, C. Maity, and J. Boekhoven. Dissipative assemblies that inhibit their deactivation. *Soft Matter*, 14(23):4852–4859, 2018.

[57] K. Dai, J. R. Fores, C. Wanzke, B. Winkeljann, A. M. Bergmann, O. Lieleg, and J. Boekhoven. Regulating chemically fueled peptide assemblies by molecular design. *J Am Chem Soc*, 142(33):14142–14149, 2020.

[58] M. Tena-Solsona, C. Wanzke, B. Riess, A. R. Bausch, and J. Boekhoven. Self-selection of dissipative assemblies driven by primitive chemical reaction networks. *Nat Commun*, 9(1):2044, 2018.

[59] Caren Wanzke, Alexander Jussupow, Fabian Kohler, Hendrik Dietz, Ville R. I. Kaila, and Job Boekhoven. Dynamic vesicles formed by dissipative self-assembly. *ChemSystemsChem*, 2(1), 2019.

[60] Ronald F. Evilia. Quantitative nmr spectroscopy. *Analytical Letters*, 34(13):2227–2236, 2001.

[61] A. Hofmann. *Spectroscopic techniques: I Spectrophotometric techniques*, pages 477–521. Cambridge University Press, Cambridge, 7 edition, 2010.

[62] Fabian Schnitter, Alexander M. Bergmann, Benjamin Winkeljann, Jennifer Rodon Fores, Oliver Lieleg, and Job Boekhoven. Synthesis and characterization of chemically fueled supramolecular materials driven by carbodiimide-based fuels. *Nature Protocols*, 16(8):3901–3932, 2021.

[63] Santanu Panja, Bart Dietrich, and Dave J. Adams. Chemically fuelled self-regulating gel-to-gel transition. *ChemSystemsChem*, 2(1):e1900038, 2020.

[64] Subhajit Bal, Krishnendu Das, Sahnawaz Ahmed, and Dibyendu Das. Chemically fueled dissipative self-assembly that exploits cooperative catalysis. *Angewandte Chemie International Edition*, 58(1):244–247, 2019.

[65] Stefan Borsley, David A. Leigh, and Benjamin M. W. Roberts. A doubly kinetically-gated information ratchet autonomously driven by carbodiimide hydration. *Journal of the American Chemical Society*, 143(11):4414–4420, 2021.

[66] Jr. Ferrell, J. E. Self-perpetuating states in signal transduction: positive feedback, double-negative feedback and bistability. *Curr Opin Cell Biol*, 14(2):140–8, 2002.

[67] Albert Goldbeter. Dissipative structures in biological systems: bistability, oscillations, spatial patterns and waves. *Philosophical Transactions of the Royal Society A: Mathematical, Physical and Engineering Sciences*, 376(2124):20170376, 2018.

[68] Amos B. Oppenheim, Oren Kobiler, Joel Stavans, Donald L. Court, and Sankar Adhya. Switches in bacteriophage lambda development. *Annual Review of Genetics*, 39(1):409–429, 2005.

[69] Stephen T. Crews and Joseph C. Pearson. Transcriptional autoregulation in development. *Current biology : CB*, 19(6):R241–R246, 2009.

[70] R. A. Schubert, I. B. Dodd, J. B. Egan, and K. E. Shearwin. Cro's role in the ci cro bistable switch is critical for lambda's transition from lysogeny to lytic development. *Genes Dev*, 21(19):2461–72, 2007.

[71] Dong-Eun Chang, Shelly Leung, Mariette R. Atkinson, Aaron Reifler, Daniel Forger, and Alexander J. Ninfa. Building biological memory by linking positive feedback loops. *Proceedings of the National Academy of Sciences*, 107(1):175, 2010.

[72] Alexander Y. Mitrophanov and Eduardo A. Groisman. Positive feedback in cellular control systems. *BioEssays : news and reviews in molecular, cellular and developmental biology*, 30(6):542–555, 2008.

[73] Joseph R. Pomerening. Positive-feedback loops in cell cycle progression. *FEBS Letters*, 583(21):3388–3396, 2009.

[74] J. E. Ferrell and W. Xiong. Bistability in cell signaling: How to make continuous processes discontinuous, and reversible processes irreversible. *Chaos*, 11(1):227–236, 2001.

[75] David L. Brautigan. *Protein Phosphatases*, volume 49, pages 197–214. Academic Press, Boston, 1994.

[76] Heidi Vitrac, Venkata K. P. S. Mallampalli, and William Dowhan. Importance of phosphorylation/dephosphorylation cycles on lipid-dependent modulation of membrane protein topology by posttranslational phosphorylation. *The Journal of biological chemistry*, 294(49):18853–18862, 2019.

[77] Alessandro Sorrenti, Jorge Leira-Iglesias, Akihiro Sato, and Thomas M. Hermans. Non-equilibrium steady states in supramolecular polymerization. *Nature Communications*, 8(1):15899, 2017.

[78] Melanie I. Stefan and Nicolas Le Novère. Cooperative binding. *PLoS computational biology*, 9(6):e1003106–e1003106, 2013.

[79] G. C. Faas, B. Schwaller, J. L. Vergara, and I. Mody. Resolving the fast kinetics of cooperative binding: Ca2+ buffering by calretinin. *PLoS Biol*, 5(11):e311, 2007.

[80] Ariane Vartanian. The many facets of cooperativity. *Nature Reviews Materials*, 6(9):763–763, 2021.

[81] Larissa K. S. von Krbek, Christoph A. Schalley, and Pall Thordarson. Assessing cooperativity in supramolecular systems. *Chemical Society Reviews*, 46(9):2622–2637, 2017.

[82] William A. Eaton, Eric R. Henry, James Hofrichter, and Andrea Mozzarelli. Is cooperative oxygen binding by hemoglobin really understood? *Nature Structural Biology*, 6(4):351–358, 1999.

[83] Maria Rosa Domingo-Sananes, Orsolya Kapuy, Tim Hunt, and Bela Novak. Switches and latches: a biochemical tug-of-war between the kinases and phosphatases that control mitosis. *Philosophical Transactions of the Royal Society B: Biological Sciences*, 366(1584):3584–3594, 2011.

[84] Jr. Ferrell, James E. Tripping the switch fantastic: how a protein kinase cascade can convert graded inputs into switch-like outputs. *Trends in Biochemical Sciences*, 21(12):460–466, 1996.

[85] J. E. Lisman. A mechanism for memory storage insensitive to molecular turnover: a bistable autophosphorylating kinase. *Proc Natl Acad Sci U S A*, 82(9):3055–7, 1985.

[86] Jr. Ferrell, J. E. Bistability, bifurcations, and waddington's epigenetic landscape. *Curr Biol*, 22(11):R458–66, 2012.

[87] Masanori Shigeno, Yo Kushida, and Masahiko Yamaguchi. Molecular switching involving metastable states: molecular thermal hysteresis and sensing of environmental changes by chiral helicene oligomeric foldamers. *Chemical Communications*, 52(28):4955–4970, 2016.

[88] Mark J. Solomon. Hysteresis meets the cell cycle. *Proceedings of the National Academy of Sciences*, 100(3):771, 2003.

[89] Joseph R. Pomerening, Eduardo D. Sontag, and James E. Ferrell. Building a cell cycle oscillator: hysteresis and bistability in the activation of cdc2. *Nature Cell Biology*, 5(4):346–351, 2003.

[90] Sergey N. Semenov, Albert S. Y. Wong, R. Martijn van der Made, Sjoerd G. J. Postma, Joost Groen, Hendrik W. H. van Roekel, Tom F. A. de Greef, and Wilhelm T. S. Huck. Rational design of functional and tunable oscillating enzymatic networks. *Nature Chemistry*, 7(2):160–165, 2015.

[91] Albert Goldbeter. Dissipative structures and biological rhythms. *Chaos: An Interdisciplinary Journal of Nonlinear Science*, 27(10):104612, 2017. doi: 10.1063/1.4990783.

[92] J. W. Pringle. The excitation and contraction of the flight muscles of insects. *The Journal of physiology*, 108(2):226–232, 1949.

[93] John D. Palmer. The clocks that time us. physiology of the circadian timing systems. martin c. moore-ede , frank m. sulzman , charles a. fuller. *The Quarterly Review of Biology*, 57(4):511–512, 1982.

[94] H. Ukai and H. R. Ueda. Systems biology of mammalian circadian clocks. *Annu Rev Physiol*, 72:579–603, 2010.

[95] S. Kondo. The reaction-diffusion system: a mechanism for autonomous pattern formation in the animal skin. *Genes Cells*, 7(6):535–41, 2002.

[96] M. Way. "what i cannot create, i do not understand". *J Cell Sci*, 130(18):2941–2942, 2017.

[97] Sjoerd G. J. Postma, Dana te Brinke, Ilia N. Vialshin, Albert S. Y. Wong, and Wilhelm T. S. Huck. A trypsin-based bistable switch. *Tetrahedron*, 73(33):4896–4900, 2017.

[98] K. Montagne, R. Plasson, Y. Sakai, T. Fujii, and Y. Rondelez. Programming an in vitro dna oscillator using a molecular networking strategy. *Mol Syst Biol*, 7:466, 2011.

[99] Jesse Stricker, Scott Cookson, Matthew R. Bennett, William H. Mather, Lev S. Tsimring, and Jeff Hasty. A fast, robust and tunable synthetic gene oscillator. *Nature*, 456(7221):516–519, 2008.

[100] Pascale Angelica Bachmann, Pier Luigi Luisi, and Jacques Lang. Autocatalytic self-replicating micelles as models for prebiotic structures. *Nature*, 357(6373):57–59, 1992.

[101] Thomas Buhse, Véronique Pimienta, Dominique Lavabre, and Jean-Claude Micheau. Experimental evidence of kinetic bistability in a biphasic surfactant system. *The Journal of Physical Chemistry A*, 101(29):5215–5217, 1997.

[102] S. M. Morrow, I. Colomer, and S. P. Fletcher. A chemically fuelled self-replicator. *Nat Commun*, 10(1):1011, 2019.

[103] Sergey N. Semenov, Lewis J. Kraft, Alar Ainla, Mengxia Zhao, Mostafa Baghbanzadeh, Victoria E. Campbell, Kyungtae Kang, Jerome M. Fox, and George M. Whitesides. Autocatalytic, bistable, oscillatory networks of biologically relevant organic reactions. *Nature*, 537(7622):656–660, 2016.

[104] R. Mukherjee, R. Cohen-Luria, N. Wagner, and G. Ashkenasy. A bistable switch in dynamic thiodepsipeptide folding and template-directed ligation. *Angew Chem Int Ed Engl*, 54(42):12452–6, 2015.

[105] Indrajit Maity, Nathaniel Wagner, Rakesh Mukherjee, Dharm Dev, Enrique Peacock-Lopez, Rivka Cohen-Luria, and Gonen Ashkenasy. A chemically fueled non-enzymatic bistable network. *Nature Communications*, 10(1):4636, 2019.

[106] Jorge Leira-Iglesias, Alessandra Tassoni, Takuji Adachi, Michael Stich, and Thomas M. Hermans. Oscillations, travelling fronts and patterns in a supramolecular system. *Nature Nanotechnology*, 13(11):1021–1027, 2018.

[107] Juan Manuel Parrilla-Gutierrez, Abhishek Sharma, Soichiro Tsuda, Geoffrey J. T. Cooper, Gerardo Aragon-Camarasa, Kevin Donkers, and Leroy Cronin. A programmable chemical computer with memory and pattern recognition. *Nature Communications*, 11(1):1442, 2020.

[108] Akiko Kaminaga, Vladimir K. Vanag, and Irving R. Epstein. A reaction–diffusion memory device. *Angewandte Chemie International Edition*, 45(19):3087–3089, 2006.

[109] Hongwei Zhou, Xiaobin Ding, Zhaohui Zheng, and Yuxing Peng. Self-regulated intelligent systems: where adaptive entities meet chemical oscillators. *Soft Matter*, 9(20):4956–4968, 2013.

[110] István Lagzi, Bartlomiej Kowalczyk, Dawei Wang, and Bartosz A. Grzybowski. Nanoparticle oscillations and fronts. *Angewandte Chemie International Edition*, 49(46):8616–8619, 2010.

[111] Hideki Nabika, Tetsuro Oikawa, Keisuke Iwasaki, Kei Murakoshi, and Kei Unoura. Dynamics of gold nanoparticle assembly and disassembly induced by ph oscillations. *The Journal of Physical Chemistry C*, 116(10):6153–6158, 2012.

[112] Jinshan Guo, Eszter Poros-Tarcali, and Juan Perez-Mercader. Evolving polymersomes autonomously generated in and regulated by a semibatch ph oscillator. *Chemical Communications*, 55(63):9383–9386, 2019.

[113] Guangtong Wang, Bohan Tang, Yang Liu, Qingyu Gao, Zhiqiang Wang, and Xi Zhang. The fabrication of a supra-amphiphile for dissipative self-assembly. *Chemical Science*, 7(2):1151–1155, 2016.

[114] Klara Kovacs, Rachel E. McIlwaine, Stephen K. Scott, and Annette F. Taylor. An organic-based ph oscillator. *The Journal of Physical Chemistry A*, 111(4):549–551, 2007.

[115] Ljiljana Kolar-Anić and Guy Schmitz. Mechanism of the bray–liebhafsky reaction: effect of the oxidation of iodous acid by hydrogen peroxide. *Journal of the Chemical Society, Faraday Transactions*, 88(16):2343–2349, 1992.

[116] Richard J. Field and Horst Dieter Foersterling. On the oxybromine chemistry rate constants with cerium ions in the field-koeroes-noyes mechanism of the belousov-zhabotinskii reaction: the equilibrium hbro2 + bro3- + h+ .dblharw. 2bro.ovrhdot.2 + h2o. *The Journal of Physical Chemistry*, 90(21):5400–5407, 1986.

[117] Atchara Sirimungkala, Horst-Dieter Försterling, Vladimir Dlask, and Richard J. Field. Bromination reactions important in the mechanism of the belousov-zhabotinsky system. *The Journal of Physical Chemistry A*, 103(8):1038–1043, 1999. doi: 10.1021/jp9825213.

[118] Fabian Spaeth, Carsten Donau, Alexander M. Bergmann, Moritz Kränzlein, Christopher V. Synatschke, Bernhard Rieger, and Job Boekhoven. Molecular design of chemically fueled peptide–polyelectrolyte coacervate-based assemblies. *Journal of the American Chemical Society*, 143(12):4782–4789, 2021.

[119] Michaela A. Wuerbser, Patrick S. Schwarz, Jonas Heckel, Alexander M. Bergmann, Andreas Walther, and Job Boekhoven. Chemically fueled block copolymer self-assembly into transient nanoreactors. *ChemSystemsChem*, 3(5):e2100015, 2021.

[120] Kun Dai, Marta Tena-Solsona, Jennifer Rodon Fores, Alexander M. Bergmann, and Job Boekhoven. Morphological transitions in chemically fueled self-assembly. *Nanoscale*, 13(47):19864–19869, 2021.